Fakultät für Medizin

Development of Novel Genetically Encoded Labels for Optoacoustic Imaging

Kanuj Mishra

Vollständiger Abdruck der von der Fakultät für Medizin der Technischen
Universität München zur Erlangung des akademischen Grades
eines

Doktors der Naturwissenschaften
Genehmigten Dissertation

Vorsitzender: **Prof. Dr. Wolfgang Weber**
Prüfer der Dissertation: 1. **Prof. Dr. Vasilis Ntziachristos**
2. **Prof. Dr. Michael Sattler**

Die Dissertation wurde am **12.10.2020** bei der Technischen Universität München eingereicht und durch die Fakultät für Medizin am **13.07.2021** angenommen.

Dedicated to My Parents

Acknowledgment

My Doctoral Dissertation at the Institute of Biological and Medical Imaging (IBMI), Helmholtz Zentrum Munich, has helped to enhance my scientific knowledge and made it a very thankful journey.

I wish to express my humble gratitude to my primary supervisor, Prof. Vasilis Ntziachristos, for giving me the opportunity, support, and facilities to perform this research work in IBMI. The foremost appreciation I would like to offer to my Mentor and Guide, Dr. Andre C. Stiel (Group Leader – Cell Engineering Group, IBMI). He has helped me in crafting various aspects during my thesis with valuable scientific discussions and motivation. I also feel obliged to my co-supervisor Prof. Michael Sattler (STB, HMGU) for his timely advice and kind encouragement in all the Thesis Advisory Committee meetings.

I am also very grateful to my good friend, collaborator, and colleague Dr. Juan Pablo Fuenzalida Werner, for teaching me all about protein biology and helping me throughout my Ph.D. work by giving valuable suggestions and advice.

Moreover, I like to acknowledge all the past and present members of the IBMI for their collaboration, help, and extensive scientific discussion. My special thanks go to Uwe Klemm, Pia Anzenhofer, Sarah Glasl, and Ruth Hillerman for their incredible support and technical assistance. I also extend my appreciation to the DFG and Helmholtz Zentrum Munich to provide financial support during my Ph.D.

My thesis and exposure were made memorable and worth reminiscing due to my friend’s presence from the beginning to the end of my journey – Dr. Vipul Gujrati, Dr. Ajay Kesharwani, and Dr. Mayur Andulkar. I want to thank especially my wife, Dr. Sharmilee Vetrivel. She stood with me during my whole journey and supported me scientifically & emotionally.

Thank you so much!

Abstract

Optoacoustic (OA) imaging represents an emerging imaging modality that achieves high-resolution, real-time *in-vivo* imaging well beyond the 1mm penetration depth. The current challenge in OA imaging is the lack of specific absorbers capable of competing with the signal from tissue background. Reversibly switchable proteins (RSPs) have been instrumental for life science imaging due to their contribution to sub-diffraction-resolution optical microscopy (nanoscopy). Initial *in-vitro* studies have shown their possible beneficial applications in optoacoustic (OA) imaging, where they allow efficient separation of the label signal from a non-modulating background (lock-in-detection). Understanding of the photophysics of RSPs in OA and tailoring reporters for OA are essential to enable its routine application in imaging. In this thesis, I first analyzed the photophysical behavior of existing RSPs under the condition used in OA and found that BphPs possess favorable characteristics for OA. The insights gained laid the foundation for a focused development of RSP reporters based on BphPs for OA.

To identify the most promising BphPs for further development, eight native BphPs were screened by probing their photophysics suitable for OA. Further modification using structure-guided truncation based strategy of selected BphPs from *Rhozobium etli* & *Rhodopseudomonas palustris* resulted in a higher absorbing, & fast switching, *Re*BphP-PCM and slow switching *Rp*BphP1-PCM. The introduced rsOAPs, in combination with the ML-based unmixing approach and commercial OA imaging system, allowed *In-vivo* sensitivity of 500 immune-cells and 14000 *E. Coli*. I demonstrated the possibility of studying cancer development over time, using deep-seated colorectal and superficial breast tumor models. rsOAPs with different switching kinetics allowed simultaneous tracking of mixed Jurkat T cells-population through temporal multiplexing.

In summary, extensive characterization of RSPs in OA led to the selection and development of superior BphPs based rsOAPs. The developed rsOAPs along with ML unmixing algorithm and commercial OA imaging system, are potential tools allowing highly sensitive detection and multiplexing in whole animal OA imaging.

Zusammenfassung

Die optoakustische (OA) Bildgebung stellt eine neue Bildgebungsmodalität dar, welche eine hochauflösende *In-vivo*-Echtzeit-Bildgebung mit einer Eindringtiefe von über 1 mm ermöglicht. Die aktuelle Herausforderung bei der OA-Bildgebung, ist das Fehlen spezifischer Absorber, welche mit dem Signal vom Gewebehintergrund konkurrieren können. Reversibel schaltbare Proteine (RSP) waren aufgrund ihres Beitrags zur optischen Mikroskopie mit Subbeugungsauflösung (Nanoskopie) für die Life-Science-Bildgebung von entscheidender Bedeutung. Erste *In-vitro*-Studien haben ihre möglichen vorteilhaften Anwendungen in der optoakustischen (OA) Bildgebung gezeigt, in welcher sie eine effiziente Trennung des Markierungssignals vor einem nicht modulierenden Hintergrund ermöglichen (Lock-in-Detektion). Das Verständnis der Photophysik von RSP in der Optoakustik (OA) und die Anpassung von Reportern für die OA sind unerlässlich, um die routinemäßige Anwendung in der Bildgebung zu ermöglichen. In dieser Arbeit analysierte ich zunächst das photophysikalische Verhalten bestehender RSP unter den bei der OA verwendeten Bedingungen und fand heraus, dass BphP vorteilhafte Eigenschaften für die OA besitzen. Die gewonnenen Erkenntnisse legten den Grundstein für eine gezielte Entwicklung von RSP-Reportern auf der Basis von BphPs für die OA.

Um die vielversprechendsten BphPs für die weitere Entwicklung zu identifizieren, wurden acht native BphPs durch Überprüfung ihrer photophysikalischen Eigenschaften für die OA, untersucht. Weitere Modifikationen, unter Verwendung einer strukturgesteuerten verkürzungsbasierten Strategie, ausgewählter BphPs aus *Rhozobium etli* & *Rhodopseudomonas palustris*, führten zu einem höher absorbierenden und schnell schaltenden *Re*BphP-PCM und einem langsam schaltenden *Rp*BphP1-PCM. Die vorgestellten rsOAP ermöglichten in Kombination mit dem ML-basierten Unmixing und dem kommerziellen OA-Bildgebungssystem eine *In-vivo*-Sensitivität von 500 Immunzellen und 14000 *E. Coli*. Ich habe die Möglichkeit aufgezeigt, die zeitliche Entwicklung von tiefsitzenden kolorektalen und oberflächlichen Brusttumor-Modellen zu untersuchen. rsOAPs mit unterschiedlicher Schaltkinetik ermöglichten die gleichzeitige Verfolgung von gemischten Jurkat-T-Zell populationen durch zeitlichen Multiplexen.

Zusammenfassend führte eine umfassende Charakterisierung von RSPs in der OA zur Auswahl und Entwicklung überlegener BphPs-basierter rsOAPs. Die entwickelten

rsOAPs sind, zusammen mit dem ML-unmixing algorithmus und dem kommerziellen OA-Bildgebungssystem, potenzielle Werkzeuge, die eine hochempfindliche Erkennung und Multiplexverfahren bei der OA-Bildgebung von ganzen Tieren ermöglichen.

Table of Contents

Chapter 1: Introduction

1.1 General Concepts of Optoacoustics

In the last decades, optical imaging has played a crucial role in providing valuable information for *in-vivo* biomedical studies[1]. However, the strong absorption and scattering of light in soft tissue limits the penetration depth vs. resolution ratio of pure optical methods. For example the high resolution of intravital microscopy (IVM) is only achievable up to a few hundred micrometers[1]. Conversely, whole animal fluorescence methods show very poor resolution of 2-3 millimeters. Thus, fluorescence is limited either in imaging volume or resolution and fails to provide a comprehensive understanding of complex biological events like whole tumor development and the multiple biological events taking place in its microenvironment. These limitations provoked the researchers to look for alternative modalities such as ultrasound, X-Ray, computed tomography (CT), magnetic resonance imaging (MRI), and positron emission tomography (PET). While ultrasound imaging offers a low-cost implementation, other modalities require high infrastructure and frequently specialized contrast agents[2], e.g., specific cell population visualization by using genetically encoded labels

Optoacoustic (OA) overcomes the limitations of pure optical methods by combining optical excitation with ultrasound detection. OA provides higher resolution imaging of tissue to a depth of several centimeters as sound scatters 1000 times less than light, allowing acoustic signal propagation much deeper in biological tissue without significant attenuation.[1,3]

Additionally, OA has highly attractive features such as spatial resolution of ~50-200 µm for imaging at depths more than 1cm (Figure 1B), sensitivity for endogenous absorbers like oxy/deoxyhemoglobin[4,5], melanin[6], and lipid[7,8] allowing anatomical conclusions, as well as exogenous labels like nanoparticles[9], and genetically encoded chromophoric proteins[10]. The versatility of OA in simultaneously visualizing anatomical features using endogenous absorbers and specific tagged cells using genetically encoded labels gives it a significant edge over other modalities for deep tissue imaging.

In OA, the sample is illuminated by a nanosecond pulsed laser, that excites the absorber and causes a thermo-elastic expansion after a non-radiative decay, generating transient acoustic waves. These ultrasound waves are detected as a pressure signal using ultrasound transducers and reconstructed into an image using inversion algorithms[11] (Figure 1A). OA imaging based on endogenous chromophores like hemoglobin and lipids[9,12] has already proved its potential for biomedical research, providing intriguing insights into neuronal dynamics[13], psoriasis[14], brown fat metabolism[8], and tumor heterogeneity[15,16].

While a wide range of exogenous contrast agents, such as dyes[10] or nanoparticles[17,18], have been used in OA, their use in longitudinal *in-vivo* OA imaging is often hampered by limitations such as specificity, low systemic delivery, high toxicity, and rapid clearance[10]. Transgene labels at the same time cannot be cleared or diluted and provide specificity, making it feasible to study specific cell types. Transgene labels such as enzymatic reporter system (*lacz* reporter gene system[19], melanin[20], or violacein[21]) or fluorescent labels (EGFP or mCherry)[22] have been explored in OA. Both are limited in their OA applications. The enzymatic reporter-based approach has proven less effective because most products absorb in the visible range. Moreover, the product melanin emits a strong acoustic signal, but its production stresses cells[23], and its absorption spectrum lacks features that can be easily distinguish from the background. Concurrently, the known fluorescent labels are too blue-shifted for *in-vivo* imaging due to the high light absorption of visible light by tissues. To overcome these limitations, NIR absorbing labels like iRFP720[24] has been employed in OA imaging. These labels provide an advantage compared to visible range FPs as the excitation light penetrates deeper in NIR region. However, the signal from these NIR absorbing proteins is often too weak, and their concentration is too low to give a significant signal against the overwhelming background of endogenous absorbers.

Recently, reversible switchable proteins (RSPs) provided a better alternative for OA imaging, generating sufficiently strong signal over background at lower and more physiological concentrations by virtue of their photo-switching. They are characterized by their ability to be repeatedly photo-switched between two states using the light of two distinct wavelengths, allowing it to be separated from the non-switchable background, such as blood hemoglobin. To achieve this, the sample is repeatedly illuminated: first with a wavelength that switches the label to either an OA-active or inactive state and subsequently with a second wavelength that induces a reverse transition[25]. Since the frequency at which the sample is illuminated with the second wavelength is known, OA signals modulating with this frequency can be assigned as label and other signals as background (locked-in detection).

The OA signal change upon illumination in most RSFPs and all BphPs is due to their photochromic behavior. Upon illumination, the molecular structure undergoes a reversible photo-induced transformation causing red- or blue-shift in absorption (Photochromism), resulting in pronounced contrast change in OA between ON and OFF state[26].

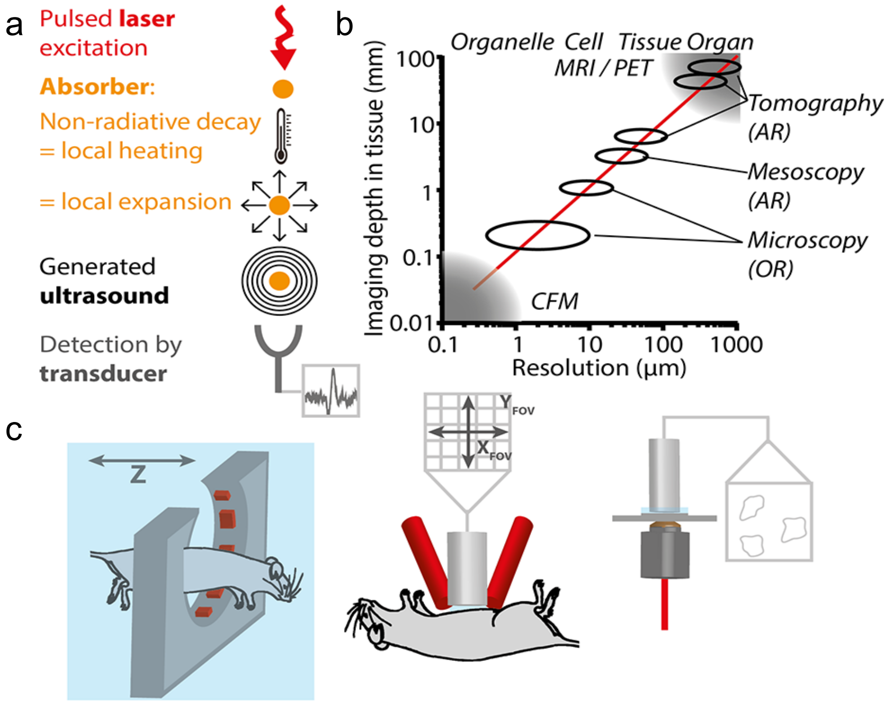

Figure 1: Photo- or optoacoustic (OA) imaging: **a)** General principle of OA, **b)** Relation of resolution and imaging depth for various imaging techniques including OA with the acoustic and optical resolution, **c)** Different modes of OA imaging: tomography (e.g., multispectral OA tomography; MSOT, left), scanning acoustic focus mesoscopy (e.g., raster scanning OA mesoscopy; RSOM, middle) and OA microscopy (right). FOV = field-of-view, AR = acoustic resolution and OR = optical resolution OA imaging, respectively, CFM = confocal fluorescence microscopy. Reprinted with permission from ref [26] (Copyright © 2018 American Chemical Society).

1.2 Photo-controllable proteins

The photo-controllable proteins have been exploited well in super-resolution microscopy[27]. However, their use in OA is still at a nascent stage. Photo-control in proteins can occur in three ways: (1) Photoactivation in which irreversibly phototransformation happens from a dim or non-fluorescent state to an emitting state[28], (2) Photoconversion in which a chemical reaction upon excitation, results in an irreversible modification of the chromophore or its surrounding leading to a shift of the emission spectrum[28], and (3) Reversible photo-switching where the chromophore can be photo-switched repeatedly between an active (OA or Fluorescent) and a non-active state[28]. Since with reversible photo-switching, one can get a multiple cycles of signal change over the time, makes reversible switchable proteins (RSPs) better suited for the modulation approach used for OA. Based on fluorescence, RSPs can be further divided into two classes: more fluorescent reversible switchable fluorescent proteins (RSFPs) absorbing in visible range[27,29,30] and less fluorescent NIR absorbing Phytochromes[31].

1.2.1 Reversible Switchable Fluorescent Proteins (RSFPs)

With very few exceptions[30,38], RSFPs are derivatives of non-switchable GFP-like proteins. They also adopt a classic 11-stranded beta-barrel and encloses an auto-catalytically derived 4-(p-hydroxybenzylidene)-5-imidazolinone (p-HBI) chromophore. The chromophore is formed from tripeptide amino acid sequence consisting of threonine (can be variable), tyrosine and glycine. It is formed in three steps: i) cyclization where glycine cyclizes into an imidazolinone ring, ii) Dehydration, iii) Oxidation, where both the tyrosine and glycine undergo oxidation, during which the tyrosine is reduced into a dihydroxybenzylidene moiety. The resulting p-HBI chromophore forms a conjugated system universal for all green-emitting GFP-like proteins. The chromophore transformations, including oxidation, cyclization, hydrogen bonds formation, protonation, deprotonation, and its position relative to the amino acid in its vicinity, determine the spectral characteristics of GFP-like proteins[33].

RSFPs can be classified based on their photo-switching behavior into three groups, namely, negative switching RSFPs, positive switching RSFPs, and third group represented by a solitary RSFP, Dreiklang[34] (Figure 2f). In negative RSFPs, the protein switches from fluorescent (ON) to non-fluorescent (OFF) state with illumination at a wavelength absorbed by the protein in its fluorescent state. In contrast, in positive RSFPs, it switches ON with illumination at a wavelength absorbed by the protein in its ON-state. Whereas in Dreiklang, on-off photo-switching is controlled by light at wavelengths that do not correspond to the excitation maximum used for probing the fluorescence.

In RSFPs, the light-induced cis-trans isomerization of p-HBI chromophore moiety between two states dictates their photo-physical property. In negative switching green RSFPs like Dronpa[30], rsEGFP[29], and rsFastlime[35], the deprotonated fluorescent cis p-HBI chromophore undergoes a isomerization to the non-fluorescent protonated GFP like trans chromophore. The non-radiative decay of excitation energy by the chromophore in the trans conformation results from protonation, loss of planarity, and flexibility in the rearranged protein pocket[36]. The chromophore cavity preference for the coplanar cis or noncoplanar trans configuration determines the equilibrium state of the switching. In most cases, the deprotonated forms are frequently the most fluorescent and, in most cases, predominant in equilibrium.

Conversely, in positive switching RSFP like padron[37] (Figure 2c), the anionic cis chromophore stays in thermal equilibrium with the protonated non-fluorescent chromophore and doesn’t go cis-trans isomerization. Later, protonated cis chromophore undergoes photoisomerization in to the anionic non-fluorescent chromophore upon violet light illumination

While RSFPs are highly successful in RESOLFT type super-resolution imaging, their absorbance in the visible range (400 nm – 600 nm) hinders their use in deep tissue imaging. This makes NIR (600 nm – 900 nm) absorbing phytochromes a better option for developing next generation optoacoustic protein for deep tissue imaging.

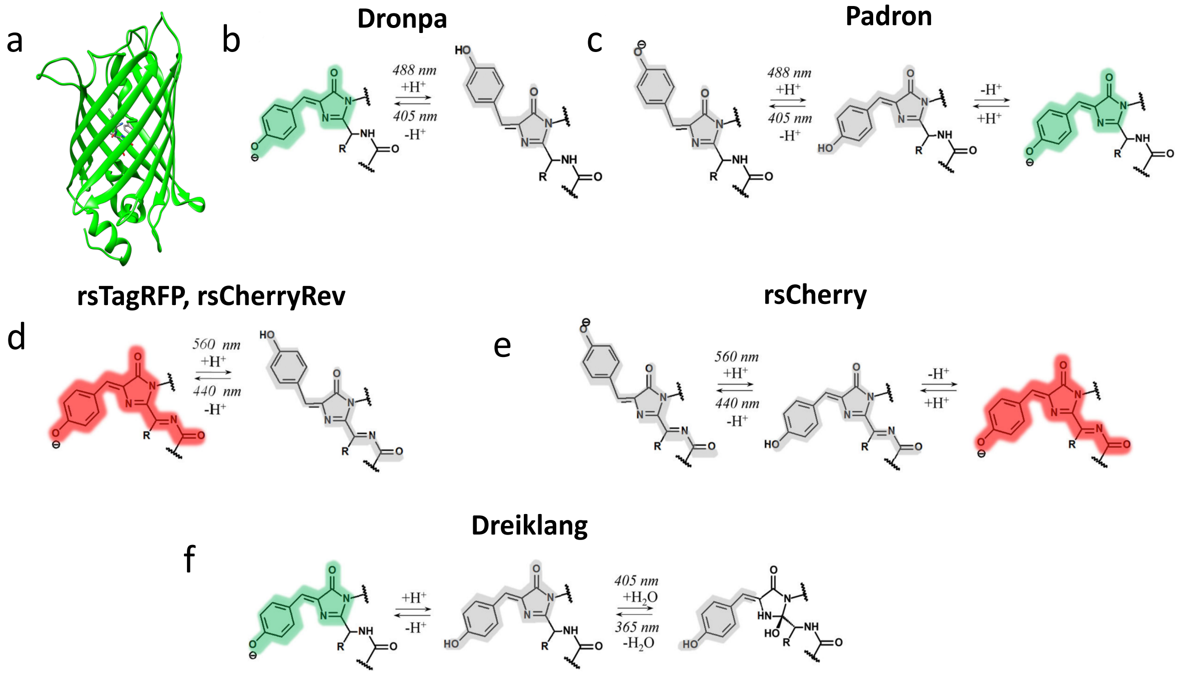

Figure 2: Light-induced chromophore conformations in reversible switchable Fluorescent Proteins

(RSFPs) where **a)** shows the cartoon representation of classic RSFPs 11-strand beta barrel hosting a centrally located p- hydroxybenzylidene-imidazolinone (p-HBI), **b)** to **f)** are showing the conformation transformation for Dronpa, Padron, rsTagRFP & rsCherryRev, rsCherry and Dreiklang respectively. Colors highlighting chromophores correspond to the spectral range of observed fluorescence. Non-fluorescent chromophores are shown in gray. Adapted from the ref [33] Copyright ©2014 with permission from Elsevier.

1.2.2 Phytochromes

Phytochromes are a widespread family of red/far-red responsive photoreceptor initially discovered in plants (Phy). They rely on light-induced structural changes and interconvert between two structurally distinct states, Pr and Pfr. Subsequently, the interconversion triggers various effector functions regulating molecular, cellular, and developmental responses such as cell division[31,38]. The Phytochrome-related proteins have also been isolated from other taxa such as cyanobacteria, fungi, and other bacteria, named as cyanobacterial phytochromes (Cphs), fungal phytochromes (Fphs) and bacteriophytochromes (BphPs) respectively[31] (Figure 3a). The red/far-red light family of phytochromes exists as dimers. Upon red light (650-700 nm) absorption, the Pr state undergoes large conformational changes to photoconvert via various intermediate states into the Pfr state. The reverse photoconversion to the equilibrium Pr from the Pfr state is initiated either by far-red light (750-780 nm) absorption or by dark thermal relaxation except for bathy phytochromes where Pfr is the steady state[39].

Phytochromes contain a covalently linked tetrapyrrole bilin chromophore, attached via a thioether linkage to a conserved cysteine in the GAF domain (cyanobacteria and plants)[40] or PAS domain (bacteria)[41]. The nature of the chromophore employed by different phytochromes varies, for example, phytochromobilin (PΦB) for plants phytochrome, phycocyanobilin (PCB) for Cphs and biliverdin IXα (BV) for BphPs. All major bilin chromophores are derived from heme, which is synthesized from Proto IX by ferrochelatase. Heme is cleaved in three successive monooxygenation steps to BV catalyzed by heme oxygenase (HO). Further, reduction of BV by bilin reductase results in PΦB in plants and PCB in fungal phytochromes.[42]

In BphPs, BV is primarily surrounded by residues of the GAF domain, which provide most of the hydrogen bonding, steric and hydrophobic interactions. Since the BphPs employs biliverdin as a natural chromophore whose conjugated system is more extended than PΦB or PCB, the absorption maxima of BphPs is found at higher wavelengths compared to plant and cyanobacterial homologs. Phytochromes, similarly like RSFPs, show photochromism due to the key interactions between the bilin chromophore and amino acids in its binding pocket resulting in spectrally different Pr and Pfr states.

Phytochromes, like other signaling proteins, are multi-domain modular proteins (Figure 3a) and are divided into three groups based on the domain architecture. Group I phytochrome share highly conserved N terminal photosensory core module (PCM) consisting of the domains PAS-GAF-PHY (Per/Arnt/Sim - cGMP phosphodiesterase/adenylate cyclase/ FhlA - Phytochrome-specific) connected with α-helix linkers. Plant, fungal and bacterial phytochrome belong to this group[31]. Three structural elements define phytochrome PCM namely,1) a figure-of-eight ”knot” at the interface of PAS & GAF domain, 2) a long helix called ”spine” extending through the entire photosensory module, and 3) a conserved loop region in the PHY domain, called ”tongue” extending from the PHY domain back towards the chromophore binding pocket[41] (Figure 3c). Upon illumination with red light (630nm-680nm) in BphPs, the tongue refolds from a β-hairpin conformation in Pr to an α-helical structure in Pfr and vice-versa after illumination with 780nm wavelength light. The PCM of the cyanobacterial group II and III phytochromes consist of GAF-PHY and GAF, respectively. The effector domains in phytochromes may vary and consist of a C-terminal Histidine Kinase in bacteria, the so-called N-terminal extension, and C-terminal PAS domains in plants and fungi.[43]

The various reasons that make BphPs most suitable for *in-vivo* imaging applications include:

1) It utilizes BV as a chromophore, which is a product of heme catabolism and is endogenously present in the mammalian system and thus in many mammalian cell types. This advantage is not shared by the plant and most cyanobacterial phytochromes which employ PΦB and PCB as chromophores, which are not endogenous to the mammalian system.

2) The extended π-electron conjugated system of BV enables BphPs to absorb strongly at wavelength above 700 nm, which is suitable due to lower scattering in tissue.

3) It shows spectrally very different states resulting in pronounced signal changes upon illumination (Figure 3b).

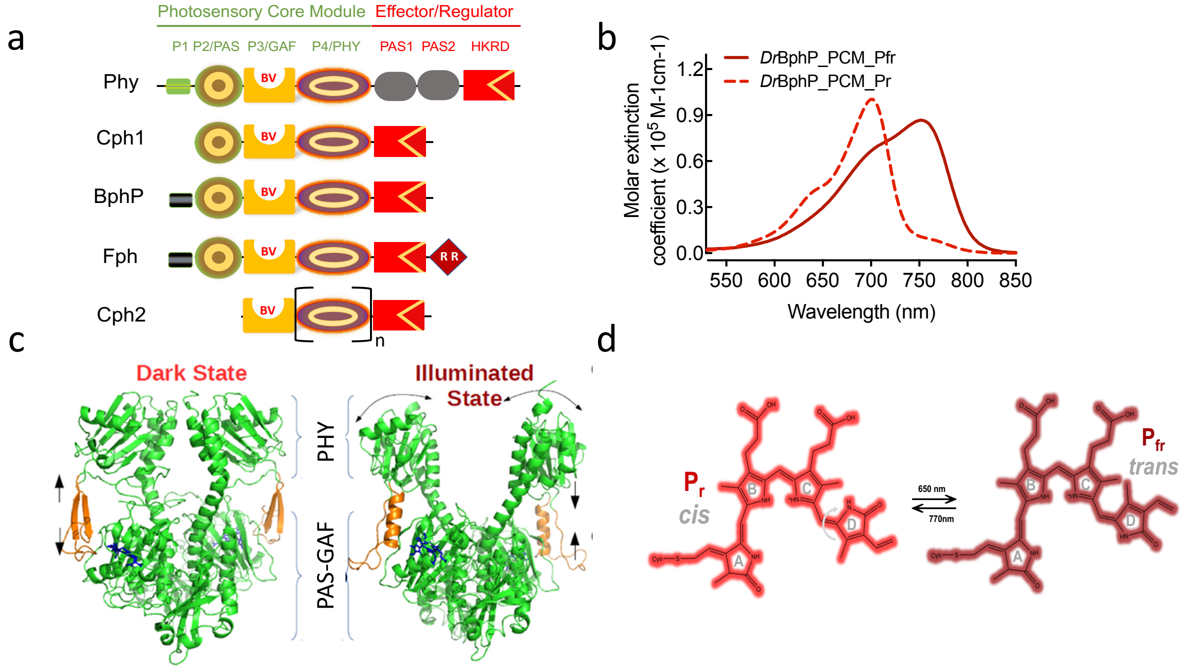

Figure 3: a) Domain architecture of extended phytochrome family. The phytochromes essentially consist of an N-terminal photosensory core module and a C-terminal regulator output domain. The P3/GAF domain is associated with the bilin chromophore and is highly conserved. All phytochromes except those found in the Cph2 subfamily share P2/PAS domains, whereas Phys possess two additional PAS domains within the regulatory region. Fungal phytochromes (Fphs) have a domain structure similar to those of the cyanobacterial phytochrome 1 (Cph1) and bacteriophytochrome (BphP) families, except for an additional C-terminal response regulator receiver domain (RR) extension and variable N-terminal extensions, **b)** Experimental Pr and Pfr absorption spectra of *Dr*BphP-PCM, **c)** Cartoon representation for the crystal structure of *Dr*BphP-PCM in the Pr Dark state (PDB: 400P)^{44} and in Pfr-Illuminated state(PDB: 4O01)^{44}, **d)** Light-induced BV conformation in the Pr and Pfr state of *Dr*BphP-PCM.

1.2.3 Fundamental Photophysics of Switching in RSFPs and Phytochromes

Generally, the photo-physical properties of RSFPs and phytochromes are guided by light induced structural changes involving cis-trans isomerization of the chromophore (Figure 2 & Figure 3d). The chromophore conformation (cis or trans) along with its relative position to the residue in the vicinity leads to distinct absorbance and emission spectra as well as in quantum yields (QY) and lifetimes of transitions of the two states. For example, in the simplified model given in Figure 4a, A and B refer to two states of

RSP, representing OA/fluorescent active (ON) and inactive (OFF) state respectively. The states can be interconverted by using light of distinct wavelength. The interconversion kinetics depend on the QY of the respective photophysical transitions relative to competing transitions, e.g., fluorescence, non- radiative decay, or intersystem crossing (Figure 2b). A high QY meaning high likelihood that an absorbed photon will induce only A and B interconversion, rather than other transitions. At the bulk level with millions of chromophoric proteins observed together in an imaging experiment, the transition kinetics (k_{off} and k_{on}) are determined by high QY and the photon flux (number of photon available for the chromophore to absorb). Due to the differences between state A and B in their absolute energy, it results in a thermal relaxation of the chromophore in the dark (k_{dark}). The kinetics of this transition strongly depend on A and B's relative stabilities and can be on the order of seconds to days.

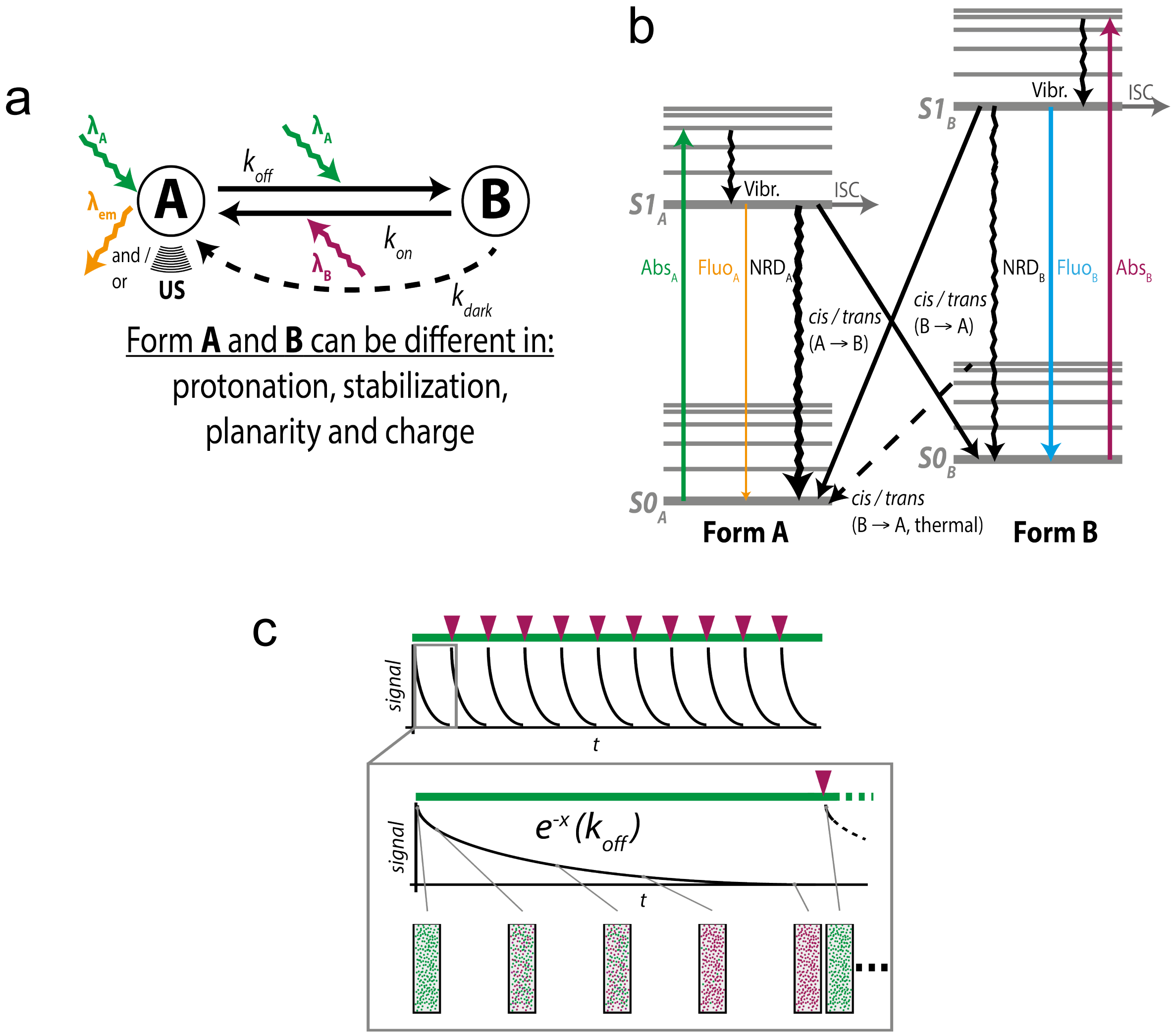

Figure 4: General principles of photocontrol in RSFPs and BphPs. **a)** A simplified model of RSP either in state A or state B, which can transition between a signal form and a no-signal form (e.g., fluorescence

or OA). The signal form emits fluorescence and/or ultrasound (US) waves. **b)** Simplified Jablonski diagram depicting the relevant transitions between forms A and B of a reversibly switchable molecule. Fluo = fluorescence, Abs = absorption, NRD = nonradiative decay, ISC = intersystem crossing, Vibr. = vibrational relaxation. Other electronic states can occur but are not depicted. For OA a $\mathrm{QY}_{\mathrm{NRD}}$ "$\mathrm{QY}_{\mathrm{Fluo}}$ is optimal (see the thickness of transition arrows in form A for example). **c)** Symbolized changes of a bulk volume of photo-controllable molecules as it would appear in a cuvette or a cell under illumination with two wavelengths. The curve depicts the exponential decay under green light illumination (green line) and subsequent recovery of the signal over time under UV illumination (purple arrowhead). A single switching curve is shown in the inset together with a stylized cuvette showing the change of photo-controllable molecules in bulk. Reprinted with permission from ref [26] (Copyright © 2018 American Chemical Society).

1.3 Unmixing for switchable OA signal and multiplexing

OA images represent the signal from different absorbers and are generally obtained in two steps. Initially, OA images are reconstructed from the pressure signals generated by employing inversion algorithms, for example, based on back-projection[45,46], time-reversal[47], or model-based approaches[48,49]. Then, the image acquired is processed to map the signal's spatial distribution corresponding to the target chromophore. This process of signal segmentation of different absorbers in an image is known as unmixing. Optoacoustic imaging using spectral unmixing approach has been instrumental in biomedical research[50]. The spectral unmixing algorithm exploits the prior knowledge of the targeted absorber optical spectra and extract its signal based on its distinct spectral features. Unmixing in spectral-domain has a strong limitation mainly due spectral coloring[51] (changes in detected optoacoustic spectra of an absorber due to wavelength-dependent fluence in deep tissue) and strong signal from endogenous chromophores like blood hemoglobin. In general, in the spectral-domain the targeted exogenous label signal always competes with the background signal. RSPs provide a promising alternative to this problem as they work in the temporal-domain. In the temporal-domain, the unmixing approach exploits the induced modulation of the signal over time, and the targeted RSP signal does not compete with the non- modulating background signal.

Till now, the temporal unmixing approach has been reported in five implementations in OA, namely single[52] or dual differential imaging[14,15], multi-contrast temporal frequency lock-in photoacoustics reconstruction (LIR)[55], vertex component analysis (VCA)[25], and difference-spectra demixing[56] (summarized in Figure 5).

In single wavelength differential imaging (Figure 5a), the unmixing is done simply by subtracting the image acquired when the label is in OA-active state (I_A) with the image acquired in the OA-inactive state[52]. Contrarily, in the dual-wavelength differential approach[54] (Figure 5b), the concept of single- wavelength differential imaging is extended to include an intermediate state in which both OA-active and -inactive molecules (I_{A+B}) are generated by simultaneously illuminating with both wavelengths. Difference images are obtained by subtracting the two single population images from the mixed one.

One limitation of differential imaging is that it completely neglects the switching kinetics between OA-active and -inactive forms. VCA and LIR temporal unmixing approach take this switching kinetics into account, which substantially improves the results. Another advantage of considering switching kinetics is that the signals from multiple labels can be distinguished if their switching kinetics are different enough. This allows the simultaneous imaging of several labels in parallel (multiplexing) while using only two wavelengths, thus reducing "spectral crowding" that typically limits how many labels can be used for a given set of wavelengths. The multiplexing of switchable proteins in OA was shown first by Stiel et al.[25] by temporally unmixing (Figure 5d) spectrally similar slow switching Dronpa and its fast switching variant DronpaM159T using VCA. Similarly, LIR (Figure 5c) also takes features from switching kinetics into account for unmixing. Lei et al. [55] using LIR based temporal unmixing and BphPs (*Rp*BphP1 & *Dr*BphP1) as labels, showed multiplexing in the *in-vivo* xenograft mouse model.

Difference-spectra demixing[56] (Figure 5e) is an intermediate approach used for multiplexing. Here two proteins that both absorb strongly at the switching wavelength but not at the second wavelength are imaged sequentially. The entire spectra of the proteins are recorded, and the final unmixed image is formed by taking advantage of the spectral differences between the two proteins minimizing the crosstalk between the spectral overlap from the two labels.

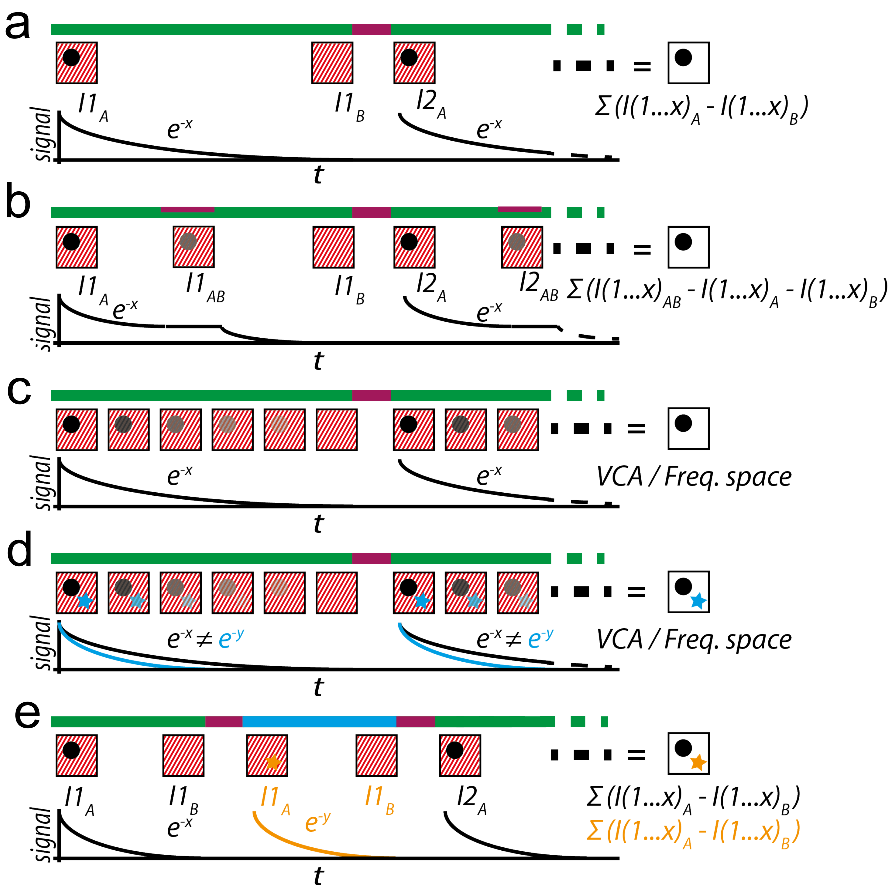

Figure 5: Unmixing strategies for RSP signal from background. **a-e)** the basic principle of **a)** differential, **b)** double differential, **c)** temporal unmixed, and locked-in reconstruction (LIR), **d)** Temporal multiplexing of two labels based on their characteristic photocontrol kinetics, **e)** Multiplexing based on difference spectra demixing. The structure labeled with photo-controllable protein is shown in black, blue & orange and background in red. Illumination wavelengths are shown as green and purple bars over each strategy. The graphs show simulated signal traces of the respective structure labeled with RSP. Basics calculation is depicted or indicated as VCA = vertex component analysis, for temporal unmixing and frequency space for LIR. All the images show only the starting illumination and generated signal sequence. Note that the number of repetitions determines the CNR. Reprinted with permission from ref [26] (Copyright © 2018 American Chemical Society).

1.4 Application examples using RSPs and unmixing in *in-vivo* studies

RSPs and the unmixing strategies discussed in previous section have provided the required robustness for efficient routine use of OA for the detection of small numbers of labeled cells in deep tissue, expanding the use of OA imaging in broad life science research.

Therefore, various *in-vivo* studies have been done to evaluate their applicability using BphPs expressing cell-line derived tumor xenograft models (Figure 6). For instance, the liver xenograft model employing U87 glioblastoma cell line expressing *Rp*BphP1[52] (origin*: Rhodopseudomonas Palustris*)(Figure 6a) and subcutaneous tumor xenograft of AGP1 (origin: *Agrobacterium tumefaciens*) expressing HT29 cell[53,54] in mice were visualized with high signal to noise ratio using differential imaging and OA difference imaging approaches respectively.

Li et al.[55] showed multiplexing using the U87 brain and liver xenograft model. Briefly, U87 cells expressing *Rp*BphP1 and *Dr*BphP-PCM were injected in the right rear and left front lobe of the brain respectively. They were unmixed using the LIR method based on the different switching kinetics of the proteins. A similar outcome was achieved when the U87 cells expressing *Dr*BphP-PCM or HEK-293 cells expressing both *Dr*BphP-PCM and *Rp*BphP1 were injected in liver and unmixed using the LIR approach (Figure 6c).

Additionally, to study protein-protein interaction Li et al.[55] designed bimolecular photoacoustic complementation (BiPC) reporter from *Dr*BphP-PCM. Briefly, they genetically separated (split) *Dr*BphP-PCM between the *Dr*PAS domain and the *Dr*GAF-PHY domains and fused them with FRB (FKBP-rapamycin binding domain) protein and the FKBP (FK506 binding protein) proteins, respectively, and named as DrSplit. In the presence of rapamycin, FRB and the FKBP proteins interact, and complementation between PAS and GAF-PHY results in reconstituting the functional PCM, which can eventually be detected using switching. Using DrSplit, a longitudinal PPI study was done using MTLn3 cells expressing DrSplit (Figure 6c). Interestingly, they were able to detect PPI with as few as ~530 cells.

Another application of switchable proteins was shown in a bacterial *in-vivo* model, opening up the possibility of their use in studies involving bacterial infection and therapy. Chee et al. [56] visualized *E. coli* expressing switchable (sGPC2 and BphP1) and mIFP in the hind flank of mice and achieved multiplexing using difference spectra demixing (Figure 6d).

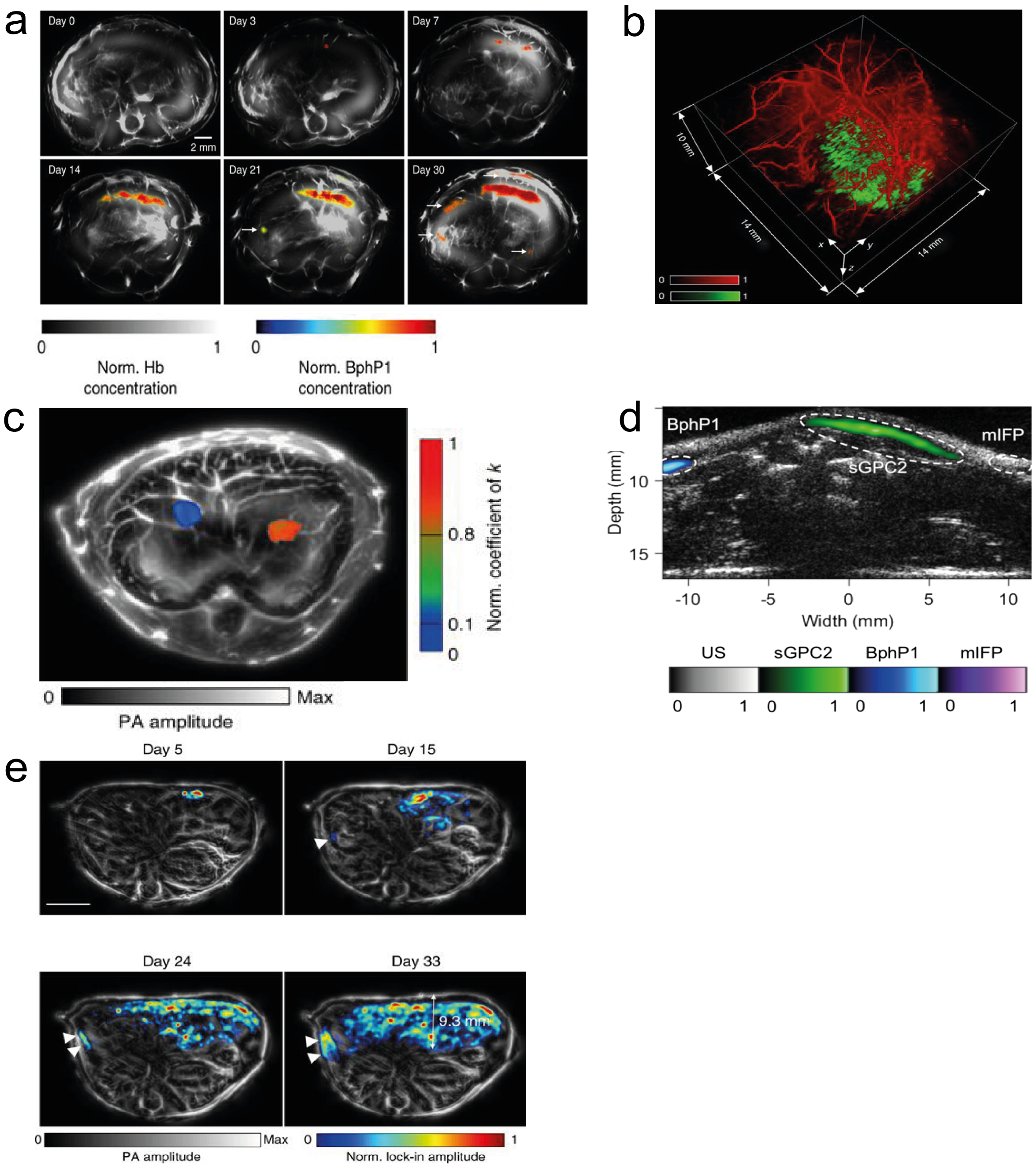

Figure 6: Reversible switchable proteins (RSPs) application in OA. **a)** The longitudinal tumor development and metastasis in mouse liver using U87 cells, expressing BphP1 and differential unmixing,[30] **b)** Subcutaneous tumor together with vascular morphology in 3D using HT29 cells expressing AGP1 unmixed with the double differential strategy,[54] **c)** LIR (Multiplexed detection) of cancerous cells in the liver, the U87 cells expressing *Dr*BphP-PCM (right, red) or HEK-293 expressing cells expressing both *Dr*BphP-PCM and *Rp*BphP1 (left, blue),[58] **d)** *In-vivo* unmixing of individual bacteria expressing two RSP (sGPC2 or BphP1) and non-switchable NIR label mIFP,[56] **e)** Longitudinal imaging of PPIs in a tumor and monitoring of tumor metastases in a mouse liver using LIR unmixing strategy[58]. Arrows indicate a secondary tumor. Adapted with permission from ref[26] (Copyright © 2018 American Chemical Society).

1.5 Rationale

OA imaging based on endogenous contrast from hemoglobin or lipids has been well established in preclinical and clinical research[50,59]. However, its application in life science research is limited by the lack of appropriate transgene labels (discussed in detail in section 1.1) specifically for multiplexing to visualize multiple cell populations parallelly in deep tissue. For example, melanin has been a popular transgene label in OA imaging due to its strong OA signal generating ability but poses several limitations. Most importantly, unmixing of signals from melanin relies on the separation of the spectral features of melanin from the strong signals of the tissue background. This makes unmixing challenging, especially for low concentration of the label – i.e. low cell numbers.

RSPs offer to tackle these limitations as they can be photo-modulated, and such modulation allows separating their signal from non-modulating background using temporal unmixing. This unmixing strategy offers unique potential for the visualization of even small cell numbers with high sensitivity in OA.

In my research, I focused on characterizing photo-switching in context of RSPs, developing new and superior RSPs for OA imaging (rsOAPs) and showcasing their applications in *in-vivo* OA imaging. This was achieved in the following two studies:

1. **Characterization of Reversibly Switchable Fluorescent Proteins in Optoacoustic Imaging**

   Initial studies showed RSP's advantages as a potential label in OA imaging[25]. In the first part of my thesis, I studied the differences that the OA imaging principle imposes on the photo-physical properties of RSPs as OA regularly requires pulsed illumination compared to continuous illumination in fluorescence imaging. I chose a broad range of existing RSPs representing whole bandwidth of their photophysics such as wavelength, switching kinetics, and quantum yield and characterized their photo-physical properties under the condition used in OA. This is addressed in publication 1 (Chapter 2)

2. **Multiplexed whole-animal imaging with reversibly switchable optoacoustic proteins (rsOAPs)**

Due to NIR absorption and good performance in the characterization (publication 1), BphPs are an optimal starting point for the development of photo-switching labels for OA imaging. In the second publication I tailored such labels based on native BphPs for an optimal application in OA imaging. The study directly focused on commercial OA imaging systems to allow an immediate application of this labeling strategy by the community. Next to the development, another part of this study (conducted by Mariia Stankevych) focused on the development of efficient machine learning algorithms for unmixing the photo-switching from the OA images. Finally, using the developed labels, the ML-based analysis algorithm, and a commercial OA system, I demonstrated several proof-of-concept in *in-vivo* applications focusing on cancer and immune-cell imaging, and demonstrated the capabilities of the developed labels and approach for multiplexing. This is addressed in publication 2 (Chapter 3).

1.6 Methods

1.6.1 Construct generation for protein expression in bacterial and mammalian system

1.6.1.1 Construct generated for protein expression in bacterial system

For protein expression of RSFPs[60] and rsOAPs[61], the coding sequences of RSFPs-Dronpa, DronpaM159T, rsFastlime, Padron, rsEGFP2, rsCherry, rsCherryRev, rsCherryRev1.4 and rsTagRFP were subcloned by use of XhoI/HindIII into an arabinose-inducible pBad-HisA vector. While all coding sequences of all rsOAPs except *Rp*BphP1 were polymerase chain reaction (PCR) – amplified as a Nde I/Xho I fragment and cloned into the second multiple cloning site of the pET-Duet1 vector (Novagen, Merck Millipore). *Rp*BphP1 was PCR-amplified as a Nde/Pac1 fragment and cloned into the second multiple cloning site of the pET-Duet1 vector. In addition, for biliverdin synthesis, the heme oxygenase (HO) of *Nostoc sp.* was cloned using Nco I/Hind III into the first multiple cloning site of pET-Duet1.

1.6.1.2 Constructs generated for mammalian expression of wild-type BphPs and developed rsOAPs.

To compare the mammalian expression of different rsOAPs and wild type BphPs in mammalian cells, I used a multi-cistronic expression system using P2A, allowing equimolar expression. Due to low quantum yield of rsOAPs, I chose mCherry as the reference fluorescent protein. First, *Re*BphP1_P2A and P2A_mCherry were PCR-amplified and then stitched together using overlap PCR as an EcoRI/XbaI fragment and cloned in a pcDNA3.0 vector (Thermo Fisher Scientific). Later, similar constructs for other rsOAPs and wild type BphPs were made by amplifying them as EcoRI/NotI fragment and inserted in the place of *Re*BphP1-PCM in the above construct. The resulting plasmids allowed the equimolar co-expression of *Rp*BphP1 or *Rp*BphP1-PCM or *Re*BphP-PCM or *Re*BphP-PCM, or *Dr*BphP-PCM and mCherry proteins.

For generation of stable Jurkat, HCT116 and 4T1 cell lines in order to perform longitudinal *in-vivo* imaging I used the multi-cistronic mammalian expression system employing IRES. For the same, the *Re*BphP-PCM-IRES-GFP was amplified as Not1/EcoR1 fragment and cloned into the mP71 using Not1 and EcoR1 restriction sites.

1.6.2 RSPs expression and purification

Proteins for spectroscopic characterization were expressed in *Escherichia coli* strain BL21 (DE3) (NEB # C2527). In brief, plasmids expressing RSFPs or rsOAPs or wild type BphPs with HO were transformed into the BL21 host cells. Bacterial cells were grown in LB media supplemented with ampicillin at 37^o C until the culture reached OD 0.6 followed by induction of protein expression by addition of IPTG and further incubation for 16 – 18 h at 22^o C. Next day, the bacterial pellet was collected by centrifugation and pellet was resuspended in phosphate-buffered saline (PBS). After cell lysis, proteins were purified by immobilized metal affinity chromatography (IMAC) in PBS, followed by gel-filtration on a HiLoad 26/600 Superdex 75pg (GE Life Sciences, Freiburg, Germany). Additionally, rsOAPs were run on an analytical size exclusion chromatography (Superdex 75, 10/300 GL (GE Life Sciences, Freiburg, Germany)

1.6.3 Absorption and Fluorescence Spectroscopy

For absorption spectra, the purification buffer was exchanged against PBS, and the proteins were measured with a Shimadzu UV-1800 spectrophotometer (Shimadzu Inc., Kyoto, Japan) in a 100-µl quartz cuvette. To measure, ON and OFF spectra of respective proteins, photo-switching was carried out using the respective switching light from light-emitting diodes delivering light homogenously just above the meniscus of the protein solution in the cuvette.

Fluorescence measurements for all proteins were carried out using a Cary Eclipse Fluorescence spectrophotometer (Varian Inc., Australia). Photo-switching was carried out as above. Excitation wavelength and emission slit were set to 5 nm, and the absorbance at the excitation wavelength was always equal to 0.1 to avoid inner filter effects. Processing of all spectral data was conducted in Microsoft Office Excel.

1.6.4 Characterization of RSPs using custom build hybrid spectrophotometer

For characterization of the photophysical characteristics under illumination conditions similar to OA imaging, I used a custom-build hybrid spectrophotometer capable of recording optical and optoacoustic spectra simultaneously[62]. Additionally, the setup also allowed recording of switching kinetics of different RSPs. Altogether, it allowed me to study various photo-physical parameter of RSPs such as switching speed, photoacoustic generation efficiency (PGE), photo-fatigue, and dynamic range. Briefly, the custom-build spectrophotometer consisted of an optical parametric oscillator (OPO) laser (Spitlight-DPSS 250 ZHGOPO, Innolas) generating nanosecond excitation pulses at a repetition rate of 50 Hz or 25Hz. Constant pulse energy for characterization was ensured by the use of a half-wave plate in a motorized rotation stage (PRM1Z8, Thorlabs) and a polarizing beam splitter; using a lookup table and adapting the polarization with the half-wave plate, I kept the power constant at ~1.3 mJ (otherwise mentioned) over all wavelengths of the illumination schedule. Samples were injected into an acoustically coupled flow chip (µ-Slide I 0.2 Luer, hydrophobic, uncoated, IBIDI) and illuminated from one side by using a fiber bundle (CeramOptec). Photo-switching was carried out by illuminating the sample alternatively with the light of switching wavelengths. OA-active and non-active spectra (explained in Chapter 1.1) was recorded by illuminating the sample over the range of wavelength (420-550nm for all green absorbing, 450nm-650nm for red absorbing, and 550nm-850nm for BphP1). The OA spectra were recorded with a step size of 5 nm and to keep the respective protein in either active or non-active state I used inter-pulsing with proper ON or OFF wavelength. I also calculated PGE for measured RSPs, in order to accurately compare their optoacoustic capacities. PGE is a measure of how much of the absorbed energy is converted to pressure. It is calculated by normalizing OA signal by the absorbance, so that the slope of the linear relation between the absorbance and OA signal yields the PGE. Optoacoustic signals were detected with a cylindrically focused single element transducer (V382-SU, 3.5 MHz, Olympus) followed by signal amplification by 60 dB via a wide-band voltage amplifier (DHPVA-100, Femto) and digitized at 100 MS/s with a data acquisition card (RZE-002 400, GaGe). The dependency of RSFPs and rsOAPs switching on the laser's repetition rate was measured with three different laser repetition rates (10, 25, and 50 Hz). The dependency of ON-OFF conversion on pulse energy was measured with different pulse energies (0.4 mJ, 0.7 mJ, 1.0 mJ, and 1.3 mJ).

1.6.5 Optoacoustic image acquisition and data analysis

For all *in-vitro* phantom and *in-vivo* data acquisition for the second part of my thesis[61], I used the commercial multiple spectral optoacoustic tomography imaging system (MSOT, InVision 256-TF, iThera Medical GmbH, Munich, Germany). In brief, the system employs a tunable (680-980 nm) optical parametric oscillator (OPO) laser at a repetition rate of 10 Hz generating nanosecond pulsed light that is delivered to the sample through a ring-type fiber bundle. For recording photo-switching, I employed the wavelengths, 680 and 770 nm. Light absorbed by the sample generates an acoustic signal that propagates through the sample and is detected outside of the sample by a cylindrically focused 256-element transducer. The transducer array has a central frequency of 5 MHz (−6 dB was approximately 90%) with a radius of curvature of 40 mm and an angular coverage of 270°. Acoustic signals were detected as time series pressure readouts at 2030 discrete time points at 40 MS/s. The acquired acoustic data were reconstructed using the back-projection inversion algorithm in ViewMSOT software version 3.8.1.04 (iThera Medical GmbH, Munich, Germany) software with the following settings: 50 kHz to 6.5 MHz; trim speed of 7.

Later, for signal unmixing for the photo-modulated signal, I used a ML-based unmixing algorithm developed by Mariia Stankevych. Briefly, the model was constructed based on random forest approach and trained upon various experimental datasets with ground truth provided by histology co-registration. The ensuing model was then used to analyze all data in this study.

1.6.6 Stable cell lines generation

The stable lines used in the publication 2 was generated by the collaborator (Simon Grassmann). Briefly, the retrovirus was produced in Platinum-E or RD114 packaging cells after transfection with the retroviral vector mP71-*Re*BphP-PCM-IRES-GFP. Later the virus supernatant was purified and used for transduction of 4T1, HCT116 and Jurkat T. After 5 days of culture, cells were sorted for high expression of GFP using flow cytometry.

1.6.7 *In-vivo* application of rsOAPs

All animal experiments were approved by the government of Upper Bavaria and carried out under the approved guidelines. To showcase the use of rsOAPs in tumor imaging I employed different mice tumor model. First, to visualize tumor at superficial location and track its development, I chose the 4T1 breast cancer tumor model. Briefly, 0.8×10^6 4T1 cells stably co-expressing *Re*BphP-PCM and GFP were grafted onto the backs of FoxN1 nude mice (n = 3) and imaged till 9th day. Next, to show the application of rsOAP in brain imaging, I used the same 4T1 cells stably co-expressing *Re*BphP-PCM & GFP. Briefly, 0.7×10^6 (in 5µl PBS) were intracranially injected at the depth of 3.6mm. The mice were scanned in MSOT and sacrificed immediately after scanning. Next, to visualize and track the development in deep seated tissues I chose colon cancer cell line (HCT116) expressing *Re*BphP-PCM and GFP. Briefly, 1.5×10^6 cells in 200 µl PBS were injected intraperitoneally in FoxN1 nude mice and imaged at different time interval till day 14.

Next, to assess the sensitivity of imaging with rsOAPs, I imaged dorsal implants of matrigel containing different numbers of Jurkat T lymphocytes or bacterial cells expressing *Re*BphP-PCM. For the same, matrigel implants with different concentrations of Jurkat cells expressing *Re*BphP1-PCM ranging from 6400 to 500 cells/µl were implanted subcutaneously in the back of the mice. Similarly, bacterial cells expressing *Re*BphP-PCM in different concentrations (1.4×10^5 to 1.4×10^4 cells/µl) were also implanted in the mice's back.

A strong advantage of RSPs is the possibility to visualize and segment multiple labels based on their individual switching kinetics. To demonstrate this *in-vivo*, I did three individual experiments. In the first experiment, I used three populations of cells; namely, Jurkat cells expressing *Re*BphP-PCM (origin: *Rhizobium etli)* or *Dr*BphP-PCM (origin: *Deinococcus radiodurans)*, and bacterial cells expressing *Rp*BphP1-PCM were injected subcutaneously in the back of the mice. In the second experiment I assessed the ability to unmix two populations of Jurkat cells, I chose 4T1 tumor model and injected Jurkat cells expressing *Re*BphP-PCM or *Dr*BphP-PCM intratumorally. In the end, I used a 4T1 tumor expressing our *Re*BphP-PCM, intratumorally injected with slow switching *Dr*BphP-PCM.

For all MSOT imaging, mice were anesthetized using 2% isoflurane in O_2. Anesthetized mice were placed in the MSOT holder using ultrasound gel and water as coupling media. After the termination of the experiments, all mice were sacrificed and stored at −80°C for cryo-sectioning.

Chapter2: Results

2.1 Characterization of Reversibly Switchable Fluorescent Proteins in Optoacoustic Imaging

2.1.1 Summary

Reversible switchable proteins (RSPs) have shown great potential in optoacoustic imaging (OA) mainly by virtue of their photo-switching property and the possibility of lock-in-detection. This study aims to study differences that the OA imaging principle imposes on the photo-physical properties of RSPs. OA uses short pulsed illumination requires to generate broadband ultrasonic waves compared to continuous illumination in fluorescence imaging. Towards understanding the implications of the different illumination, in this study**,** I characterized a broad range of RSFP's (Dronpa, DronpaM159T, rsFastlime, Padron, rsCherry, rsCherryRev, rsCherryRev1.4, and rsTagRFP) along with NIR absorbing bacteriophytochrome (BphP1). We analyzed the proteins using a custom-built spectrometer (Chapter 1.6.4), thereby allowing us to record high-quality optoacoustic spectra in conjunction with the optical spectra.

The study shows that, for most of the reversible proteins characterized, the OA and optical spectra in active and non-active state coincide well with square of determination (R^2) higher than 0.94, except for proteins with high QY. The complete photochromic proteins which shows 100% change in the absorbance like rsEGFP2, Dronpa, DronpaM159T, & BphP1 results in higher dynamic range (OA signal difference between ON and OFF state) in OA. In contrast to the proteins showing photochromism, QY changers like rsCherry and its sibling rsCherryRev and rsCherryRev1.4 show little or no change in OA signal upon switching. I also calculated the PGE (Chapter 1.6.4) to accurately compare the OA capacities of measured RSPs. PGE appears in concordance with QY as OA signal generation is inversely proportional to QY. Protein with low QY like 0.3 for rsEGFP2 and 0.23 for Dronpa-M159T results in higher PGEs of ~0.5 and ~0.7 than Dronpa with QY of 0.85 showing the weakest optoacoustic signal of PGE < 0.1.

I also observed that switching speed and its dependency on laser repetition rate & energy in OA closely follow the trend known from fluorescence wherein switching kinetics shows an exponential dependence on illumination intensities. Next, we compared the effect of pulsed and continuous illumination on photo-fatigue by measuring super-folder green fluorescent protein (sfGFP) under four illumination conditions at the same power: 10 ns/50 MHz (pulse width/repetition rate), 100 ns/5 MHz, 1 µs/500 kHz, and continuous, all depositing the same power of 500 µW. The results showed accelerated bleaching for pulsed illumination, scaling inversely with pulse length.

In summary, this study characterized reversible switchable proteins (RSPs) using the hybrid OA-Absorbance spectrophotometer. Overall, the study shows that photochromic proteins are a better option for OA imaging compared to QY changers as they offer higher dynamic change after switching. By far, bacteriophytochromes (BphPs) are the best-suited proteins for most OA applications due to their wavelengths in the NIR, good dynamic range, and robust resistance to photo-fatigue. We correlated pulse length with photo-fatigue, which showed that shorter pulses result in higher photo-fatigue.

2.1.2 Contribution

For this study, me and Paul Vetschera contributed equally. I selected the proteins for the study and prepared all the sample. I performed all the molecular biology experiments along with the absorption, fluorescence, and OA spectroscopy. Paul Vetschera built the OA - Absorbance hybrid spectrophotometer with my, Juan Pablo Fuenzalida-Werner and Andre C. Stiel help. Me and Paul Vetschera did all the data analysis. Andriy Chmyrov performed bleaching and high-repetition-rate OA experiments along with me and Paul Vetschera. Juan Pablo Fuenzalida-Werner and Vasilis Ntziachristos contributed to the scientific discussion. Andre C. Stiel wrote the manuscript and led the project with me and Paul Vetschera.

2.1.3 Publication

The data presented is an original work and reprinted here with the permission from:

Characterization of Reversibly Switchable Fluorescent Proteins in Optoacoustic Imaging. Paul Vetschera*, Kanuj Mishra*, Juan Pablo Fuenzalida-Werner, Andriy Chmyrov, Vasilis Ntziachristos, and Andre C. Stiel. *Analytical Chemistry* 2018, *90* (17),10527-10535. DOI: 10.1021/acs.analchem.8b02599. Copyright © 2018 American Chemical Society.

* Contributed Equally

2.2 Multiplexed whole animal imaging with reversibly switchable optoacoustic proteins

2.2.1 Summary

Optoacoustic (OA) imaging enables high-resolution, real-time *in-vivo* imaging well beyond the 1 mm penetration depth[63,64] and already provided valuable information in various preclinical and clinical studies[15,52,65–69]. However, its application to life science research is limited by the lack of appropriate labels, specially transgene labels. While transgene labels such as enzymatic reporter system (*lacz* reporter gene system,[19] melanin,[20] or violacein[21]) or fluorescent labels (EGFP or mCherry)[22] have been explored in OA. Their broader use in OA imaging is often hampered, as most of them absorb in the visible range, and other like melanin, lacks the distinct spectral feature. Reversible switchable proteins (RSPs) provided a better alternative for OA imaging as they by virtue of their photo-modulation results in high contrast-to-noise ratio in OA unmixed images. In RSPs, the absorption bands can be modulated by light (photochromism). Such modulation allows separating these protein-labels signal from non-modulating background. This approach can benefits OA life-science imaging with unprecedented sensitivity and specificity.

In this study, I have developed two new near-infrared reversible switchable optoacoustic proteins (rsOAPs) from the wild type BphP of *Rhizobium etli (ReBphP-PCM and Rhodopseudomonas palustris* (*Rp*BphP1-PCM). *Re*BphP-PCM is a small monomer with high absorption, which shows 2-fold larger change in OA signal, >5-fold faster switching, and greater resistance to photo-fatigue than other rsOAPs. Whereas the *Rp*BphP differs from its parent wild type *Rp*BphP1 only in having slower switching kinetics. For image acquisition I used an off-the-shelf commercial OA imaging system and a highly sensitive machine learning-based temporal unmixing algorithm to extract the specific signal of the photo-modulating label for the analysis. Using this, a sensitivity of 500 immune-cells and 14000 bacterial-cells *in-vivo* was achieved. Next, I demonstrated the possibility of studying tumor development using two different tumor models, superficial 4T1 breast and deep-seated HCT116 colorectal tumor models. Finally, the fast switching speed of *Re*BphP-PCM allows it to be used together with other rsOAPs (*Rp*BphP1-PCM and *Dr*BphP-PCM with slow switching speeds effectively imaging mixed cell-populations labeled with the different rsOAPs. This demonstrates the potential for simultaneous tracking of different cellular processes through temporal multiplexing.

In conclusion, in this study, I developed next-generation superior rsOAPs, which in combination with the ML-based unmixing algorithm and commercial OA imaging setup allowed sensitive detection and, importantly multiplexing in whole animal OA imaging. These tools will facilitate the wider use of reversible switchable proteins with OA imaging in biomedical research.

2.2.2 Contribution

For this study, I screened wildtype BphPs for the parameters like absorptivity and dynamic range and later optimized the selected BphPs using truncation-based approach. This approach led to the development of superior rsOAPs. To achieve this, I designed and performed all the molecular biology experiments including, cloning, transformation, protein expression & purification and mammalian cell line transfection experiments. Further, I comprehensively evaluated the photo-physical characteristics of the selected proteins using absorption, fluorescence and OA spectroscopy. For its *in-vivo* proof of concept, I selected the appropriate *in-vivo* models and performed the required mouse work alongside Uwe Klemm, occasionally with the help of Vipul Gujrati. Moreover, I performed Bacterial Cell immobilization by entrapment and acquired all the *in-vitro* and *in-vivo* data using commercial MSOT OA imaging system. Mariia Stankevych wrote the analysis code, did the *in-vivo* data analysis under my and Andre C. Stiel supervision. Juan Pablo Fuenzalida-Werner performed a PGE analysis of all the rsOAPs described in this study. Yuanhui Huang supported the in-vitro characterization of rsOAPs through his technical experience in OA spectroscopy. Simon Grassmann provided stable rsOAP-GFP cell lines. The co-authors Veit R. Buchholz and Vasilis Ntziachristos contributed to the scientific discussion. Andre C. Stiel led the project and wrote the manuscript with me.

2.2.3 Publication

The data presented is an original work published in *Science Advances* in June 2020 and reprinted under the Creative Commons Attribution 4.0 International License.

Multiplexed whole animal imaging with reversibly switchable optoacoustic proteins. Kanuj Mishra, Mariia Stankevych, Juan Pablo Fuenzalida-Werner, Simon Grassmann, Vipul Gujrati, Yuanhui Huang, Uwe Klemm, Veit R. Buchholz, Vasilis

Ntziachristos and Andre C. Stiel. *Science Advances* 2020, 6-24. DOI: 10.1126/sciadv.aaz6293. Copyright © 2018 Science advances.

Chapter:3 Summary and Outlook

3.1 Summary

In summary, the presented work provides a comprehensive understanding of the reversible switchable proteins in OA, generation of a superior rsOAP as a label and its application in deep tissue imaging using different mouse models.

In the initial part of the study the differences inflicted by OA imaging principle (pulsed illumination) on RSPs functioning was studied. Towards this end, a broad range of proteins ranging from green Dronpa-like to NIR BphPs, based on the parameters like switching kinetics, wavelength, QY, and photochromism were selected and photophysically characterized in OA. Comparative analysis of the photo-physical properties of the proteins revealed that the photochromic proteins are better suited for optoacoustic applications than QY-changers. The pulsed illumination in OA results in slow switching kinetics due to its dark times and the proteins natural relaxation. Hence, implying that high repetition laser systems are beneficial for imaging RSPs due to the lesser number of pulses required for switching. The high repetition laser system thereby could result in reduced photo-fatigue and imaging dwell time. In conclusion, BphPs are the ideal candidate for developing dedicated next-generation rsOAPs for OA imaging due to their high switching speed, low photo-fatigue, high PGE, photochromism in the NIR region of spectra, and low QY.

Consequently, I developed two new rsOAPs based on BphPs One of the developed rsOAP (*Re*BphP-PCM) showed higher absorption and fast switching kinetics. Whereas the other rsOAP (*Rp*BphP-PCM) showed slower switching and used for multiplexing applications. The unmixing approach to extract the desired signal from the image is one of the key elements for any imaging modality. Therefore, in this study, for the first time, I employed an in-house developed open-access machine learning approach for unmixing photo-modulated signal from the OA images. Using rsOAPs with highly sensitive ML-based algorithm and commercial OA imaging system, I was able to show highly sensitive, multiplexed visualization of T lymphocytes, bacteria, and tumors in the mouse body and brain.

In conclusion, this study provides a complete framework for using rsOAPs in whole animal imaging using a commercial OA imaging system for data collection, and highly sensitive ML-based software for data analysis. This will facilitate wider use of rsOAPs with OA imaging in life-science research particularly tracking specific cell populations in longitudinal studies of intact animals. Hence, the tools developed will help in cell specific high-spresolution deep tissue imaging in diverse fields such as immunology, developmental biology, neurology, and cancer research.

3.2 Outlook

The current study provides a good starting point for the broader use of OA imaging using rsOAPs. Concurrently, further research is certainly required to achieve single-cell sensitivity with multiplexing in whole-animal imaging. This can be achieved by advancements including, a) generation of high absorbing palette of rsOAPs with differential kinetics in order to allow routine multiplexing in the temporal domain. It would also be relevant to engineer other class of NIR absorbing proteins to be switchable, e.g., phycobiliproteins. Currently, the lack of comprehensive structure information for BphPs and Phycobiliproteins hinders their further development for changed photophysics b) advanced unmixing algorithms with minimal effect from animal movement and extraction of the maximum possible information per switching cycle, c) Another approach to achieve single cell resolution sensitivity in deep tissue would be to develop current OA setup like RSOM (Chapter 1: Figure 2c) specifically for photo-modulating proteins. Currently, the RSOM enables axial and lateral resolution of 4.5µm and 18.4µm[14] several mm deep in the tissue. Therefore, it can be envisioned that the use of RSPs with RSOM like approach could further enhance the resolution in deeper tissues.

Looking forward, an interesting application for rsOAPs could be in *in-vivo* diagnostics. This could be achieved by linking targeting signal to rsOAP and sterically shielding it with XTENylation[70] like approaches to reduce its immunogenicity and extend its plasma life.

Another, interesting concept would be to engineer functional labels (sensor) based on rsOAPs, capable of sensing and reporting nutrients such as glucose and messenger molecules such as calcium. For instance, in combination with new labels, these sensors would allow deeper visualization of cellular distributions and chemical environments in the tumor microenvironment with high spatial resolution in deep tissue. The universality of the concept will provide crucial insights for a number of questions. Like brain functioning, cell mediated immune responses or developmental pathophysiology.

Appendix

Appendix I - List of Publications

The present work is a publication-based dissertation based on two publications, published in international journals (* indicates equal author contribution):

1) Vetschera, P*., **Mishra, K***., Fuenzalida-Werner, J. P., Chmyrov, A., Ntziachristos, V. & Stiel, A. C. Characterization of Reversibly Switchable Fluorescent Proteins in Optoacoustic Imaging. Anal. Chem. 90, 10527–10535 (2018).

2) **Mishra, K**., Stankevych, M., Fuenzalida-Werner, J. P., Grassmann, S., Gujrati, V., Huang, Y., Klemm, U., Buchholz, V. R., Ntziachristos, V. & Stiel, A. C. Multiplexed whole-animal imaging with reversibly switchable optoacoustic proteins. Sci. Adv. 6, 6293–6305 (2020).

Throughout my Ph.D. work, I also contributed to the following additional publication:

1) Fuenzalida-Werner, J. P., Janowski, R., **Mishra, K**., Weidenfeld, I., Niessing, D., Ntziachristos, V. & Stiel, A. C. Crystal structure of a biliverdin-bound phycobiliprotein: Interdependence of oligomerization and chromophorylation. J. Struct. Biol. 204, 519–522 (2018).

2) **Mishra, K***., Fuenzalida-Werner*, J. P*., Ntziachristos, V. & Stiel, A. C. Photocontrollable Proteins for Optoacoustic Imaging. Anal. Chem. 91, 5470–5477 (2019).

3) Fuenzalida Werner, J. P., **Mishra, K**., Huang, Y., Vetschera, P., Glasl, S., Chmyrov, A., Richter, K., Ntziachristos, V. & Stiel, A. C. Structure-Based Mutagenesis of Phycobiliprotein smURFP for Optoacoustic Imaging. ACS Chem. Biol. 14, 1896–1903 (2019).

4) Fuenzalida Werner, J. P., Huang, Y., **Mishra, K**., Janowski, R., Vetschera, P., Heichler, C., Chmyrov, A., Neufert, C., Niessing, D., Ntziachristos, V. & Stiel, A. C. Challenging a Preconception: Optoacoustic Spectrum Differs from the Optical Absorption Spectrum of Proteins and Dyes for Molecular Imaging. Anal. Chem. 92, 10717–10724 (2020).

Appendix II - List of Figures

Figure 7: Photo- or optoacoustic (OA) imaging: **a)** General principle of OA, **b)** Relation of resolution and imaging depth for various imaging techniques including OA with the acoustic and optical resolution, **c)** Different modes of OA imaging: tomography (e.g., multispectral OA tomography; MSOT, left), scanning acoustic focus mesoscopy (e.g., raster scanning OA mesoscopy; RSOM, middle) and OA microscopy (right). FOV = field-of-view, AR = acoustic resolution and OR = optical resolution OA imaging, respectively, CFM = confocal fluorescence microscopy. Reprinted with permission from ref [26] (Copyright © 2018 American Chemical Society).

Figure 8: Light-induced chromophore conformations in reversible switchable Fluorescent Proteins (RSFPs) where **a)** shows the cartoon representation of classic RSFPs 11-strand beta barrel hosting a centrally located p- hydroxybenzylidene-imidazolinone (p-HBI), **b)** to **f)** are showing the conformation transformation for Dronpa, Padron, rsTagRFP & rsCherryRev, rsCherry and Dreiklang respectively. Colors highlighting chromophores correspond to the spectral range of observed fluorescence. Non-fluorescent chromophores are shown in gray. Adapted from the ref [33] Copyright ©2014 with permission from Elsevier.

Figure 9: a) Domain architecture of extended phytochrome family. The phytochromes essentially consist of an N-terminal photosensory core module and a C-terminal regulator output domain. The P3/GAF domain is associated with the bilin chromophore and is highly conserved. All phytochromes except those found in the Cph2 subfamily share P2/PAS domains, whereas Phys possess two additional PAS domains within the regulatory region. Fungal phytochromes (Fphs) have a domain structure similar to those of the cyanobacterial phytochrome 1 (Cph1) and bacteriophytochrome (BphP) families, except for an additional C-terminal response regulator receiver domain (RR) extension and variable N-terminal extensions, **b)** Experimental Pr and Pfr absorption spectra of *Dr*BphP-PCM, **c)** Cartoon representation for the crystal structure of *Dr*BphP-PCM in the Pr Dark state (PDB: 400P)[44] and in Pfr-Illuminated state(PDB: 4O01)[44], **d)** Light-induced BV conformation in the Pr and Pfr state of *Dr*BphP-PCM.

Figure 10: General principles of photocontrol in RSFPs and BphPs. **a)** A simplified model of RSP either in state A or state B, which can transition between a signal form and a no-signal form (e.g., fluorescence or OA). The signal form emits fluorescence and/or ultrasound (US) waves. **b)** Simplified Jablonski diagram depicting the relevant transitions between forms A and B of a reversibly switchable molecule. Fluo = fluorescence, Abs = absorption, NRD = nonradiative decay, ISC = intersystem crossing, Vibr. = vibrational relaxation. Other electronic

states can occur but are not depicted. For OA a QY_{NRD} "QY_{Fluo} is optimal (see the thickness of transition arrows in form A for example). **c)** Symbolized changes of a bulk volume of photo-controllable molecules as it would appear in a cuvette or a cell under illumination with two wavelengths. The curve depicts the exponential decay under green light illumination (green line) and subsequent recovery of the signal over time under UV illumination (purple arrowhead). A single switching curve is shown in the inset together with a stylized cuvette showing the change of photo-controllable molecules in bulk. Reprinted with permission from ref [26] (Copyright © 2018 American Chemical Society).

Figure 11: Unmixing strategies for RSP signal from background. **a-e)** the basic principle of **a)** differential, **b)** double differential, **c)** temporal unmixed, and locked-in reconstruction (LIR), **d)** Temporal multiplexing of two labels based on their characteristic photocontrol kinetics, **e)** Multiplexing based on difference spectra demixing. The structure labeled with photo-controllable protein is shown in black, blue & orange and background in red. Illumination wavelengths are shown as green and purple bars over each strategy. The graphs show simulated signal traces of the respective structure labeled with RSP. Basics calculation is depicted or indicated as VCA = vertex component analysis, for temporal unmixing and frequency space for LIR. All the images show only the starting illumination and generated signal sequence. Note that the number of repetitions determines the CNR. Reprinted with permission from ref [26] (Copyright © 2018 American Chemical Society).

Figure 12: Reversible switchable proteins (RSPs) application in OA. **a)** The longitudinal tumor development and metastasis in mouse liver using U87 cells, expressing BphP1 and differential unmixing,[30] **b)** Subcutaneous tumor together with vascular morphology in 3D using HT29 cells expressing AGP1 unmixed with the double differential strategy,[54] **c)** LIR (Multiplexed detection) of cancerous cells in the liver, the U87 cells expressing *Dr*BphP-PCM (right, red) or HEK-293 expressing cells expressing both *Dr*BphP-PCM and *Rp*BphP1 (left, blue),[58] **d)** *In-vivo* unmixing of individual bacteria expressing two RSP (sGPC2 or BphP1) and non-switchable NIR label mIFP,[56] **e)** Longitudinal imaging of PPIs in a tumor and monitoring of tumor metastases in a mouse liver using LIR unmixing strategy[58]. Arrows indicate a secondary tumor. Adapted with permission from ref[26] (Copyright © 2018 American Chemical Society).

Appendix III – Abbreviations

Abs	Absorbance
BiPC	Bimolecular Photoacoustic Complementation
Bphps	Bacteriophytochromes
BV	Billiverdin
C-Terminal	Carboxyl Terminal
Cphys	Cyanobacterial Phytochromes
CT	Computed Tomography
DMEM	Dulbecco’s Modified Eagle Medium
E.Coli	Escherichia coli
EGFP	Enhanced Green Fluorescent Protein
FKBP	FK506 Binding Protein
Flou	Fluorescence
FOV	Field of View
FP	Fluorescent Protein
Fphps	Fungal Phytochromes
FRB	FKBP-Rapamycin Binding Domain
GAF	cGMP Phosphodiesterase/Adenylate Cyclase/ Fhla
HO	Heme Oxygenase
ISC	Intersystem Crossing
IVM	Intravital Microscopy
LIR	Frequency Lock-In Reconstruction

MRI	Magnetic Resonance Imaging
MSOT	Multispectral Optoacoustic Tomography
N-Terminal	Amino Terminal
NIR	Near-Infra-Red
NRD	Non-Radiative Decay
OA	Optoacoustics
OPO	Optical Parametric Oscillator
OR	Optical Resolution
PAS	Per/Arnt/Sim
PBS	Phosphate Buffer Saline
PCB	Phycocyanobilin
PCM	Photosensory Core Module
PET	Beta-2-Microglobulin
pHBI	4-(P-Hydroxybenzylidene)-5-Imidazolinone
Phy	Phytochromes
PHY	Phytochrome-Specific
PΦB	Phytochromobilin
QY	Quantum Yield
RPMI	Roswell Park Memorial Institute Medium
rsEGFP	Reversible Switchable Green Fluorescent Proteins
RSFP	Reversible Switchable Fluorescent Proteins
rsOAPs	Reversible Switchable Optoacoustic Proteins
RSOM	Raster Scan Optoacoustic Mesoscopy
RSPs	Reversible Switchable Proteins

SD	Difference Signals
VCA	Vertex Component analysis
Vibr.	Vibrational Relaxation

Appendix IV – Bibliography

1. Ntziachristos, V. Going deeper than microscopy: the optical imaging frontier in biology. *Nat. Methods* **7**, 603–14 (2010).
2. Frangioni, J. V. New technologies for human cancer imaging. *Journal of Clinical Oncology* vol. 26 4012–4021 (2008).
3. Wang, L. V & Yao, J. A practical guide to photoacoustic tomography in the life sciences. *Nature Methods* vol. 13 627–638 (2016).
4. Laufer, J. G., Zhang, E. Z., Treeby, B. E., Cox, B. T., Beard, P. C., Johnson, P. & Pedley, B. In vivo preclinical photoacoustic imaging of tumor vasculature development and therapy. *J. Biomed. Opt.* **17**, 1 (2012).
5. Bohndiek, S. E., Sasportas, L. S., Machtaler, S., Jokerst, J. V., Hori, S. & Gambhir, S. S. Photoacoustic tomography detects early vessel regression and normalization during ovarian tumor response to the antiangiogenic therapy trebananib. *J. Nucl. Med.* **56**, 1942–1947 (2015).
6. Gujrati, V., Prakash, J., Malekzadeh-Najafabadi, J., Stiel, A., Klemm, U., Mettenleiter, G., Aichler, M., Walch, A. & Ntziachristos, V. Bioengineered bacterial vesicles as biological nano-heaters for optoacoustic imaging. *Nat. Commun.* **10**, 1114 (2019).
7. Guggenheim, J. A., Allen, T. J., Plumb, A., Zhang, E. Z., Rodriguez-Justo, M., Punwani, S. & Beard, P. C. Photoacoustic imaging of human lymph nodes with endogenous lipid and hemoglobin contrast. *J. Biomed. Opt.* **20**, 1 (2015).
8. Reber, J., Willershäuser, M., Karlas, A., Paul-Yuan, K., Diot, G., Franz, D., Fromme, T., Ovsepian, S. V, Bézière, N., Dubikovskaya, E., Karampinos, D. C., Holzapfel, C., Hauner, H., Klingenspor, M. & Ntziachristos, V. Non-invasive Measurement of Brown Fat Metabolism Based on Optoacoustic Imaging of Hemoglobin Gradients. *Cell Metab.* **27**, 689-701.e4 (2018).
9. Gujrati, V., Mishra, A. & Ntziachristos, V. Molecular imaging probes for multi-spectral optoacoustic tomography. *Chem. Commun.* **53**, 4653–4672 (2017).
10. Weber, J., Beard, P. C. & Bohndiek, S. E. Contrast agents for molecular photoacoustic imaging. *Nature Methods* vol. 13 639–650 (2016).
11. Lutzweiler, C. & Razansky, D. Optoacoustic imaging and tomography: Reconstruction approaches and outstanding challenges in image performance and quantification. *Sensors (Switzerland)* vol. 13 7345–7384 (2013).
12. Brunker, J., Yao, J., Laufer, J. & Bohndiek, S. E. Photoacoustic imaging using genetically encoded reporters: a review. *J. Biomed. Opt.* **22**, 070901 (2017).
13. Yao, J., Wang, L., Yang, J. M., Maslov, K. I., Wong, T. T. W., Li, L., Huang, C. H., Zou, J. & Wang, L. V. High-speed label-free functional photoacoustic microscopy of mouse brain in action. *Nat. Methods* **12**, 407–410 (2015).
14. Aguirre, J., Schwarz, M., Garzorz, N., Omar, M., Buehler, A., Eyerich, K. & Ntziachristos, V. Precision assessment of label-free psoriasis biomarkers with ultra-broadband optoacoustic mesoscopy. *Nat. Biomed. Eng.* **1**, 68 (2017).
15. Hai, P., Imai, T., Xu, S., Zhang, R., Aft, R. L., Zou, J. & Wang, L. V. High-throughput, label-free, single-cell photoacoustic microscopy of intratumoral metabolic heterogeneity. *Nat. Biomed. Eng.* **3**, 381–391 (2019).

16. Herzog, E., Taruttis, A., Beziere, N., Lutich, A. A. & Razansky, D. Optical imaging of cancer heterogeneity with Multispectral. *Radiology* **263**, 461–468 (2012).
17. Kircher, M. F., De La Zerda, A., Jokerst, J. V, Zavaleta, C. L., Kempen, P. J., Mittra, E., Pitter, K., Huang, R., Campos, C., Habte, F., Sinclair, R., Brennan, C. W. & Gambhir, S. S. A Brain Tumor Molecular Imaging Strategy Using A New Triple-Modality MRI-Photoacoustic-Raman Nanoparticle HHS Public Access. *Nat Med* **18**, 829–834.
18. De La Zerda, A., Zavaleta, C., Keren, S., Vaithilingam, S., Bodapati, S., Liu, Z., Levi, J., Smith, B. R., Ma, T. J., Oralkan, O., Cheng, Z., Chen, X., Dai, H., Khuri-Yakub, B. T. & Gambhir, S. S. Carbon nanotubes as photoacoustic molecular imaging agents in living mice. *Nat. Nanotechnol.* **3**, 557–562 (2008).
19. Cai, X., Li, L., Krumholz, A., Guo, Z., Erpelding, T. N., Zhang, C., Zhang, Y., Xia, Y. & Wang, L. V. Multi-scale molecular photoacoustic tomography of gene expression. *PLoS One* **7**, (2012).
20. Stritzker, J., Kirscher, L., Scadeng, M., Deliolanis, N. C., Morscher, S., Symvoulidis, P., Schaefer, K., Zhang, Q., Buckel, L., Hess, M., Donat, U., Bradley, W. G., Ntziachristos, V. & Szalay, A. A. Vaccinia virus-mediated melanin production allows MR and optoacoustic deep tissue imaging and laser-induced thermotherapy of cancer. *Proc. Natl. Acad. Sci. U. S. A.* **110**, 3316–3320 (2013).
21. Jiang, Y., Sigmund, F., Reber, J., Deán-Ben, X. L., Glasl, S., Kneipp, M., Estrada, H., Razansky, D., Ntziachristos, V. & Westmeyer, G. G. Violacein as a genetically-controlled, enzymatically amplified and photobleaching-resistant chromophore for optoacoustic bacterial imaging. *Sci. Rep.* **5**, 11048 (2015).
22. Razansky, D., Distel, M., Vinegoni, C., Ma, R., Perrimon, N., Köster, R. W. & Ntziachristos, V. Multispectral opto-acoustic tomography of deep-seated fluorescent proteins in vivo. *Nat. Photonics* **3**, 412–417 (2009).
23. Sigmund, F., Massner, C., Erdmann, P., Stelzl, A., Rolbieski, H., Desai, M., Bricault, S., Wörner, T. P., Snijder, J., Geerlof, A., Fuchs, H., De Angelis, M. H., Heck, A. J. R., Jasanoff, A., Ntziachristos, V., Plitzko, J. & Westmeyer, G. G. Bacterial encapsulins as orthogonal compartments for mammalian cell engineering. *Nat. Commun.* **9**, 1–14 (2018).
24. Krumholz, A., Shcherbakova, D. M., Xia, J., Wang, L. V. & Verkhusha, V. V. Multicontrast photoacoustic in vivo imaging using near-infrared fluorescent proteins. *Sci. Rep.* **4**, 1–7 (2014).
25. Stiel, A. C., Luís Deán-Ben, + X, Jiang, Y., Ntziachristos, V., Razansky, D. & Westmeyer, G. G. High contrast imaging of reversibly switchable fluorescent proteins via temporally unmixed Multispectral Optoacoustic Tomography (tuMSOT). *Opt. Lett.* **40**, 4691–4694 (2015).
26. Mishra, K., Fuenzalida-Werner, J. P., Ntziachristos, V. & Stiel, A. C. Photocontrollable Proteins for Optoacoustic Imaging. *Anal. Chem.* **91**, 5470–5477 (2019).
27. Zhou, X. X. & Lin, M. Z. Photoswitchable Fluorescent Proteins: Ten Years of Colorful Chemistry and Exciting Applications. *Curr Opin Chem Biol* **17**, 682–690 (2013).
28. Adam, V., Berardozzi, R., Byrdin, M. & Bourgeois, D. Phototransformable fluorescent proteins: Future challenges. *Current Opinion in Chemical Biology* vol. 20 92–102 (2014).

29. Grotjohann, T., Testa, I., Leutenegger, M., Bock, H., Urban, N. T., Lavoie-Cardinal, F., Willig, K. I., Eggeling, C., Jakobs, S. & Hell, S. W. Diffraction-unlimited all-optical imaging and writing with a photochromic GFP. *Nature* **478**, 204–208 (2011).
30. Ando, R., Mizuno, H. & Miyawaki, A. Regulated fast nucleocytoplasmic shuttling observed by reversible protein highlighting. *Science (80-.).* **306**, 1370–1373 (2004).
31. Fankhauser, C. The Phytochromes, a Family of Red/Far-red Absorbing Photoreceptors. *Journal of Biological Chemistry* vol. 276 11453–11456 (2001).
32. Lukyanov, K. a, Fradkov, A. F., Gurskaya, N. G., Matz, M. V, Labas, Y. a, Savitsky, A. P., Markelov, M. L., Zaraisky, A. G., Zhao, X., Fang, Y., Tan, W. & Lukyanov, S. a. Natural animal coloration can be determined by a nonfluorescent green fluorescent protein homolog. *J. Biol. Chem.* **275**, 25879–25882 (2000).
33. Shcherbakova, D. M. & Verkhusha, V. V. Chromophore chemistry of fluorescent proteins controlled by light. *Current Opinion in Chemical Biology* vol. 20 60–68 (2014).
34. Brakemann, T., Stiel, A. C., Weber, G., Andresen, M., Testa, I., Grotjohann, T., Leutenegger, M., Plessmann, U., Urlaub, H., Eggeling, C., Wahl, M. C., Hell, S. W. & Jakobs, S. A reversibly photoswitchable GFP-like protein with fluorescence excitation decoupled from switching. *Nat. Biotechnol.* **29**, 942–950 (2011).
35. Stiel, A. C., Trowitzsch, S., Weber, G., Andresen, M., Eggeling, C., Hell, S. W., Jakobs, S. & Wahl, M. C. .8 Å bright-state structure of the reversibly switchable fluorescent protein Dronpa guides the generation of fast switching variants. *Biochem. J* **402**, 35–42 (2007).
36. Mizuno, H., Mal, T. K., Wälchli, M., Kikuchi, A., Fukano, T., Ando, R., Jeyakanthan, J., Taka, J., Shiro, Y., Ikura, M. & Miyawaki, A. Light-dependent regulation of structural flexibility in a photochromic fluorescent protein. *Proc. Natl. Acad. Sci. U. S. A.* **105**, 9227–9232 (2008).
37. Andresen, M., Stiel, A. C., Fölling, J., Wenzel, D., Schönle, A., Egner, A., Eggeling, C., Hell, S. W. & Jakobs, S. Photoswitchable fluorescent proteins enable monochromatic multilabel imaging and dual color fluorescence nanoscopy. *Nat. Biotechnol.* **26**, (2008).
38. Nathan C. Rockwell, Y.-S. S. & and J. Clark Lagarias. Phytochrome Structure and Signaling Mechanisms. *Annu. Rev. Plant Biol.* **57**, 837–58 (2006).
39. Rottwinkel, G., Oberpichler, I. & Lamparter, T. Bathy phytochromes in rhizobial soil bacteria. *J. Bacteriol.* **192**, 5124–5133 (2010).
40. Nathan C. Rockwell, Shelley S. Martin, Kateryna Feoktistova, and J. C. L. Diverse two-cysteine photocycles in phytochromes and cyanobacteriochromes. *PNAS* **108**, 11854–11859 (2011).
41. Wagner, J. R., Brunzelle, J. S., Forest, K. T. & Vierstra, R. D. A light-sensing knot revealed by the structure of the chromophore-binding domain of phytochrome. *Nature* **438**, 325–331 (2005).
42. Kohchi, T., Kataoka, H. & Linley, P. J. Biosynthesis of chromophores for phytochrome and related photoreceptors. *Plant Biotechnology* vol. 22 409–413 (2005).
43. Duanmu, D., Bachy, C., Sudek, S., Wong, C. H., Jiménez, V., Rockwell, N. C., Martin, S. S., Ngan, C. Y., Reistetter, E. N., Van Baren, M. J., Price, D. C., Wei, C. L., Reyes-

Prieto, A., Lagarias, J. C. & Worden, A. Z. Marine algae and land plants share conserved phytochrome signaling systems. *Proc. Natl. Acad. Sci. U. S. A.* **111**, 15827–15832 (2014).

44. Takala, H., Björling, A., Berntsson, O., Lehtivuori, H., Niebling, S., Hoernke, M., Kosheleva, I., Henning, R., Menzel, A., Ihalainen, J. A. & Westenhoff, S. Signal amplification and transduction in phytochrome photosensors. *Nature* **509**, 245–248 (2014).
45. Hoelen, C. G. A., de Mul, F. F. M., Pongers, R. & Dekker, A. Three-dimensional photoacoustic imaging of blood vessels in tissue. *Opt. Lett.* **23**, 648 (1998).
46. Hoelen, C. G. A. & de Mul, F. F. M. Image reconstruction for photoacoustic scanning of tissue structures. *Appl. Opt.* **39**, 5872 (2000).
47. Xu, Y. & Wang, L. V. Time Reversal and Its Application to Tomography with Diffracting Sources. *Phys. Rev. Lett.* **92**, 4 (2004).
48. Wang, K., Ermilov, S. A., Su, R., Brecht, H. P., Oraevsky, A. A. & Anastasio, M. A. An imaging model incorporating ultrasonic transducer properties for three-dimensional optoacoustic tomography. *IEEE Trans. Med. Imaging* **30**, 203–214 (2011).
49. Rosenthal, A., Ntziachristos, V. & Razansky, D. Model-based optoacoustic inversion with arbitrary-shape detectors. *Med. Phys.* **38**, 4285–4295 (2011).
50. Taruttis, A. & Ntziachristos, V. Advances in real-time multispectral optoacoustic imaging and its applications. *Nat. Photonics* **9**, 219–227 (2015).
51. Tzoumas, S. & Ntziachristos, V. Spectral unmixing techniques for optoacoustic imaging of tissue pathophysiology. *Philosophical Transactions of the Royal Society A: Mathematical, Physical and Engineering Sciences* vol. 375 20170262 (2017).
52. Yao, J., Kaberniuk, A. A., Li, L., Shcherbakova, D. M., Zhang, R., Wang, L., Li, G., Verkhusha, V. V & Wang, L. V. Multi-scale photoacoustic tomography using reversibly switchable bacterial phytochrome as a near-infrared photochromic probe. *Nat. Methods* **13**, 67–73 (2016).
53. Dortay, H., Märk, J., Wagener, A., Zhang, E., Grötzinger, C., Hildebrandt, P., Friedrich, T. & Laufer, J. Dual-wavelength photoacoustic imaging of a photoswitchable reporter protein. in (eds. Oraevsky, A. A. & Wang, L. V.) vol. 9708 970820 (International Society for Optics and Photonics, 2016).
54. Märk, J., Dortay, H., Wagener, A., Zhang, E., Buchmann, J., Grötzinger, C., Friedrich, T. & Laufer, J. Dual-wavelength 3D photoacoustic imaging of mammalian cells using a photoswitchable phytochrome reporter protein. *Commun. Phys.* **1**, 3 (2018).
55. Li, L., Shemetov, A. A., Baloban, M., Hu, P., Zhu, L., Shcherbakova, D. M., Zhang, R., Shi, J., Yao, J., Wang, L. V. & Verkhusha, V. V. Small near-infrared photochromic protein for photoacoustic multi-contrast imaging and detection of protein interactions in vivo. *Nat. Commun.* **9**, 1–14 (2018).
56. Chee, R. K. W., Li, Y., Zhang, W. & Campbell, R. E. In vivo photoacoustic difference-spectra imaging of bacteria using photoswitchable chromoproteins. *J. Biomed. Opt.* **23**, 1 (2018).
57. Yao, J., Kaberniuk, A. A., Li, L., Shcherbakova, D. M., Zhang, R., Wang, L., Li, G., Verkhusha, V. V & Wang, L. V. Multiscale photoacoustic tomography using reversibly switchable bacterial phytochrome as a near-infrared photochromic probe. *Nat.*

Methods **13**, 67–73 (2015).

58. Li, L., Shemetov, A. A., Baloban, M., Hu, P., Zhu, L., Shcherbakova, D. M., Zhang, R., Shi, J., Yao, J., Wang, L. V. & Verkhusha, V. V. Small near-infrared photochromic protein for photoacoustic multi-contrast imaging and detection of protein interactions in vivo. *Nat. Commun.* **9**, 2734 (2018).
59. Oraevsky, A. A., Jacques, S. L. & Tittel, F. K. Measurement of tissue optical properties by time-resolved detection of laser-induced transient stress. *Appl. Opt.* **36**, 402–15 (1997).
60. Vetschera, P., Mishra, kanuj, Fuenzalida Werner, J.-P., Chmyrov, A., Ntziachristos, V. & Stiel, A. C. Characterization of reversibly switchable fluorescent proteins (rsFPs) in optoacoustic imaging. *Anal. Chem.* (2018) doi:10.1021/acs.analchem.8b02599.
61. Mishra, K., Stankevych, M., Fuenzalida-Werner, J. P., Grassmann, S., Gujrati, V., Huang, Y., Klemm, U., Buchholz, V. R., Ntziachristos, V. & Stiel, A. C. Multiplexed whole-animal imaging with reversibly switchable optoacoustic proteins. *Sci. Adv.* **6**, 6293–6305 (2020).
62. Vetschera, P., Mishra, K., Fuenzalida-Werner, J. P., Chmyrov, A., Ntziachristos, V. & Stiel, A. C. Characterization of Reversibly Switchable Fluorescent Proteins in Optoacoustic Imaging. *Anal. Chem.* **90**, 10527–10535 (2018).
63. Ntziachristos, V. & Razansky, D. Molecular imaging by means of multispectral optoacoustic tomography (MSOT). *Chem. Rev.* **110**, 2783–2794 (2010).
64. Wang, L. V. & Hu, S. Photoacoustic tomography: In vivo imaging from organelles to organs. *Science* vol. 335 1458–1462 (2012).
65. Wang, D., Wu, Y. & Xia, J. Review on photoacoustic imaging of the brain using nanoprobes. *Neurophotonics* **3**, 010901 (2016).
66. Jokerst, J. V, Cole, A. J., Van De Sompel, D. & Gambhir, S. S. Gold nanorods for ovarian cancer detection with photoacoustic imaging and resection guidance via Raman imaging in living mice. *ACS Nano* **6**, 10366–10377 (2012).
67. Beziere, N., Lozano, N., Nunes, A., Salichs, J., Queiros, D., Kostarelos, K. & Ntziachristos, V. Dynamic imaging of PEGylated indocyanine green (ICG) liposomes within the tumor microenvironment using multi-spectral optoacoustic tomography (MSOT). *Biomaterials* **37**, 415–424 (2015).
68. Qin, H., Zhou, T., Yang, S., Chen, Q. & Xing, D. Gadolinium(III)-gold nanorods for MRI and photoacoustic imaging dual-modality detection of macrophages in atherosclerotic inflammation. *Nanomedicine* **8**, 1611–1624 (2013).
69. Jokerst, J. V, Thangaraj, M., Kempen, P. J., Sinclair, R. & Gambhir, S. S. Photoacoustic imaging of mesenchymal stem cells in living mice via silica-coated gold nanorods. *ACS Nano* **6**, 5920–5930 (2012).
70. Schellenberger, V., Wang, C. W., Geething, N. C., Spink, B. J., Campbell, A., To, W., Scholle, M. D., Yin, Y., Yao, Y., Bogin, O., Cleland, J. L., Silverman, J. & Stemmer, W. P. C. A recombinant polypeptide extends the in vivo half-life of peptides and proteins in a tunable manner. *Nat. Biotechnol.* **27**, 1186–1190 (2009).

Appendix V – Publication 1

analytical chemistry
Article
Cite This: Anal. Chem. 2018, 90, 10527−10535
pubs.acs.org/ac

Characterization of Reversibly Switchable Fluorescent Proteins in Optoacoustic Imaging

Paul Vetschera,[†,‡] Kanuj Mishra,[†] Juan Pablo Fuenzalida-Werner,[†] Andriy Chmyrov,[†,§] Vasilis Ntziachristos,[†,‡,§] and Andre C. Stiel*,[†]

[†]Institute of Biological and Medical Imaging, Helmholtz Zentrum München, D-85764 Neuherberg, Germany
[‡]Chair of Biological Imaging, Technische Universität München, D-80333 München, Germany
[§]Center for Translational Cancer Research, Technische Universität München, D-81675 München, Germany

Supporting Information

ABSTRACT: Reversibly switchable fluorescent proteins (rsFPs) have had a revolutionizing effect on life science imaging due to their contribution to sub-diffraction-resolution optical microscopy (nanoscopy). Initial studies showed that their use as labels could also be highly beneficial for emerging photo- or optoacoustic imaging. It could be shown that their use in optoacoustics (i) strongly improves the imaging contrast-to-noise ratio due to modulation and locked-in detection, (ii) facilitates fluence calibration, affording precise measurements of physiological parameters, and finally (iii) could boost spatial resolution following similar concepts as used for nanoscopy. However, rsFPs show different photophysical behavior in optoacoustics than in optical microscopy because optoacoustics requires pulsed illumination and depends on signal generation via nonradiative energy decay channels. This implies that rsFPs optimized for fluorescence imaging may not be ideal for optoacoustics. Here, we analyze the photophysical behavior of a broad range of rsFPs with optoacoustics and analyze how the experimental factors central to optoacoustic imaging influence the different types of rsFPs. Finally, we discuss how knowledge of the switching behavior can be exploited for various optoacoustic imaging approaches using sophisticated temporal unmixing schemes.

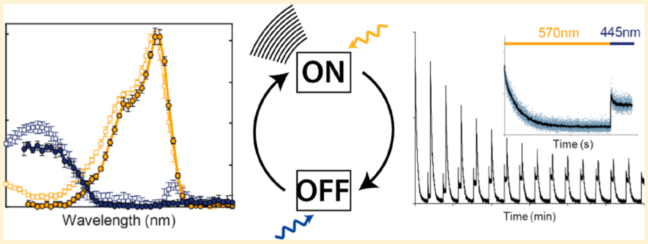

Reversibly switchable fluorescent proteins (rsFPs) are a class of mostly green fluorescent protein (GFP)-like transgene imaging labels that can be selectively and reversibly switched between metastable states with distinct photophysical characteristics by light of appropriate different wavelengths (for review, see ref 1). The on/off switching of fluorescence possible with rsFPs revolutionized optical imaging, due to its importance for sub-diffraction-resolution microscopy concepts (nanoscopy).[2,3] Structural studies as well as photophysical analysis allowed for tailored improvements of rsFPs for nanoscopy (for overviews, see refs 4−6).

Photo- or optoacoustic (OA) imaging is an innovative imaging approach that overcomes the penetration depth limit of optical imaging methods by acoustically detecting light absorption.[7−9] In contrast to light, ultrasound waves are only weakly scattered in tissue; thus the resolution of optoacoustic images is limited only by ultrasound diffraction, not photon diffusion. The contrast in optoacoustic imaging is based on the different absorption coefficients of tissue components like blood, melanin, and lipids or suitable transgene labels in the sample. Those absorbers can be separated by multiwavelength illumination and subsequent unmixing algorithms.[10] The method allows high-resolution imaging of tissue to depths of several centimeters[11,12] and has already proved effective at imaging brain activity,[13,14] precise cancer localization,[15,16] and cell fate and migration of macrophages[17] or stem cells.[18] However, longitudinal, noninvasive studies of live animals, one of the unique capabilities of optoacoustic imaging, are limited by the low number of transgene labels for optoacoustic and their poor signal generation efficiency, which complicates imaging of specific processes at the cellular and subcellular levels.[19] The relatively weak optoacoustic signals generated by illuminating transgene labels at single wavelengths results in weak contrast compared to other strong absorbers like hemoglobin or melanin.

Recently, a method was described for harnessing the unique properties of rsFPs as transgene labels in optoacoustic imaging: Light-driven modulation of the rsFPs, together with lock-in detection of the optoacoustic signals, could strongly improve the contrast-to-noise ratio (CNR), especially over the background of abundant endogenous absorbers like hemoglobin.[20−22] Moreover, this approach also allows temporal unmixing of different labels and therefore multiplexing with only two wavelengths.[21] Additionally, recent studies could show that the characteristic light-intensity-dependent switching kinetics of rsFPs can be used to calibrate light fluence, which can improve the accuracy of, for example, blood-oxygenation

Received: June 8, 2018
Accepted: August 6, 2018
Published: August 6, 2018

DOI: 10.1021/acs.analchem.8b02599
Anal. Chem. 2018, 90, 10527−10535

measurements with optoacoustics;[23] or metastable rsFPs can be used to selectively mark cell populations, as demonstrated for photoconvertible proteins.[24] Finally, imaging schemes similar to nanoscopy can improve the spatial resolution.[20] However, these studies already suggested that the different illumination (pulsed) and detection (ultrasound) leads to a different behavior of rsFPs in optoacoustic compared to fluorescence imaging. This implies that rsFPs optimized for fluorescence imaging may not be ideal for optoacoustics, and it highlights the need for systematic analysis of rsFPs in the optoacoustic modality in order to provide a baseline for further protein engineering efforts to enhance their performance.

Switching in rsFPs relies on the light-driven transition between distinct states that differ in chromophore planarity, stability, and protonation. These factors determine the absorption and fluorescence spectra of each switched state (exemplified for Dronpa).[25,26] Two major types can be distinguished (Figure 1): photochromic rsFPs, which show a change in absorption spectra upon switching (photochromes), and rsFPs that exhibit a quantum yield (QY) change but largely preserve the absorption spectra (QY changer). Presently, the majority of rsFPs stem from the class of GFP-like fluorescent proteins, showing absorption in the green, yellow, and red regions of the spectrum.[4] Recently, the class of bacteriophytochromes harboring a porphyrin chromophore have found attention as labels in the near-infrared (NIR).[27] Members of this class are reversibly switchable, similar to classic photochromic rsFPs, but they have not been largely exploited for imaging.[20,22] Like any other chromophores, rsFPs show a number of possible deexcitation pathways from their excited state. Predominant are the fast processes of internal conversion (picosecond scale) and fluorescence (nanosecond scale) as well as processes associated with the eponymous switching, like cis/trans isomerization and/or photoinduced protonation/deprotonation[28] (millisecond scale for Dronpa-like compounds).[29] Intersystem crossing and subsequent triplet deexcitation by quenching, phosphorescence, or radiationless decay (microsecond to second scale for Dronpa-like compounds)[26] have often only a smaller contribution for GFP-like proteins,[30] although a connection with switching, especially photoconversion, is discussed.[28,31]

This is especially true for the pulsed illumination used in our study, with nanosecond pulse length and <100 Hz repetition rates. The major contributor to the observable optoacoustic signal is the relaxation from the S1 by internal-conversion occurring on the picosecond time scale. Other events that can dissipate heat happen on a longer time scale ($\gg 1\ \mu$s) and would produce signals that have only neglectable contributions in the bandwidth of our transducer. All these processes are competitive to internal conversion; thus, although we cannot directly measure them, the various alternative deexcitation pathways impact the observable PGE. Moreover, this value is influenced not only by direct photophysics but also by the immediate protein's surroundings, especially the shielding β-barrel of FPs enclosing the chromophore, which can create a microenvironment with different thermoelastic parameters than the bulk solvent.[32] However, all these parameters are convoluted in the observable PGE and thus allow for a comparative study.

Presently, a broad range of rsFPs have been used for fluorescence imaging, but only a few rsFPs have been used for optoacoustic applications. In this work we systematically analyze the characteristics of rsFPs in terms of optoacoustic signal generation, switching kinetics, and applicability for optoacoustic imaging. Additionally, we elucidate the differences that optoacoustic imaging imposes on the switching behavior of those proteins and provide a conceptual framework to predict rsFP characteristics in optoacoustic imaging. Although far-red rsFPs may be most promising for deep-tissue optoacoustic imaging, we analyzed a broad range of rsFPs differing substantially in absorbance spectra, switching directionality, and switching time scales in order to provide a more comprehensive understanding of how experimental conditions affect the photophysics of these promising labels in optoacoustic imaging. Our goal is to provide a rational basis for developing rsFPs specifically for optoacoustic imaging, rather than co-opting labels previously optimized for fluorescence imaging.

■ EXPERIMENTAL SECTION

Cloning. Reversibly switchable fluorescent proteins were a kind gift from Professor Stefan Jakobs (Max Planck Institute for Biophysical Chemistry and University of Göttingen, Germany) or were synthesized as gene strings (GeneArt, LifeTechnologies, Regensburg, Germany). The coding sequences of rsFPs Dronpa, DronpaM159T, rsFastlime, Padron, rsCherry, rsCherryRev, rsCherryRev1.4, and rsTagRFP were subcloned by use of *Xho*I/*Hin*dIII into an arabinose-inducible pBad-HisA vector, while BphP1 was subcloned into the second multiple cloning site of pET-Duet1 by use of restriction sites *Nde*I/*Xho*I. Additionally, for biliverdin synthesis for BphP1, the heme oxygenase of *Nostoc* sp. was cloned by use of *Nco*I/*Hin*dIII into the first multiple cloning side of pET-Duet1.

Protein Expression and Purification. Proteins have been expressed in *Escherichia coli* strains Top10 and BL21 via standard protocols. After cell lysis, all proteins were purified by immobilized metal affinity chromatography (IMAC), followed by desalting on a Sephadex G-25 resin HiPrep 26/10 column (GE Life Sciences, Freiburg, Germany).

Optoacoustic Measurements. Before measurement, proteins were diluted to similar Q-band optical densities in the equilibrium state. Purified rsFPs were characterized with a custom-made experimental setup shown in Figure S1. Nanosecond excitation pulses were generated by an optical parametric oscillator (OPO) laser (Spitlight-DPSS 250 ZHG-OPO, InnoLas) running at a repetition rate of 50 Hz (raw laser intensities vs wavelength can be found in Figure S2). Constant pulse energy was ensured by use of a half-wave plate in a motorized rotation stage (PRM1Z8, Thorlabs) and a polarizing beam splitter; using a lookup table and adapting the polarization with the half-wave plate, we kept the power constant at ~1.3 mJ over the whole illumination spectrum. A motorized filter wheel with a low-pass and a high-pass filter at 700 nm was used to remove the near-infrared and visible fractions in the laser pulses generated by the OPO. Samples were injected into an acoustically coupled flow chip (μ-Slide I 0.2 Luer, hydrophobic, uncoated, IBIDI) and illuminated from one side by use of a fiber bundle (CeramOptec) at a constant pulse energy of ~1.3 mJ at the fiber output. Optoacoustic signals were detected with a cylindrically focused single-element transducer (V382-SU, 3.5 MHz, Olympus) and averaged over 10 laser pulses to improve the signal-to-noise ratio (SNR). A second flow chip in the light path with a low concentration of India ink was used for the generation of reference signals to correct for any deviation in the measurement approach. Briefly, before plotting of the OA

DOI: 10.1021/acs.analchem.8b02599
Anal. Chem. 2018, 90, 10527−10535

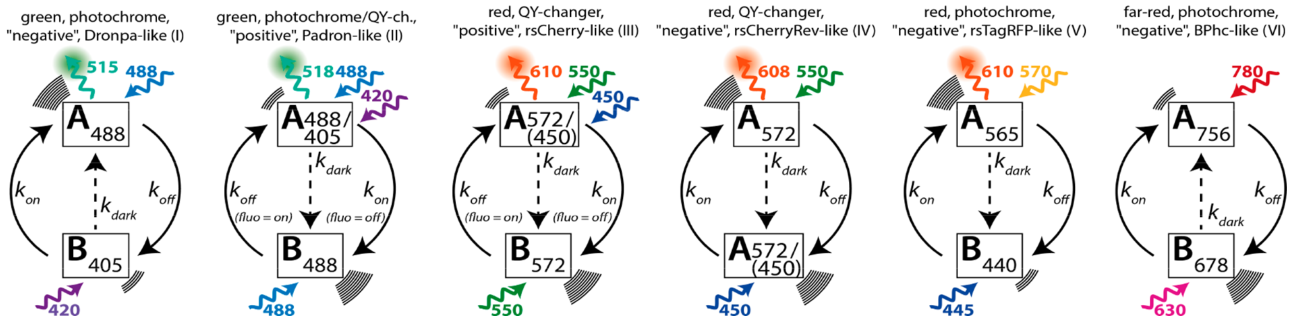

Figure 1. Switching schemes of the studied rsFPs. Light excitation and emission are denoted with a wavy arrow labeled with the corresponding wavelength. For fluorescence emission, the average wavelength of all proteins in this group is given. Emission of ultrasound is indicated by curved lines, with the number of lines indicating relative strength of emission. Switching states A and B are given with the respective wavelength of their excitation maxima; for rsFP classes with several members, the most common laser wavelength in this spectral range was selected. State transitions are denoted with solid arrows for light-driven transitions and dashed arrows for dark-state relaxation. Note that, in the second and third panels, the classic switching directions in fluorescence imaging are reversed in optoacoustics.

spectrum and calculation of the average OA value of each wavelength, the 10 OA peak-to-peak signals of the sample at each wavelength are divided by the 10 normalized ink reference peak-to-peak signals of their respective time transients. We confirmed the linearity and stability of the optoacoustic signal generated by India ink in the range of fluences used in our experiments and compared it to other well-established optoacoustic reference compounds[33] (Figure S3). The optoacoustic signals were amplified by 60 dB via a wide-band voltage amplifier (DHPVA-100, Femto) and digitized at 100 MS/s with a data acquisition card (RZE-002 400, GaGe). Exemplary wave functions of our optoacoustic signal can be found in Figure S4. The waveform is virtually identical, so no other heat-realizing processes take place on the time scale of our transducer detection.[34,35] We further show this data in frequency space (Figure S5), which shows the same result with major contributions from frequencies around 0.3 MHz. Moreover, when the loss of energy via fluorescence decay is considered, none of our proteins shows an acoustic signal generation significantly higher than our standard (which shows maximal thermal conversion),[36,37] so most likely no photochemical reaction producing a volume contribution is taking place.[34,35]

Absorption spectra were recorded after each excitation wavelength by fast interruption of the laser pulse illumination with an electronic shutter (SHB1, Thorlabs) and opening the shutter of a fiber-coupled broadband white-light illumination lamp (DH-2000, Ocean Optics). Triggering for both shutters was provided by microcontroller (Arduino Uno). Detection of the transmission spectra was provided by a commercial UV–vis spectrometer (USB 4000, Ocean Optics). The setup has a time delay for the absorption measurement of at least 110 ms after the laser pulses due to shutter responses. Both the illumination and the detection fiber were attached to a collimator rotated by 45° to the optoacoustic illumination-detection axis. Each absorption transmission spectrum was averaged over 20 acquisitions. For the optoacoustic spectral measurements, 10 optoacoustic time transients at each wavelength at 5 nm steps were recorded. To correct for laser pulse energy deviations, the peak-to-peak values at each wavelength were divided by the normalized peak-to-peak signals generated by the reference microfluidic chip, which were clearly separated in time from the sample signals. The noise level was corrected by shifting the minimum of the uncorrected optoacoustic spectrum to zero. Shifts between visible and infrared spectral measurements for BphP1 have been corrected by use of copper sulfate.[38] For absorption measurements, the measured transmission spectra were divided by the spectrum of a reference microfluidic chip filled with phosphate-buffered saline (PBS) and then subtracted from a ones vector to obtain the relative absorption. Consequently, absorption spectra were averaged over 5 nm to visualize the same spectral resolution as for the optoacoustic spectra. Baseline shifts due to light fluence deviations introduced by the white-light lamp were corrected by shifting the baseline to zero. On-state spectra were consequently normalized and the respective peaks were visually matched to the corresponding optoacoustic spectrum. Off-state spectra were equally normalized and subsequently matched to on/off peak ratio of the averaged non-normalized absorption raw data.

Figure 1 and Figure S8 show two different features of the recorded absorbance spectra. In Figure 1, the whole wavelength range of the spectrum after multiple averaging at the onset of the switching cycle is presented. In Figure S8, fractions of the absorbance spectrum after laser illumination of the corresponding wavelength are averaged over 5 nm (e.g., 497.5–502.5 nm after 500 nm illumination) and subsequently concatenated to the full spectrum.

Switching cycles were recorded by the optoacoustic peak-to-peak values as a function of laser pulses. Cycle plots in Figure 2 are averaged over 20 consecutive pulses. The excitation wavelengths chosen for switching were selected as close as possible to the absorption peak maxima. For BphP1, 630 and 780 nm were chosen to avoid the overlapping wavelength range of the two states.

Overall temperature stability in the sample chamber was ensured by monitoring the peak-to-peak distances of the optoacoustic measurement, which are indicative of the speed-of-sound and hence the temperature of the sample (Figure S6B). Moreover, we used a thermo-camera with 0.05 °C sensitivity (FLIR E60, FLIR Systems GmbH) to monitor the overall temperature in the water bath used for coupling (Figure S6C).

Pulsed versus Continuous Bleaching Experiments. Bleaching experiments were performed by use of a laser diode at 450 nm with a custom-build laser diode driver described in ref 39. The diode was triggered by a commercial waveform generator (Rigol) with rectangular pulses with pulse duration/repetition rates of 10 ns/50 MHz, 100 ns/5 MHz, and 1000 ns/500 kHz. Continuous-wave (CW) illumination was

DOI: 10.1021/acs.analchem.8b02599
Anal. Chem. 2018, 90, 10527−10535

Table 1. Overview of Photophysical Parameters of rsFPs Covered in This Study

	maxima (nm)						continuous illumination[a]			pulsed illumination[b]	OA switching dynamic range		PGE relative to $CuSO_4$[c]	
rsFP	abs	em	QY[d]	molar abs coeff ($M^{-1}\cdot cm^{-1}$)	switching mode	equil state fluores cence (%)	$t_{1/2}^{\mathrm{on}}$ [c,e] (s)	$t_{1/2}^{\mathrm{off}}$ [c,f] (s)	$t_{1/2}^{\mathrm{dark}}$ [g] (s)	$t_{1/2}^{\mathrm{off}}$ [f] (s)	switch off	bleaching $t_{1/2}$ (min)	in equilibrium state	in switched state
Dronpa[h]	503, 390[h]	518[h]	0.85[h], 0.67[i]	95 000[h]	neg	100[j]	0.1[k], 0.12[j] (405)	263[k], 115[j] (488)	50 400[k]	19.78	0.57	nd[l]	0.03 (485)	nd
rsFastLime[k]	496[k], ~390[m]	518[k]	0.77[k], 0.60[j]	39 094[k], 46 000[j]	neg	93[j]	0.11[k], 0.03[j] (405)	5[k], 2.6[j] (488)	480[k]	5.81	0.68	29	0.06 (485)	nd
Dronpa-M159T[k], Dronpa-2[n]	489[k], ~390	515[k]	0.23[k], 0.33[n], 0.28[i]	61 732[k], 56 000[i]	neg	~100	0.05[k] (405)	0.23[k] (488)	30[k]	0.64	0.89	55	0.68 (485)	nd
Padron[j]	503, 396[j]	522[j]	0.64[j]	43 000[j]	pos	5[j]	5.6[j] (488)	0.06[j] (405)	9000[j]	4.99	0.61	36	0.62 (500)	0.49 (510)
rsEGFP2[o]	478, 408[o]	503[o]	0.3[o]	61 300[o]	neg	~100	nda[p]	0.0005[o] (488)	nda	1.78	0.88	17	0.46 (485)	nd
rsCherry[q]	572[q], ~405	610[q]	0.02[r]	80 000[r]	pos	32[q]	3[q] (550)	0.05[q] (450)	40[q]	16.49	0.28	64	0.74 (570)	0.69 (570)
rsCherryRev[q]	572[q], ~405	608[q]	0.0051[r]	42 300[r], 84 000[i]	neg	8[q]	0.05[q] (450)	0.7[q] (550)	13[q]	nd	nd	nd	0.47 (570)	nd
rsCherryRev1.4[s]	572, 450[s]	609[s]	nda	nda	neg	~8	nda	nda	nda	nd	nd	nd	0.46 (570)	nd
rsTagRFP[t]	565, 440[t]	585[t]	0.11[t]	36 800[t]	neg	33[t]	0.0028[t] (440)	0.18[t] (570)	~3300[t]	14.16	0.91	25	0.45 (570)	nd
BphP1[u]	756, 678[u]	na[u]	na[u]	78 300[u]	neg	na[u]	nda	nda	nda	0.65	0.9	>200	0.31 (755)	0.53 (685)

[a] For fluorescence excitation. Note that only values from one source are intercomparable. [b] 1.3 mJ/pulse, 7 ns pulse length, 50 Hz repetiton rate. [c] Wavelength for switching or photoacoustic generation efficiency (PGE) determination, in nanometers, is given in parentheses. [d] Quantum yield. [e] Switch-on halftime. [f] Switch-off halftime . [g] Dark relaxation halftime. [h] Reference 40. [i] Reference 4. [j] Reference 42. [k] Reference 56. [l] nd, data not defined in this study. [m] ~ indicates approximations made by the authors. [n] Reference 41. [o] Reference 43. [p] nda, no data available in the literature. [q] Reference 44. [r] Reference 57. [s] Reference 45. [t] Reference 46. [u] Reference 20.

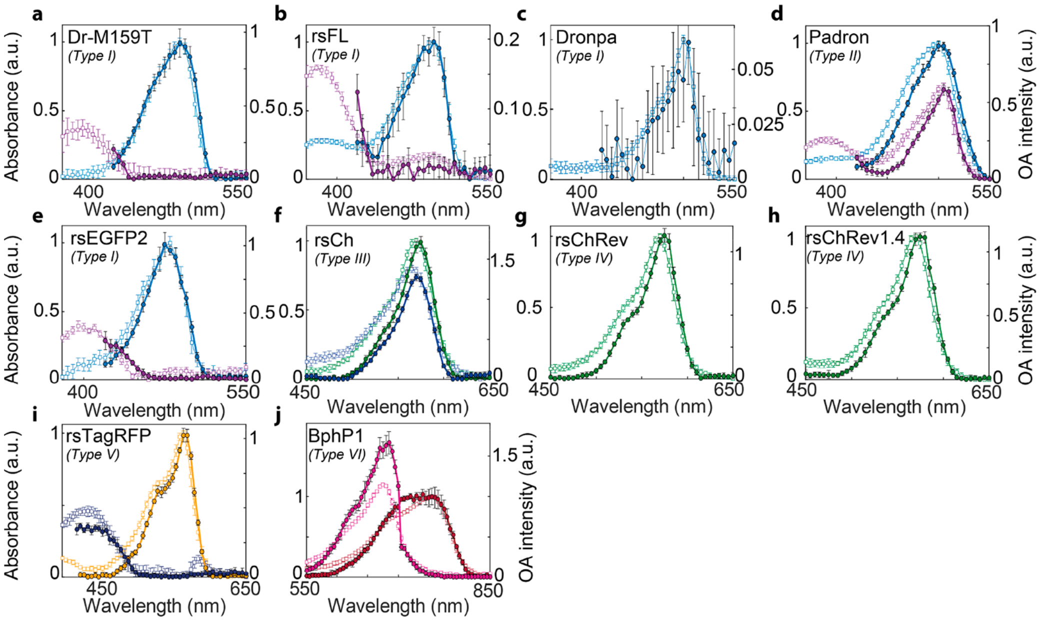

Figure 2. Optoacoustic spectra (solid symbols) and absorbance spectra (open symbols) of rsFPs in both switched states. Optoacoustic and absorbance spectra are chosen to ease comparison of the spectral features. The coloring of the curves refers to the switched states, respectively. All spectra are normalized to the absorbance state of the equilibrium spectra, defined as 1. The switching mode as described in Figure 1 is denoted in the upper left corner of each plot. For Dronpa (c), rsCherryRev (g), and rsCherryRev1.4 (h), no spectral change was observable upon switching. Optoacoustic and absorbance spectra that have been recorded simultaneously are shown in Figure S8. Abbreviations: Dr = Dronpa, rsFL = rsFastLime, Ch = Cherry.

generated with a duty cycle of 99.9%. The output of the laser diode was directly attached to a multimode fiber. Before the experiment, the power for all the pulse durations was measured with a powermeter (Thorlabs), and the amplitude of the triggering pulses was adjusted to ensure 500 μW power for all pulse durations at the output of the fiber. Purified superfolder GFP protein was inserted in a coverslip and illuminated for 300 s. Fluorescence signals were band-pass-filtered from 500 to 570 nm, detected with an avalanche photodiode (SPCM-AQRH-13, Excelitas), and digitized at a sampling rate of 100 samples/s with a data acquisition card (PCIe-6353, National Instruments). The mean noise level was subtracted from the data, and subsequently the fluorescence signal amplitude was normalized and its minimum set to zero.

■ RESULTS AND DISCUSSION

In choosing the rsFPs for this work, we tried to cover a representative range of this protein class (Figure 1 and Table 1,[4,20,47,25,40−46]). However, we focused on the derivatives of the green rsFP Dronpa,[40] since this group combines proteins with different switching kinetics and directionality at similar wavelengths whose photophysics have been extensively studied. We analyzed all proteins by use of a unique custom-built spectrometer setup (Figure S1) equipped with a tunable (420−2100 nm) pulsed laser with a repetition rate of 50 Hz, pulse duration of 7 ns, and energies of ∼1.3 mJ, which allowed us to record high-quality optoacoustic spectra (Figure S7) in conjunction with the absorption spectra (see Experimental Section for details).

Optoacoustic and Absorption Spectra Characteristics. In contrast to fluorescence detection, a low QY and thus a high level of nonradiative de-excitation favors the generation of optoacoustic signals (photoacoustic generation efficiency, PGE). To determine the PGE and analyze spectral characteristics of rsFPs, we recorded optoacoustic as well as absorbance spectra of the equilibrium state and, where possible, the switched state (Figure 2). In general, the spectral shapes of optoacoustic and absorbance spectra coincide very well (R^2 higher than 0.94), with only minimal differences observed in the case of proteins showing very low optoacoustic signal (e.g., Dronpa, R^2 = 0.80; Figure 2c). The absorbance spectra depicted in Figure 2 is an averaging of several absorbance spectra at the onset of each switching cycle. A comparison with the absorbance at each wavelength, measured simultaneously with the respective wavelength in the optoacoustic spectra, can be found in Figure S8. Differences directly relate to the influence of QY and, to a lesser extent, other decay channels on the PGE and allow us to quantify its contribution for the different proteins. In Figure 2, rsEGFP2 (e), Dronpa-M159T (Dronpa 2) (a), rsFastLime (b), Dronpa (c), rsTagRFP (i), and *Rhodopseudomonas palustris* bacteriophytochrome (BphP1) (j) are proteins with switching predominantly governed by photochromism. For these proteins, upon switching, the optoacoustic spectra closely follow the absorbance spectra, resulting in optoacoustic signal differences between the on and off states of ∼100% for Dronpa-M159T, rsEGFP2, rsTagRFP, and BphP1 as well as ∼90% for rsFastLime, resulting in a high dynamic range of switching (Table 1). rsFastLime shows an absorbance in the 488 state after switching, which, however, cannot be seen in the optoacoustic spectra, possibly hinting at a residual 488 population with very low fluorescence and PGE. This could be a state with high positional freedom prior to isomerization. Despite Dronpa being equally switchable like, for example, Dronpa-M159T, the slow switching of the wild-type protein could not be resolved in our optoacoustic spectra (see next section); moreover, the high QY leads to very low PGE, complicating the measurement.

DOI: 10.1021/acs.analchem.8b02599
Anal. Chem. 2018, 90, 10527−10535

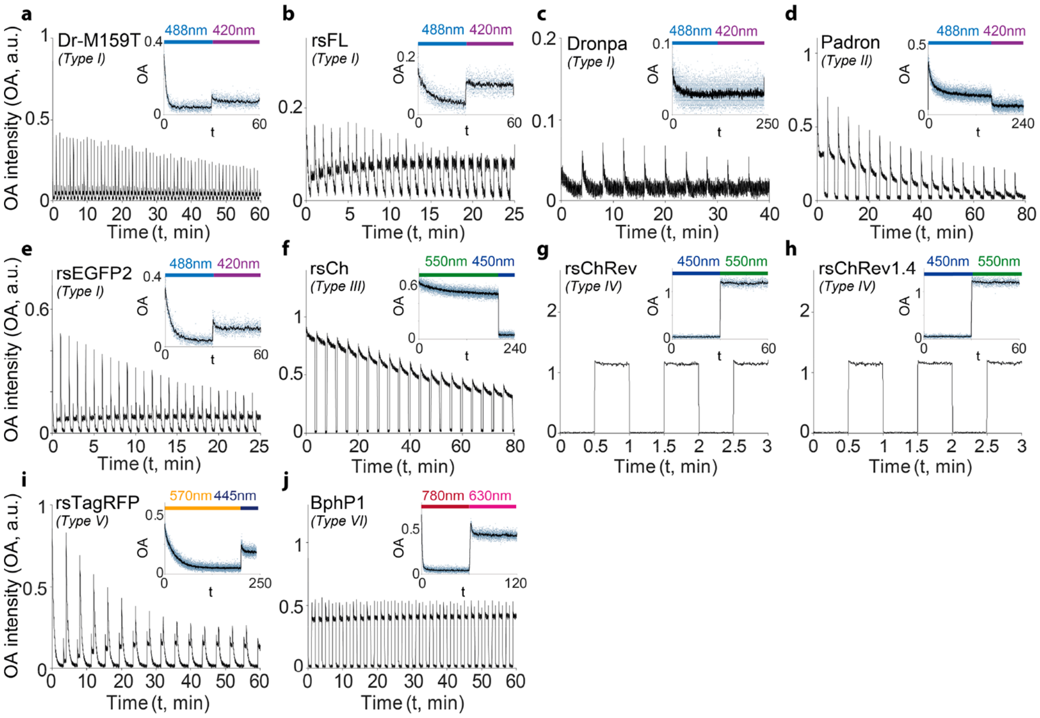

Figure 3. Change of optoacoustic signal of rsFPs upon switching with light of different wavelengths. Shown are several switching cycles per protein. Insets show a single cycle, with the excitation used and switching light denoted as a bar above the trace. Abbreviations are as in Figure 2.

In contrast to the photochromes, the switching of rsCherryRev and its sibling rsCherryRev1.4 (Figure 2g,h) is dominated by changes in QY. Accordingly, we see no change in absorbance spectra upon switching; however, also, the change in QY of the already poorly fluorescent proteins results in too small a change in the optoacoustic spectra to be resolved by our optoacoustic spectrometer (see next section).

Padron and rsCherry (Figure 2d,f) show a combination of QY change and photochromism, with the switched spectra exhibiting a lower absorbance at 488 and 550 nm, respectively, but a higher QY. This is clearly reflected in higher optoacoustic signal for those switched states with dynamic ranges of ~50% and ~20%, respectively. As a result, the two proteins that are positive switchers for fluorescence (i.e., irradiation with excitation wavelength switches on) are negative switchers for optoacoustics, since both the lowered absorbance and increased QY have detrimental effects on the optoacoustic signal. We used absorption data and the optoacoustic signal of the same sample at similar wavelengths to calculate the PGE (Table 1). In general, fluorescent proteins present an absorption spectrum with the main band exhibiting a blue-shifted shoulder. As can be observed in Figure S9, the PGE of this shoulder when calculated by its own absorbance is significantly lower than that of the main peak. This phenomenon is stronger in red proteins.

As described previously,[48] the optoacoustic signal generation is inversely linked to the QY. Dronpa, with a very high QY of 0.85, shows the weakest optoacoustic signal with a PGE < 0.1, while the poor QYs of 0.3 for rsEGFP2 and 0.23 for Dronpa-M159T result in PGEs of ~0.5 and ~0.7, respectively. Moreover, rsCherryRev, exhibiting a very low QY of 0.005,[4] shows also only a PGE of ~0.5, hinting that small changes in QY are negligible for optoacoustics. Interestingly, the two “positive” rsFPs, Padron and rsCherry, show higher PGEs than their respective relatives Dronpa-M159T and rsCherryRev, despite exhibiting comparable or even higher QY. It is interesting to note that positive rsFPs are described as having a more space-conserving isomerization route for their chromophores involving fewer rearrangements in the vicinity of the chromophore.[25,49] Whether this is connected to the different PGE remains to be elucidated. Overall, the data show that photochromic rsFPs can provide a high dynamic range in optoacoustics, whereas QY-change rsFPs, especially those with initially low QY, support only infinitesimal optoacoustic signal modulation.

Switching Behavior of Reversibly Switchable Fluorescent Proteins in Optoacoustics. Switching behavior under optoacoustic (i.e., pulsed) illumination is the crucial factor determining the usability of an rsFP in optoacoustics. We recorded switching kinetics of all rsFPs by multiple cycles of alternating switching wavelengths (Figure 3; see Figure 1 for details on the switching schedule and mode). The studied green rsFPs provide a set that allows direct comparison of switching kinetics under comparable illumination. The trend known from fluorescence switching, with kinetics ranging from slow-switching Dronpa to fast-switching Dronpa-M159T and rsEGFP2, is also observable in optoacoustics. However, the overall switching at the given repetition rate of 50 Hz is much slower than in fluorescence imaging (Figure 4). This can be attributed to the pulsed illumination used in optoacoustics. Depending on the repetition rate of the laser, only a small part of the pulse provides illumination while for the remaining time the sample is dark. Since the switched states in rsFPs are metastable and naturally relax in the absence of illumination to their equilibrium state, the dark time between pulses allows partial recovery of the equilibrium state, effectively counteracting the switching. We demonstrated this dependency by switching with three different laser repetition rates (10, 25, and 50 Hz; Figure 4A). The switching halftime increased from ~5 s at 50 Hz to ~25 s at 10 Hz. For high-repetition laser systems,

DOI: 10.1021/acs.analchem.8b02599
Anal. Chem. 2018, 90, 10527−10535

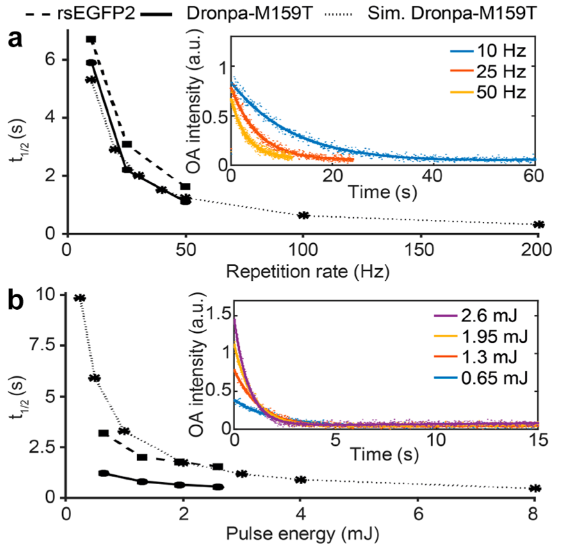

Figure 4. Dependency of switching times on (a) laser repetition rate and (b) laser energy for rsEGFP2 and Dronpa-M159T, as well as predicted development for Dronpa-M159T (dotted line). The insets show exemplary switching behavior for Dronpa-M159T at different repetition rates (a) or pulse energies (b).

the effect of the natural relaxation between pulses is negligible. A measurement of rsEGFP2 with a 20 MHz repetition rate shows switching halftimes of 0.4 ms ± 0.1 ms (Figure S10). Both results match well with a theoretical approximation of the switching and recovery under pulsed illumination using two-exponential functions (Figure 4A). As for fluorescence, switching kinetics in optoacoustics show an exponential dependence on illumination intensities (Figure 4B). For the rsFP derivatives of mCherry, the change of QY upon illumination is the major source of fluorescence modulation. For fluorescence, this results in sufficient signal modulation, but for optoacoustics, the small change from low to even lower QY translates to infinitesimal signal changes. Most rsCherry and rsCherryRev molecules are off in the equilibrium state, which translates to an optoacoustic on-state; the change upon switching translates to a change of only a few percent of the original signal (Figure 3g,h). This suggests that, for optoacoustic applications, photochromic rsFPs are generally much more favorable.

Photofatigue of Reversibly Switchable Fluorescent Proteins under Optoacoustic Illumination. Photofatigue (permanent bleaching or long-lived dark states) is an essential parameter in every imaging experiment, since it limits the maximal dwell time. We determined the number of possible switching cycles for our set of rsFPs under our illumination conditions (Figure S11). For the GFP-like rsFPs, Dronpa-M159T shows the least bleaching. However, it is clearly surpassed by the far-red bacteriophytochrome BphP1. Toward elucidating the general difference between continuous and the pulsed-energy deposition used in optoacoustics, we compared the photofatigue of superfolder green fluorescent protein (sfGFP)[50] under four illumination conditions at the same power: 10 ns/50 MHz (pulse width/repetition rate), 100 ns/5 MHz, 1 μs/500 kHz, and continuous, all deposited the same power of 500 μW, allowing comparison (Figure 5). We selected a nonswitchable protein for this experiment in order not to confound switching with photofatigue. The results show an accelerated bleaching for pulsed illumination, which scales inversely with pulse length. This effect could be attributed to multiple photons absorbed by each chromophore, resulting in transitions to long-lived or photolytic higher-order singlet and triplet states S_n and T_n.[51]

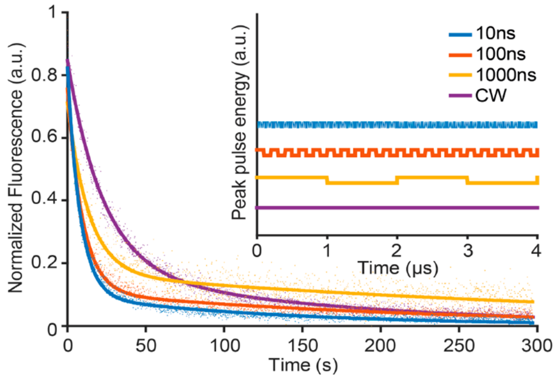

Figure 5. Dependence of photofatigue of sfGFP, as an exemplary fluorescent protein, on the illumination type (continuous or different types of pulsed). Illumination patterns used are depicted in the inset.

Implications for Optoacoustic Imaging Applications Employing Reversibly Switchable Fluorescent Proteins. In this work, we comprehensively explore the characteristics of rsFPs in the context of optoacoustics. In general, photochromes are better suited for optoacoustic applications than QY-changers. Since the latter already exhibit a low QY corresponding to a high optoacoustic signal in the fluorescence on-state, the small change to an even lower QY in switched-off state translates to a poor dynamic range for the optoacoustic signal. The dynamic range of negative-switching photochromes is directly governed by the change in absorption spectra, which is often near 100%. Due to the natural relaxation of rsFPs, the dark times of pulsed illumination effectively result in slowed switching kinetics. Thus, high-repetition laser systems are beneficial because they accelerate switching. They also reduce the number of pulses necessary for switching, decreasing overall exposure and hence photofatigue. rsFPs always show a faster and a slower switching kinetics, with the fast kinetics being in most cases in the direction of the equilibrium state. Ideally, optoacoustic readout and switching is achieved with this wavelength by use of pulsed illumination, and the reverse process is achieved by use of a second continuous illumination. This is especially true since, as demonstrated in this paper, the photofatigue depends on pulse length and repetition rate. On the other hand, for both on- and off-switching, kinetics for photochromic rsFPs can be used for optoacoustic readouts to gain additional CNR.

This distinct switching kinetics of rsFPs can be exploited in various optoacoustic imaging modalities, which can be classified by their penetration depth and resolution. This optoacoustic specific scalability can be approximated by the rule of thumb that penetration depth/resolution ≈ 200.[52] Main optoacoustic imaging modalities include high-resolution optical-resolution photoacoustic microscopy (OR-PAM), acoustic-resolution photoacoustic microscopy (AR-PAM), and deep-penetration photoacoustic computed tomography (PACT).[11] The beneficial use of rsFPs for optoacoustic imaging, based on the gain in CNR, has already been demonstrated for OR-PAM[20] and PACT.[20−23] The different sizes of optical excited regions [focused/full field-of-view (FOV)] influence the suitability of different rsFPs, light modulation schemes, and temporal unmixing concepts.

DOI: 10.1021/acs.analchem.8b02599
Anal. Chem. 2018, 90, 10527−10535

For OR-PAM approaches, the pixel dwell time is essentially governed by the switching necessary to achieve the required CNR. Scanning systems that operate with high laser repetition rates could benefit from fast transient modulation of the signal, achievable by several of the fluorescence imaging optimized photochromic rsFPs. In acoustic-resolution mesoscopy systems like raster-scanning optoacoustic mesoscopy (RSOM), a broad FOV is illuminated while only single positions are read out at the acoustic focus. The approach of recording the full switching at each position results in continuous full exposure of the sample and considerable photofatigue. An alternative could be that the sample is continuously scanned at the acoustic focus while the whole illuminated area is modulated differently by each FOV passage, thus sparsely capturing different points of the switching curve of each pixel, reducing the total exposure and hence the photofatigue. The switching kinetics for each position can be delineated by locked-in detection and separating the modulated protein in the frequency domain. In this context, the use of fast switching rsFPs in optoacoustic approaches operating with laser diodes[39] with very high repetition rates (>500 kHz) can be advantageous. For optoacoustic systems with a large FOV and an acoustic-resolution tomography approach (PACT) like multispectral optoacoustic tomography (MSOT),[53] that operate with high laser powers and low repetition rates, full switching and temporal unmixing by difference images is a viable method. For such systems, other modes of signal modulation are also conceivable; for example, a change of the optoacoustics signal through reversible micellization, leading to quenching of the signal.[54]

Overall, to date switchable bacteriophytochromes are likely the best proteins for most optoacoustic applications, due to their good dynamic range and resistance to photofatigue and, foremost, due to their wavelength in the NIR, which is essential for tomography experiments with deep penetration and in vivo work in mammalians due to the prevalence of hemoglobin as a strong absorber below 700 nm. However, also very fast switching green photochromic rsFPs like Dronpa-M159T or rsEGFP2 can be beneficial for various optoacoustic imaging applications. Due to the facility of boosting the CNR by temporal unmixing and the equivalent absorption spectrum to GFP, Dronpa-M159T and rsEGFP2 can directly be used as transgene labels in model organisms like *Drosophila melanogaster* pupae and adult zebrafish and thus further improve the optoacoustic imaging capabilities for morphological and functional studies in developmental biology.[55]

The four rsFPs used to date for optoacoustic imaging are either designed for fluorescence or are wild-type proteins. Dedicated protein engineering of reversible switchable proteins for optoacoustic (rsOAPs) will most likely originate from bacteriophytochromes, due to their natural low QY, high absorbance, and resistance to photofatigue, and will focus on accelerating their switching kinetics. Moreover, maintaining a high metastability is especially relevant for use in low-repetition-rate systems. The photostability of classical green rsFPs must be improved if these proteins are to be useful. Despite the clear advantage in dynamic range of negative-switching photochromes, the surprisingly high PGE of positive-switchers remains an interesting factor. Fully photochrome positive-switching proteins could be a useful development in this direction.

■ CONCLUSION

To summarize, in this work we investigated the characteristics and performance of a broad range of rsFPs in optoacoustics. We provide full optoacoustic spectroscopy and switching kinetic data for all investigated proteins, allowing conclusions on the influence of different switching approaches and protein characteristics on their performance as optoacoustic labels. To the best of our knowledge, this paper shows the first hybrid absorption and optoacoustic spectra on optoacoustic labels. Our study provides a framework for the use of rsFPs in optoacoustic imaging, which can increase the detectability and imaging contrast of transgene labels in the sample toward high penetration depth and high-resolution in vivo optoacoustic imaging.

■ ASSOCIATED CONTENT

Ⓢ Supporting Information

The Supporting Information is available free of charge on the ACS Publications website at DOI: 10.1021/acs.analchem.8b02599.

> Eleven figures showing multimodal OA and absorbance spectrometer, energy spectra, linearity and stability of OA compounds, exemplary waveforms and frequency response, temperature in sample chamber, improvement of OA spectra quality, OA and absorbance spectra of rsFPs, PGE of selected proteins, OA and fluorescence signal traces, and bleaching of rsFPs (PDF)

■ AUTHOR INFORMATION

Corresponding Author

*E-mail andre.stiel@helmholtz-muenchen.de.

ORCID

Andriy Chmyrov: 0000-0003-0265-019X
Andre C. Stiel: 0000-0001-8675-6797

Author Contributions

P.V. and K.M. performed the experiments, analyzed the data, and contributed equally to the paper. A.C. performed bleaching and high-repetition rate OA experiments. P.V. designed the OA spectrometer setup; K.M., J.P.F.-W. and A.C.S. contributed. J.P.F.-W. and V.N. contributed to the paper. A.C.S. conceived and designed the experiments and wrote the paper.

Notes

The authors declare no competing financial interest.

■ ACKNOWLEDGMENTS

We thank R. Hillermann for technical assistance, L. Prade and M. Steffner for discussions and help with the bleaching experiments, and A.C. Rodríguez for discussions on the manuscript. We thank Professor Stefan Jakobs (Max Planck Institute for Biophysical Chemistry and University of Göttingen Medical Faculty) for kindly providing several of the tested rsFPs. We thank Vipul Gujrati for help with the thermo-camera. This work was supported by the Federal Ministry of Education and Research, Photonic Science Germany, Tech2See-13N12624, 13N12623. The work of K.M. and A.C.S. was supported by the Deutsche Forschungsgemeinschaft (STI 656/1-1).

■ REFERENCES

(1) Shcherbakova, D. M.; Verkhusha, V. V. *Curr. Opin. Chem. Biol.* **2014**, *20*, 60−68.

(2) Betzig, E. *Angew. Chem., Int. Ed.* **2015**, *54* (28), 8034−8053.

(3) Sahl, S. J.; Hell, S. W.; Jakobs, S. *Nat. Rev. Mol. Cell Biol.* **2017**, *18* (11), 685−701.

(4) Zhou, X. X.; Lin, M. Z. *Curr. Opin. Chem. Biol.* **2013**, *17* (4), 682−690.

(5) Nienhaus, K.; Nienhaus, G. U. *Chem. Soc. Rev.* **2014**, *43* (4), 1088−1106.

(6) Duan, C.; Adam, V.; Byrdin, M.; Bourgeois, D. *Methods Mol. Biol.* **2014**, *1148*, 177−202.

(7) Oraevsky, A. A.; Jacques, S. L.; Tittel, F. K. *Appl. Opt.* **1997**, *36* (1), 402−415.

(8) Wang, L. V.; Hu, S. *Science (Washington, DC, U. S.)* **2012**, *335* (6075), 1458−1462.

(9) Taruttis, A.; Ntziachristos, V. *Nat. Photonics* **2015**, *9* (4), 219−227.

(10) Tzoumas, S.; Deliolanis, N.; Morscher, S.; Ntziachristos, V. *IEEE Trans. Med. Imaging* **2014**, *33* (1), 48−60.

(11) Wang, L. V.; Yao, J. *Nat. Methods* **2016**, *13* (8), 627−638.

(12) Ntziachristos, V. *Nat. Methods* **2010**, *7* (8), 603−614.

(13) Yao, J.; Wang, L.; Yang, J.-M.; Maslov, K. I.; Wong, T. T. W.; Li, L.; Huang, C.-H.; Zou, J.; Wang, L. V. *Nat. Methods* **2015**, *12* (5), 407−410.

(14) Wang, D.; Wu, Y.; Xia, J. *Neurophotonics* **2016**, *3* (1), 010901.

(15) Jokerst, J. V.; Cole, A. J.; Van de Sompel, D.; Gambhir, S. S. *ACS Nano* **2012**, *6* (11), 10366−10377.

(16) Beziere, N.; Lozano, N.; Nunes, A.; Salichs, J.; Queiros, D.; Kostarelos, K.; Ntziachristos, V. *Biomaterials* **2015**, *37*, 415−424.

(17) Qin, H.; Zhou, T.; Yang, S.; Chen, Q.; Xing, D. *Nanomedicine (London, U. K.)* **2013**, *8* (10), 1611−1624.

(18) Jokerst, J. V.; Thangaraj, M.; Kempen, P. J.; Sinclair, R.; Gambhir, S. S. *ACS Nano* **2012**, *6* (7), 5920−5930.

(19) Brunker, J.; Yao, J.; Laufer, J.; Bohndiek, S. E. *J. Biomed. Opt.* **2017**, *22* (7), 070901.

(20) Yao, J.; Kaberniuk, A. A.; Li, L.; Shcherbakova, D. M.; Zhang, R.; Wang, L. L. V; Li, G.; Verkhusha, V. V.; Wang, L. L. V. *Nat. Methods* **2016**, *13*, 67−73.

(21) Stiel, A. C.; Deán-Ben, X. L.; Jiang, Y.; Ntziachristos, V.; Razansky, D.; Westmeyer, G. G. *Opt. Lett.* **2015**, *40* (3), 367−370.

(22) Märk, J.; Dortay, H.; Wagener, A.; Zhang, E.; Buchmann, J.; Grötzinger, C.; Friedrich, T.; Laufer, J. *Commun. Phys.* **2018**, *1* (1), No. 3.

(23) Deán-Ben, X. L.; Stiel, A. C.; Jiang, Y.; Ntziachristos, V.; Westmeyer, G. G.; Razansky, D. *Opt. Lett.* **2015**, *40* (20), 4691−4694.

(24) Galanzha, E. E. I.; Nedosekin, D. a; Sarimollaoglu, M.; Orza, A. I.; Biris, A. S.; Verkhusha, V. V.; Zharov, V. P. *J. Biophotonics* **2015**, *8*, 81−93.

(25) Andresen, M.; Stiel, A. C.; Trowitzsch, S.; Weber, G.; Eggeling, C.; Wahl, M. C.; Hell, S. W.; Jakobs, S. *Proc. Natl. Acad. Sci. U. S. A.* **2007**, *104* (32), 13005−13009.

(26) Habuchi, S.; Dedecker, P.; Hotta, J.; Flors, C.; Ando, R.; Mizuno, H.; Miyawaki, A.; Hofkens, J. *Photochem. Photobiol. Sci.* **2006**, *5* (6), 567−576.

(27) Shcherbakova, D. M.; Baloban, M.; Verkhusha, V. V. *Curr. Opin. Chem. Biol.* **2015**, *27*, 52−63.

(28) Faro, A. R.; Adam, V.; Carpentier, P.; Darnault, C.; Bourgeois, D.; De Rosny, E. *Photochem. Photobiol. Sci.* **2010**, *9* (2), 254−262.

(29) Habuchi, S.; Ando, R.; Dedecker, P.; Verheijen, W.; Mizuno, H.; Miyawaki, A.; Hofkens, J. *Proc. NAtl. Acad. Sci. U.S.A.* **2005**, *102* (27), 9511−9516, DOI: 10.1073/pnas.0500489102.

(30) Jiménez-Banzo, A.; Nonell, S.; Hofkens, J.; Flors, C. *Biophys. J.* **2008**, *94* (1), 168−172.

(31) Byrdin, M.; Duan, C.; Bourgeois, D.; Brettel, K. *J. Am. Chem. Soc.* **2018**, *140* (8), 2897−2905.

(32) Kurian, E.; Prendergast, F.; Small, J. *Biophys. J.* **1997**, *73* (July), 466−476.

(33) Abbruzzetti, S.; Viappiani, C.; Murgida, D. H.; Erra-Balsells, R.; Bilmes, G. M. *Chem. Phys. Lett.* **1999**, *304* (3−4), 167−172.

(34) Brown, J. E.; Diaz, L.; Christoff-Tempesta, T.; Nesbitt, K. M.; Reed-Betts, J.; Sanchez, J.; Davies, K. W. *Anal. Chem.* **2015**, *87* (7), 3623−3630.

(35) Peters, K. S.; Snyder, G. J. *Science* **1988**, *241* (4869), 1053−1057.

(36) Braslavsky, S. E.; Ellul, R. M.; Weiss, R. G.; Al-Ekabi, H.; Schaffner, K. *Tetrahedron* **1983**, *39* (11), 1909−1913.

(37) Fonseca, M. B.; An, L.; Cox, B. T. *J. Biomed. Opt.* **2017**, *22* (12), No. 125007.

(38) Laufer, J.; Zhang, E.; Beard, P. *IEEE J. Sel. Top. Quantum Electron.* **2010**, *16* (3), 600−607.

(39) Stylogiannis, A.; Prade, L.; Buehler, A.; Aguirre, J.; Sergiadis, G.; Ntziachristos, V. *Photoacoustics* **2018**, *9*, 31−38.

(40) Ando, R.; Mizuno, H.; Miyawaki, A. *Science (Washington, DC, U. S.)* **2004**, *306* (5700), 1370−1373.

(41) Ando, R.; Flors, C.; Mizuno, H.; Hofkens, J.; Miyawaki, A. *Biophys. J.* **2007**, *92* (12), L97−9.

(42) Andresen, M.; Stiel, A. C.; Fölling, J.; Wenzel, D.; Schönle, A.; Egner, A.; Eggeling, C.; Hell, S. W.; Jakobs, S. *Nat. Biotechnol.* **2008**, *26* (9), 1035−1040.

(43) Grotjohann, T.; Testa, I.; Reuss, M.; Brakemann, T.; Eggeling, C.; Hell, S. W.; Jakobs, S. *eLife* **2012**.

(44) Stiel, A. C.; Andresen, M.; Bock, H.; Hilbert, M.; Schilde, J.; Schönle, A.; Eggeling, C.; Egner, A.; Hell, S. W.; Jakobs, S. *Biophys. J.* **2008**, *95* (6), 2989−2997.

(45) Lavoie-Cardinal, F.; Jensen, N. A; Westphal, V.; Stiel, A. C.; Chmyrov, A.; Bierwagen, J.; Testa, I.; Jakobs, S.; Hell, S. W. *ChemPhysChem* **2014**, *15* (4), 655−663.

(46) Subach, F. F. V; Zhang, L.; Gadella, T. T. W. J.; Gurskaya, N. G.; Lukyanov, K. A.; Verkhusha, V. V. *Chem. Biol.* **2010**, *17* (7), 745−755.

(47) Shcherbakova, D. M.; Shemetov, A. A.; Kaberniuk, A. A.; Verkhusha, V. V. *Annu. Rev. Biochem.* **2015**, *84*, 519−550.

(48) Laufer, J.; Jathoul, A.; Pule, M.; Beard, P. *Biomed. Opt. Express* **2013**, *4* (11), 2477.

(49) Andresen, M.; Wahl, M. C.; Stiel, A. C.; Gräter, F.; Schäfer, L. V.; Trowitzsch, S.; Weber, G.; Eggeling, C.; Grubmüller, H.; Hell, S. W.; Jakobs, S. *Proc. Natl. Acad. Sci. U. S. A.* **2005**, *102* (37), 13070−13074.

(50) Pédelacq, J.-D.; Cabantous, S.; Tran, T.; Terwilliger, T. C.; Waldo, G. S. *Nat. Biotechnol.* **2006**, *24* (1), 79−88.

(51) Eggeling, C.; Volkmer, A.; Seidel, C. A. M. *ChemPhysChem* **2005**, *6* (5), 791−804.

(52) Yao, J.; Wang, L. V. *Photoacoustics* **2014**, *2* (2), 87−101.

(53) Ntziachristos, V.; Razansky, D. *Chem. Rev.* **2010**, *110* (5), 2783−2794.

(54) Wang, J.; Lin, C.-Y.; Moore, C.; Jhunjhunwala, A.; Jokerst, J. V. *Langmuir* **2018**, *34* (1), 359−365.

(55) Razansky, D.; Distel, M.; Vinegoni, C.; Ma, R.; Perrimon, N.; Köster, R. W.; Ntziachristos, V. *Nat. Photonics* **2009**, *3* (7), 412−417.

(56) Stiel, A. C.; Trowitzsch, S.; Weber, G.; Andresen, M.; Eggeling, C.; Hell, S. W.; Jakobs, S.; Wahl, M. C. *Biochem. J.* **2007**, *402* (1), 35−42.

(57) Shcherbakova, D. M.; Sengupta, P.; Lippincott-Schwartz, J.; Verkhusha, V. V. *Annu. Rev. Biophys.* **2014**, *43* (1), 303−329.

Appendix VI – Publication 2

RESEARCH METHODS

Multiplexed whole-animal imaging with reversibly switchable optoacoustic proteins

Kanuj Mishra[1], Mariia Stankevych[1], Juan Pablo Fuenzalida-Werner[1], Simon Grassmann[2], Vipul Gujrati[1,3], Yuanhui Huang[1,3], Uwe Klemm[1], Veit R. Buchholz[2], Vasilis Ntziachristos[1,3], Andre C. Stiel[1]*

We introduce two photochromic proteins for cell-specific in vivo optoacoustic (OA) imaging with signal unmixing in the temporal domain. We show highly sensitive, multiplexed visualization of T lymphocytes, bacteria, and tumors in the mouse body and brain. We developed machine learning–based software for commercial imaging systems for temporal unmixed OA imaging, enabling its routine use in life sciences.

INTRODUCTION

Photo- or optoacoustic (OA) imaging combines optical contrast with ultrasound resolution, enabling high-resolution, real-time in vivo imaging well beyond the 1-mm penetration depth typical of microscopy methods (*1*, *2*). OA has already provided intriguing insights into tumor heterogeneity (*3*), neuronal dynamics (*4*), psoriasis (*5*), and brown fat metabolism (*6*) based on endogenous contrast from hemoglobin and lipids (*7*, *8*). This is complemented by theranostic research (*9*, *10*) and clinical application (*11*), e.g., imaging of Crohn's disease (*12*). However, OA imaging has not yet become a routine tool in life sciences because of the lack of strong OA contrast agents that can be expressed in desired cell types (*13*). The few transgenic labels used in OA so far (*8*) give weak signals that cannot rise above the strong background due to hemoglobin. Photochromic proteins that can be reversibly switched between two states by light can overcome this limitation by entirely separating the label signal, which modulates in accordance with the illumination, from the background, which remains constant (*14*). This concept, despite being validated in several studies (*15*–*20*), has not been implemented widely because it requires complex instrumentation and data analysis tools. Here, we introduce two reversibly switchable OA proteins (rsOAPs) and demonstrate their use with widely accessible off-the-shelf commercial imaging systems as well as our open-access machine learning (ML)–based software code for analysis. One of our new rsOAPs shows high switching speeds and dynamic range of photomodulation that allow us to resolve the signals of different cell populations labeled with differentiable rsOAPs in close proximity in the same animal, demonstrating the potential for simultaneous tracking of different cellular processes through temporal multiplexing.

RESULTS

Engineering of rsOAPs

Bacterial photoreceptors called bacteriophytochromes (BphPs) (*21*) have emerged as most suitable for rsOAP development due to their strong absorption in the near-infrared range and low photofatigue (*22*). To identify the most promising candidate for further development, we screened eight native BphPs (table S1) and selected the one from *Rhizobium etli*. A set of truncations enabled us to minimize its size and optimize its photoswitching characteristics. In brief, on the basis of existing structural data as well as homology models, we created truncations containing the minimum PAS-GAF-PHY photosensory core domains [photosensory core module (PCM)] together with extra amino acids from the annotated linkers between PHY and histidine kinase domains and tested their characteristics in regard to signal generation and photoswitching (Fig. 1, A to E,

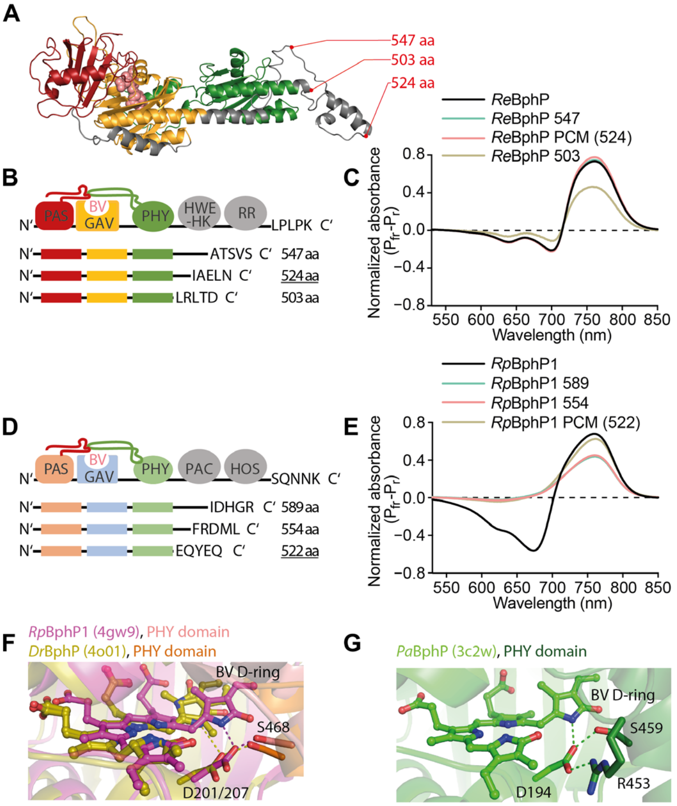

Fig. 1. Structure-guided design of rsOAPs. (**A**) Homology model (iTasser, based on 6g1y) of *Re*BphP-PCM. Truncation sides indicated. (**B**) Schematic representation of truncations. (**C**) Photoinduced differential spectra for truncations. (**D** and **E**) Similar representations for *Rp*BphP1. (**F**) Stabilization of the BV D-ring in *Rp*BphP1 and *Dr*BphP. (**G**) Similar representation for PaBphP, which shows an arginine similar to *Re*BphP, presumably abstracting D194 and destabilizing the P_{fr} state, yielding a faster photoswitching.

---

[1] Institute of Biological and Medical Imaging (IBMI), Helmholtz Zentrum München, Neuherberg, Germany. [2] Institute for Medical Microbiology, Immunology and Hygiene, Technische Universität München (TUM), Munich, Germany. [3] Chair of Biological Imaging and Center for Translational Cancer Research (TranslaTUM), Technische Universität München (TUM), Munich, Germany.
*Corresponding author. Email: andre.stiel@helmholtz-muenchen.de

and note S1). The final variant *Re*BphP-PCM shows twofold larger change in OA signal (Fig. 2G), more than fivefold faster switching (Fig. 2, C and D), and greater resistance to photofatigue than other rsOAPs (Fig. 2E), while its high molar absorbance is on par with the recently described *Deinococcus radiodurans Dr*BphP-PCM (92,000 M^{-1} cm^{-1}; Fig. 2, B and G) (*19*). Those characteristics enable higher numbers of switching cycles per second, which improves sensitivity and allows imaging over longer timeframes. On the molecular level, this acceleration of switching speed is the result of a less stabilized P_{fr} state favoring the photoinduced transition to P_r. The destabilization is likely caused by an arginine present in *Re*BphP but not in *Rp*BphP1 and *Dr*BphP. This arginine, by interacting with a conserved aspartate, which, in turn, interacts with the D-ring of the P_{fr} state chromophore, weakens P_{fr} stabilization (Fig. 1, F and G, and note S1).

Our truncation strategy also proved successful in obtaining a switchable *Rp*BphP1-PCM from *Rhodopseudomonas palustris*, in contrast to a previous report that truncated forms of this protein do not undergo reversible switching (*19*). Our engineered *Rp*BphP1-PCM maintains the far-red state (P_{fr}) extinction coefficient and photochromic behavior of the parental *Rp*BphP1 (Figs. 1E and 2B and fig. S1), and the change in its OA signal following illumination at 770 nm is similar to that of the previously described *Dr*BphP-PCM (Fig. 2G). (Plasmid for expressing *Re*BphP-PCM in bacteria and eukaryotic cells or for introduction into viral vectors can be obtained from Addgene.) Both new rsOAPs are monomeric (fig. S2) and show higher expression in mammalian cells than the full-length parental proteins (fig. S3). The two developed rsOAPs and *Dr*BphP-PCM show distinctive switching speeds, which is the reason for our ability to discriminate the proteins in vivo successfully. As a result, probes expressed in different cells in close proximity in the animal can be distinguished during high-resolution OA imaging.

OA imaging using ML-based temporal unmixing

We performed all OA imaging using an off-the-shelf, commercially available multispectral OA tomography device with a 10-Hz pulsed tunable laser and a 256-element transducer array (MSOT, iThera Medical). Off-switching of rsOAPs was achieved with light at 770 nm, which gave the highest difference in OA signal intensity between the "on" and "off" states (fig. S5A), while on switching was achieved using light at 680 nm. Lower wavelengths did not substantially improve the transition to the on state (fig. S5B). The number of laser pulses per wavelength was chosen to cover the full switching kinetics, but it can be significantly reduced using information-content analysis, which allows an estimate of the minimal number of cycles and pulses per cycle required to discern the labeled structure, thus effectively limiting imaging dwell time, which is essential for, e.g., time-resolved studies (Fig. 2H, fig. S6, and note S2). All temporal unmixing was conducted with in-house code developed to analyze time-varying patterns in the reconstructed data in the frequency and time domains using classic ML approaches (Fig. 3, Materials and Methods, and notes S3 and S4). In brief, after running fluence and motion correction on the data, a range of distinctive features

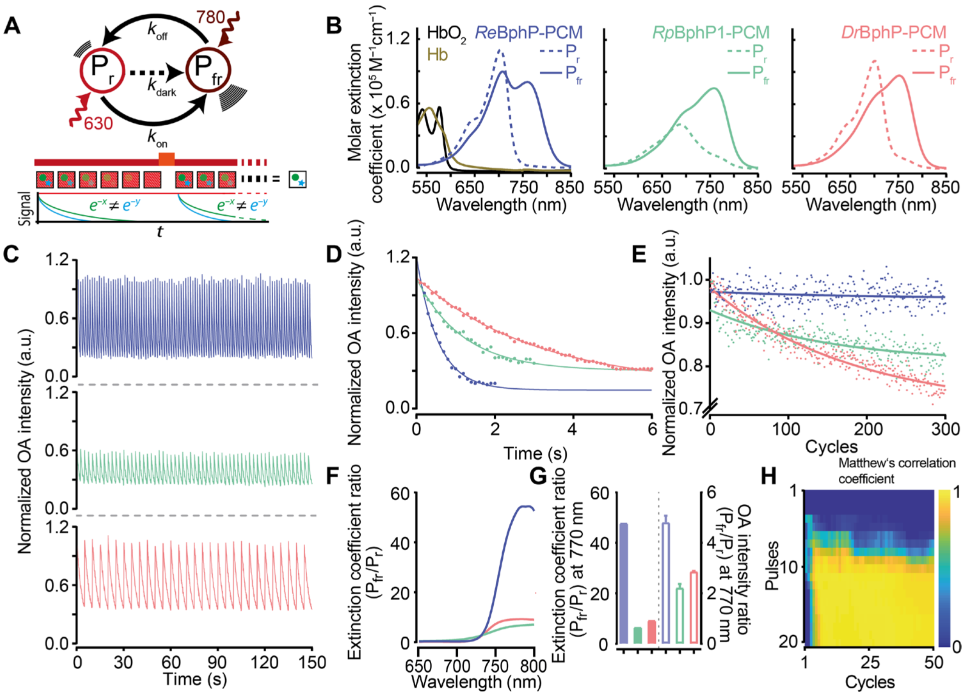

Fig. 2. In vitro characterization of *Re*BphP-PCM and *Rp*BphP1-PCM in comparison to *Dr*BphP-PCM. (**A**) Principle of photoswitching in BphPs (top) and concept of temporal unmixing of two labels (green ball and blue star; bottom). Illumination shown in dark red (780 nm) and red (630 nm). P_r refers to the red state, while P_{fr} refers to the far-red state. The bottom part of the panel was adapted with permission from (*14*). (**B**) Absorbance spectra of P_r and P_{fr} states of the three rsOAPs in comparison to hemoglobin (HbO_2 and Hb, 1999, S. Prahl, omlc.org). (**C**) Switching cycles of the rsOAPs. Only OA signal at 770 nm is shown. a.u., arbitrary units. (**D**) Single switching cycle from (C), shown with an exponential fit. (**E**) Photofatigue of the proteins per cycle. (**F**) Absorbance ratio between the P_{fr} and P_r state for different wavelengths. (**G**) Absorbance (filled bars) and OA signal intensity (hollow) ratio between the P_{fr} and P_r state for the three rsOAPs at 770 nm. (**H**) Matthew's coefficient shown as a function of number of cycles and pulses. Shown is the analysis of a 4T1 tumor expressing *Re*BphP-PCM; histology was used as ground truth. All proteins have been adjusted to equal Soret peak absorption.

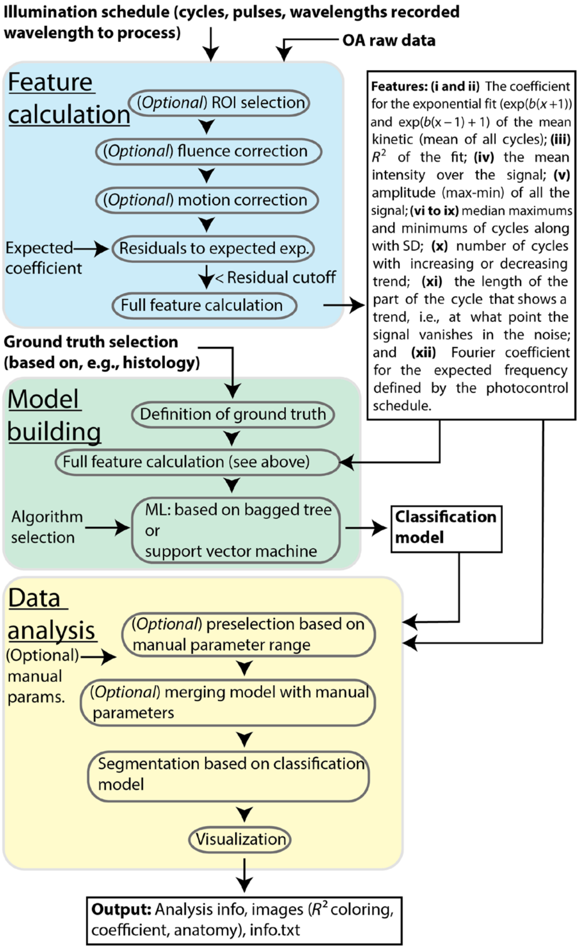

Fig. 3. Schematic flow of the ML-based analysis strategy and main scripts. The time-varying patterns in the OA raw data are extracted in the "Feature calculation" (blue) and analyzed using a classification model in the "Data analysis" step (yellow). In "Model building" (green), a classification model is trained based on imaging data with associated histology ground truth. In the script, two algorithms can be selected: bagged tree or support vector machine. For uniformity, the images shown in this work exclusively use the bagged tree approach, although the support vector machine has some virtues (note S4).

was extracted from the photomodulated signal for each voxel of the tomography images. On the basis of a set of these data and corresponding histology as ground truth, a bagged random forest algorithm (*23*) was trained and validated on independent datasets of a different type to prevent overfitting. The ensuing model was then used to analyze all data in this study. The code for data preparation, for analysis with the model used in this work, and for generation of new models is available to the community along with graphical user interfaces.

The OA imaging scheme is shown in Fig. 4A. First, we used rsOAPs for superficial in vivo imaging. We imaged the development of 4T1 mouse mammary gland tumors coexpressing *Re*BphP-PCM and green fluorescent protein (GFP) after they were grafted onto the backs of FoxN1 nude mice ($n = 3$). The initial population of 0.8 × 10^6 injected cells was readily visualized separate from all background absorbers (Fig. 4B), as was the growing tumor mass at all days after injection (fig. S7, A to D). To test whether this imaging is also possible in brain tissue after light passes through the skull, we implanted 0.7 × 10^6 4T1 cells coexpressing *Re*BphP-PCM and GFP at a depth of 3.6 mm and imaged them immediately thereafter. Comparison of the OA images with fluorescence images obtained after sacrificing mice revealed perfect overlap of the labeling, confirming background-free identification of 1.4 × 10^5 cells deep in the mouse brain (Fig. 4C). Next, we used the same rsOAP to image deep-seated tumors of HCT116 human colon carcinoma cells implanted intraperitoneally ($n = 2$). From day 3 onward, we were able to visualize the growth of several individual tumor sites to a depth of ~1 cm (fig. S7, E and F). Comparison of OA images and histology obtained after sacrifice confirmed identification of all malignant tissue (Fig. 4, D to F, and fig. S7, E and G), including small tumors or metastatic patches containing less than 10,000 cells (fig. S7, I and J).

To assess the sensitivity of imaging with our rsOAPs, we imaged dorsal implants of Matrigel containing different numbers of Jurkat T lymphocytes stably coexpressing *Re*BphP-PCM and GFP in mice (Fig. 4G). We detected populations as small as 500 cells/μl, suggesting the potential for sensitive tracking of immune processes. Similarly, imaging of dorsal implants of Matrigel containing bacteria expressing *Re*BphP-PCM detected populations as small as 14,000 bacteria/μl (Fig. 4H). This sensitivity may be useful for studying and optimizing bacteria-based tumor therapies (*24*).

A strong advantage of photocontrollable labels is the possibility to delineate multiple labels based on their individual switching kinetics. To demonstrate this, we imaged 1-mm alginate beads filled with *Escherichia coli* expressing *Re*BphP-PCM, *Rp*BphP1-PCM, or *Dr*BphP-PCM. All beads were unambiguously identified on the basis of their switching kinetics (Fig. 5A). The same differentiation was achieved in vivo after implanting Jurkat T lymphocytes expressing *Re*BphP-PCM or *Dr*BphP1-PCM and *E. coli* expressing *Rp*BphP1-PCM into the back of mice (Fig. 5B).

Because the kinetics of photoswitching are energy dependent, fluence changes due to light attenuation by surrounding absorbers—photochromic or static—complicates temporal multiplexing (note S5). Thus, one aim of our development of the fast-switching *Re*BphP-PCM was to achieve a switching time constant clearly separate from other rsOAPs. We show that 4T1 tumor expressing *Re*BphP-PCM and GFP are readily distinguished from infiltrating *Dr*BphP-PCM–expressing *E. coli* cells (intratumorally injected 10^8 bacteria; Fig. 5, D and E). This means that multiplexing is possible for co-registration studies and that the concentrations of the labels can be estimated based on the convoluted kinetics (fig. S8). Similarly, we show this for two populations of rsOAP labeled Jurkat T lymphocytes in a 4T1 tumor (intratumorally injected 5 × 10^5 cells; Fig. 5C). Hence, temporally unmixed multiplexed OA imaging of cells of the immune system enables following their function and involvement in disease mechanism in vivo, longitudinal on the organism level.

DISCUSSION

The combination of OA and transgenic rsOAP labels allows the tracking of specific cell populations in vivo, which can open up possibilities for longitudinal studies of intact animals in diverse fields such as immunology, developmental biology, neurology, and cancer research. To support these studies, we describe next-generation rsOAPs that provide faster switching and greater resistance to photofatigue than existing rsOAPs, allowing highly sensitive detection, and importantly true multiplexing, without interference from hemoglobin or other abundant absorbers in vivo. These rsOAPs can be used with

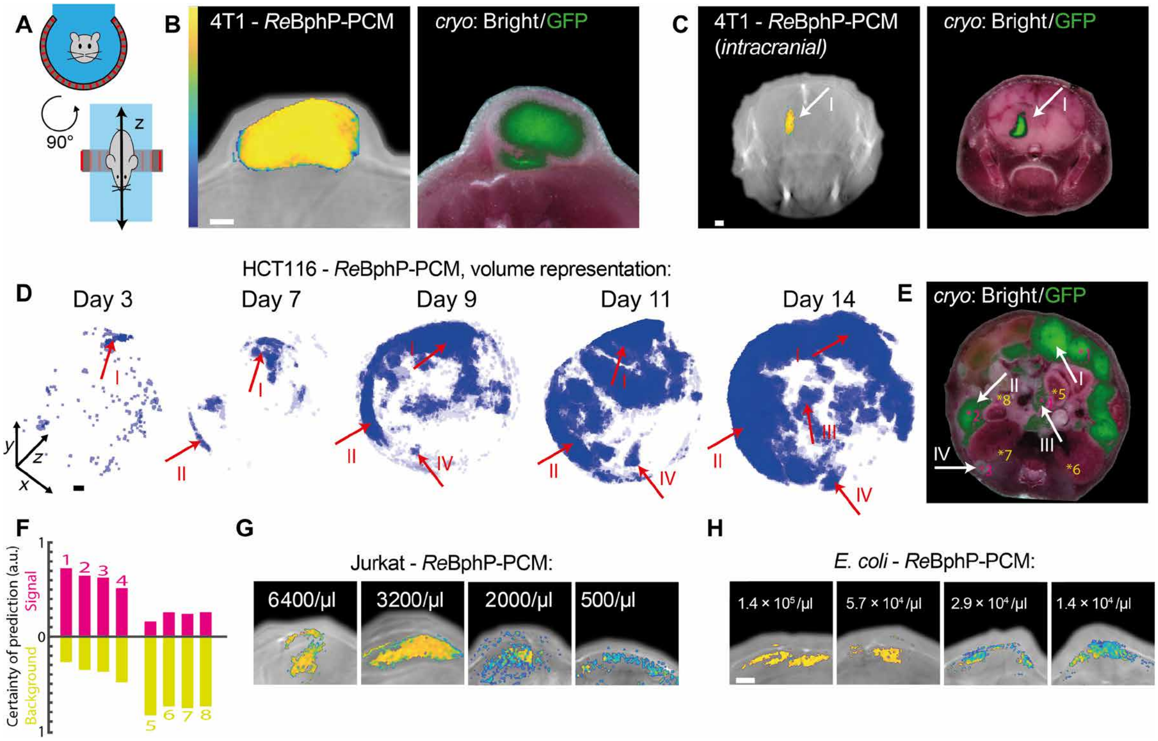

Fig. 4. MSOT imaging of *Re*BphP-PCM and other rsOAPs. In certain experiments, GFP was coexpressed to allow fluorescence imaging of histology slices. (**A**) Schematic of OA tomography used in this work. (**B**) 4T1 cells (0.8×10^6 injected subcutaneously) stably expressing *Re*BphP-PCM and imaged on day 9. (**C**) 4T1 cells (0.7×10^6 injected intracranially) stably expressing *Re*BphP-PCM imaged at a depth of 3.6 mm in the brain (arrow I) immediately after injection. (**D**) Volume representation of HCT116 cells (1.5×10^6 injected intraperitoneally) stably expressing *Re*BphP-PCM at consecutive time points. (**E**) Histology of the same mouse at day 14. (D and E) Arrows indicate distinctive tumor masses. (**F**) Certainty of prediction (weighted sum of tree scores) indicating quality of discerning label signal or background of regions of interest shown in (E) (right). (**G**) Imaging of the indicated concentrations of Jurkat T cells in Matrigel expressing *Re*BphP-PCM immediately after subcutaneous implantation; because of the polymerization process, no homogeneity is expected. (**H**) Imaging of the indicated concentrations of *E. coli* expressing *Re*BphP-PCM in Matrigel immediately after subcutaneous implantation. In (B), (C), (G), and (H), color maps refer to R^2 (detection quality). All slices are single representative slices. All scale bars, 1 mm. Earlier time points and data from additional mice can be found in fig. S7.

off-the-shelf equipment and our ML-based open-access image processing code to detect populations of fewer than 500 cells in vivo. The approach relies entirely on a time series of images, thus making the concept translatable between different OA imaging devices. These tools will facilitate the wider use of OA imaging in life sciences, particularly for the study of cellular dynamics and interactions on the level of whole organisms.

MATERIALS AND METHODS

Cloning

*Rp*BphP1 (*16*) was obtained from Addgene (V. Verkhusha, plasmid no. 79845). Mammalian optimized *Re*BphP was synthesized as gene strings (GeneArt, Life Technologies, Regensburg, Germany). All other BphPs used in the study have been a gift from A. Möglich (University of Bayreuth, Germany).

For bacterial protein expression, the coding sequences of all BphPs used in the study except *Rp*BphP1 were polymerase chain reaction (PCR)–amplified as a Nde I/Xho I fragment and cloned into the second multiple cloning site of the pET-Duet1 vector (Novagen, Merck Millipore). *Rp*BphP1 was PCR-amplified as a Nde I/Pac I fragment and cloned into the second multiple cloning site of the pET-Duet1 vector. In addition, for biliverdin synthesis, the heme oxygenase (HO) of *Nostoc sp.* was cloned using Nco I/Hind III into the first multiple cloning site of pET-Duet1.

For equimolar mammalian expression, first, *Re*BphP_P2A and mCherry were PCR-amplified and then stitched using overlap PCR as an Eco RI/Xba I fragment and cloned in a pcDNA3.0 vector (Thermo Fisher Scientific). Later similar constructs for other BphPs were made by amplifying them as Eco RI/Not I fragment and inserted in place of *Re*BphP1-PCM in the above construct. The resulting plasmids allowed the equimolar coexpression of *Rp*BphP1, *Rp*BphP1-PCM, *Re*BphP-PCM, *Re*BphP-PCM, or *Dr*BphP-PCM and mCherry proteins.

Protein expression and purification

Proteins have been expressed in *E. coli* strain BL21 (DE3) (New England Biolabs, #C2527). In brief, plasmids expressing BphPs and HO were transformed into the BL21 host cells. Bacterial cells were grown in LB media supplemented with ampicillin at 37°C until the culture reached OD (optical density) 0.6, followed by induction of protein expression by addition of IPTG (isopropyl-β-D-thiogalactopyranoside) and further incubation for 16 to 18 hours at 22°C. The next day, the bacterial pellet was collected by centrifugation and pellet was resuspended in phosphate-buffered saline (PBS). After cell lysis, proteins were purified by immobilized metal affinity chromatography in PBS,

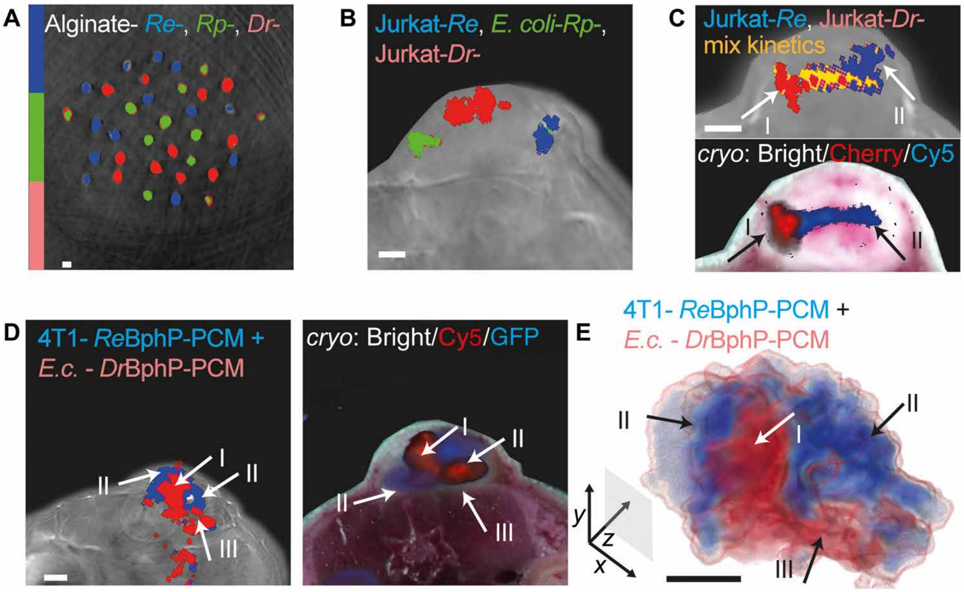

Fig. 5. Parallel visualization of multiple rsOAPs in MSOT. (**A**) Imaging of an alginate bead phantom containing *E. coli* expressing rsOAPs *Re*BphP-PCM, *Rp*BphP1-PCM, and *Dr*BphP-PCM. (**B**) Imaging of Jurkat T cells and *E. coli* (1.4×10^6) expressing each of the three rsOAPs imaged immediately after implantation into a 4T1 tumor. (**C**) Imaging of a 4T1 tumor with implants of two Jurkat T cells expressing rsOAPs. Zones of mixture of the two populations with distinct kinetics are colored yellow. In (A) to (E), color maps indicate clusters showing distinguishable kinetics. (**D**) Imaging of a 4T1 tumor stably expressing *Re*BphP-PCM at day 9 (arrows II and III) imaged immediately after *E. coli* (10^8 cells) expressing *Dr*BphP-PCM have been injected into the tumor (arrow I). Histology confirmation is inferred from fluorescence in *Dr*BphP-PCM (Cy5 only) and *Re*BphP-PCM (GFP primarily). (**E**) Volume representation of *k*. All slices are single representative slices. All scale bars, 1 mm.

followed by gel filtration on a HiLoad 26/600 Superdex 75 pg (GE Healthcare Life Sciences, Freiburg, Germany).

Absorption and fluorescence spectroscopy

For absorption spectra, the purification buffer was exchanged against PBS and the proteins were measured with a Shimadzu UV-1800 spectrophotometer (Shimadzu Inc., Kyoto, Japan) using a 100-μl quartz cuvette. To measure the ON (P_{fr}) and OFF (P_r) spectra of respective proteins, photoswitching was carried out using 650/20-nm or 780/20-nm light-emitting diodes (Thorlabs) placed above the quartz cuvette in the spectrophotometer.

Fluorescence measurements for all BphPs were performed with a Cary Eclipse Fluorescence spectrophotometer (Varian Inc., Australia). Photoswitching was carried out as above. Fluorescence measurement was done by fixing excitation wavelength at 700 nm and emission wavelength at 720 nm. Excitation wavelength and emission slit were set to 5 nm, and the absorbance at the excitation wavelength was always equal to 0.1 to avoid inner filter effects.

Mammalian cell culture

4T1 and Jurkat cells were maintained in RPMI 1640. HeLa and HCT116 cells were maintained in Dulbecco's modified Eagle's medium (DMEM) and McCoy 5A medium, respectively. All media were supplemented with 10% fetal bovine serum (Invitrogen) and antibiotics [penicillin (100 U/ml) and streptomycin (100 mg/ml)]. Cells were cultivated at 37°C and 5% CO_2.

Stable cell lines

Tissue culture

The Platinum-E and RD114 packaging cell lines were cultivated in cDMEM (Complete Dulbecco's modified Eagle medium), HCT116 cell line was grown in McCoy 5A medium (Life Technologies), and 4T1 and Jurkat cells were cultured in cRPMI (Complete Roswell Park Memorial Institute)–1640 Medium. All media were supplemented with 10% fetal calf serum, 0.025% L-glutamine, 0.1% Hepes, 0.001% gentamicin, and 0.002% streptomycin.

Generation of constructs

*Re*BphP-PCM-IRES-GFP was amplified using specific primers (5′-ATTAGCGGCCGCGCCACCATGAGCGGCACCAGAG-3′ and 5′-ATTAGAATTCTCACTTGTACAGCTCGTCCATGCCGTGAGTG-3′) and cloned into the mP71 using Not I and Eco RI restriction sites. The mP71 vector was a gift from W. Uckert.

Generation of cell lines

For retrovirus production, Platinum-E or RD114 packaging cells were transfected with the retroviral vector mP71-*Re*BphP-PCM-IRES-GFP using calcium phosphate precipitation. The supernatant of the packing cells was collected at 48 and 72 hours after transfection and purified from the remaining cells by centrifugation at 1500 rpm at 4°C for 7 min. One day before transduction, non–tissue culture–treated 48-well plates were coated with RetroNectin (Clontech) according to the manufacturer's recommendations overnight at 4°C. After washing once with PBS, virus supernatant was added and centrifuged at 3000*g* and 32°C for 2 hours. Virus supernatant was removed, and cell lines (4T1, HCT116, and Jurkat) were added in 400 μl of the respective medium supplemented with 1:100 LentiBOOST Solution A and 1:100 LentiBOOST Solution B (Sirion Biotech). Cells were then spinoculated at 800*g* at 32°C for 1.5 hours. After 5 days of culture, cells were sorted for high expression of GFP using flow cytometry.

Mouse work

All animal experiments were approved by the government of Upper Bavaria and were carried out in accordance with the approved guidelines. For 4T1 xenografts of stably expressing *Re*Bphp-PCM and GFP, 0.8 × 10^6 cells in PBS have been implanted in the back of FoxN1 nude mice (Charles River Laboratories, Boston, USA) and maintained for 9 days. For HCT116 cells expressing *Re*BphP-PCM and GFP, 1.5 × 10^6 cells in 200 μl PBS have been injected intraperitoneally in FoxN1 nude mice and were maintained for 14 days. For intracranial injections of stably expressing *Re*BphP-PCM and GFP 4T1 cells, mice were first anesthetized according to the animal protocol. The head of the mouse was fixed in a Stereotaxic frame (David Kopf Instruments, model 940), an incision in the skin was made using a scalpel, and a small hole was drilled into the skull. Later, 5-μl cells (0.14 × 10^6 cells/μl) were injected slowly with a 10-μl Hamilton syringe (26Gs). The incision in the skin was closed using Histoacryl (B. Braun Melsungen AG). The mice were scanned in MSOT and sacrificed immediately after scanning. For Matrigel implants of Jurkat cells expressing *Re*BphP-PCM, different concentrations of cells ranging from 6400 to 500 cells/μl were implanted subcutaneously in the back of the mice. Similarly, bacterial cells expressing *Re*BphP-PCM in different concentrations (1.4 × 10^5 to 1.4 × 10^4 cells/μl) were also implanted in the back of the mice. For multiplexing experiment, bacterial cells expressing rsOAPs individually with the concentration of 1.4 × 10^6 cells/μl were implanted on the back of the mice in the same plane. For multiplexing experiment in vivo, intratumoral injections, bacterial cells expressing *Dr*BphP-PCM resuspended in PBS have been injected into the 4T1 tumor expressing *Re*BphP-PCM and GFP using an insulin syringe with a 30-gauge needle.

For all MSOT imaging, mice have been anesthetized using 2% isoflurane in O_2. Anesthetized mice were placed in the MSOT holder using ultrasound gel and water as coupling media. After termination of the experiments, all mice have been sacrificed and stored at −80°C for cryosectioning.

MSOT setup and data acquisition

Phantom and mice data were acquired using a commercially available MSOT scanner (MSOT In Vision 256-TF, iThera Medical GmbH, Munich, Germany). In brief, nanosecond pulsed light was generated from a tunable optical parametric oscillator (OPO) laser and delivered to the sample through a ring-type fiber bundle. The wavelengths, 680 and 770 nm, were used for photoswitching and imaging in phantoms and in mice. Light absorbed by the sample generates an acoustic signal that propagates through the sample and is detected outside the sample by a cylindrically focused 256-element transducer. The transducer array had a central frequency of 5 MHz (−6 dB was approximately 90%) with a radius of curvature of 40 mm and an angular coverage of 270°. Acoustic signals were detected as time series pressure readouts at 2030 discrete time points at 40 MS/s (Mega-samples per second). The acquired acoustic data were reconstructed using the ViewMSOT version 3.8.1.04 (iThera Medical GmbH, Munich, Germany) software with the following settings: 50 kHz to 6.5 MHz; trim speed of 7.

OA data analysis

All data analysis was conducted using MATLAB2018b. The data reconstructed with ViewMSOT were loaded into MATLAB by iThera MATLAB code (iThera MATLAB, version: msotlib_beta_rev75). All analyses were carried out with the code provided along with this manuscript (note S3). In brief, movement correction was done by phase correlation preliminary to optimization-based image co-registration with the intensity and nonrigid co-registration of frames of the first cycle being used as reference. For further processing, different features of the time series have been computed and are used for classification/switching label detection using an ML model. For fast Fourier transform, repetitive frequency of the whole concatenated signal for each image point is computed to identify signals corresponding to the illumination schedule. For exponential fitting, the normalized mean kinetic of all cycles is used. Then, the coefficients compared to an expected exponential kinetic are calculated and used as a quality measure. Here, positive and negative exponential are considered. Using fit coefficients and quality of fit (R^2) as measures, only 77% accuracy compared to a ground truth is achieved. Thus, additional features are invoked. Overall, all analyzed features are (i and ii) the coefficient for the exponential fit ($\exp(b(x+1))$ and $\exp(b(x-1)+1)$ of the mean kinetic (mean of all cycles); (iii) R^2 of the fit; (iv) the mean intensity over the concatenated signal; (v) max-min of all the data at the pixel; (vi to ix) median maximums and minimums of cycles along with SD; (x) number of cycles with positive or negative trend; (xi) the length of the part of the cycle that shows a trend, i.e., at what point the signal vanishes in the noise; and (xii) Fourier coefficient for the expected frequency defined by the photocontrol schedule. All those are used as predictor values for an unmixing model based on random forest approaches (*23*, *25*)—for overall model, trained on 4T1 day 9 as well as highest concentration of Jurkat T lymphocytes. We used 50 trees in the ensemble, as further increase of number did not lead to out-of-bag error decrease. This approach resulted in model performance increase up to 96% of positive predictive value for ground truth (see note S4 for more details on the use of ML in this work).

For visualization, data were not further processed and are shown against the respective slice at 680 nm as anatomy information, except in the case of 4T1 injected in brain where the anatomy is shown at 900 nm. Representative slices are shown. For clustering, appropriate ranges of the kinetic parameter were chosen on the unmixed data to distinguish different labels.

Cryosectioning

After sacrificing, the mice were cryopreserved at −80°C. To detect the fluorescence in tumors, the respective part of the mouse was embedded in Tissue-Tek O.C.T. (Sakura Finetek Europe B.V., Zoeterwonde, The Netherlands). Sections (10 μm) were cut (Leica CM1950, Leica Microsystems, Wetzlar, Germany) for brain, 4T1, and HCT116 mice at the interval of 150, 250, and 500 μm, respectively, and imaged using a 482/35-nm bandpass for excitation and 535/38-nm bandpass filter for detection of GFP fluorescence. Images were taken using an Andor LucaR charge-coupled device camera (DL-604M, Andor Technology, Belfast, UK) with 10-s exposure and a gain of 10. On the basis of the histology, ground truth on co-registered images was created using a semiautomatic procedure based on anatomical markers and intensity-based multimodal co-registration together with a nonrigid spline-based method and human (two independent)–based selection of signals in the fluorescence images.

Bacterial cell immobilization by entrapment and MSOT imaging

A 2 to 4% (w/v) aqueous solution of sodium alginate was prepared in PBS. *E. coli* strain BL21 cells expressing rsOAPs were harvested by centrifugation (4000 rpm, 20 min) and resuspended in PBS. The cell suspensions were then mixed with sterile alginate. Beads were formed by filling the alginate cell mixtures in the syringe with 30-gauge needle, followed by centrifugation at 300 rpm, which allowed the addition of the mixtures into sterile $CaCl_2$ (200 mM). The cell-containing beads, 1 mm in diameter, were allowed to solidify for 10 min before $CaCl_2$ was replaced by fresh distilled water. The cell beads were then randomly distributed in the agar phantom with 1.5% (w/w) agar and 3.5% (v/v) intralipid emulsion and imaged in MSOT as described elsewhere.

OA characterization of proteins

For OA characterization of rsOAPs, custom-made experimental setup was used as described earlier (*22*). Briefly, nanosecond excitation pulses were generated by an OPO laser (SpitLight DPSS 250 ZHGOPO, InnoLas) running at a repetition rate of 50 Hz. Constant pulse energy was ensured using a half-wave plate in a motorized rotation stage (PRM1Z8, Thorlabs) and a polarizing beam splitter; using a lookup table and adapting the polarization with the half-wave plate, we kept the power constant at ~1.3 mJ (otherwise mentioned) over the whole illumination schedule. Samples were injected into an acoustically coupled flow chip (μ-Slide I 0.2 Luer, hydrophobic, uncoated, ibidi) and illuminated from one side using a fiber bundle (CeramOptec) at a constant pulse energy of ~1.3 mJ at the fiber output. Photoswitching was carried out by illuminating the sample alternatively with 650- and 780-nm light. OA signals were detected with a cylindrically focused single-element transducer (V382-SU, 3.5 MHz, Olympus) followed by signal amplification by 60 dB with a wide-band voltage amplifier (DHPVA-100, Femto) and digitized at 100 MS/s with a data acquisition card (RZE-002 400, GaGe). Dependency of $P_{fr} \rightarrow P_r$ conversion on 770-nm pulse energy was measured with different pulse energies (0.4, 0.7, 1.0, and 1.3 mJ). Dependency of $P_{fr} \rightarrow P_r$ conversion on repetition rate of laser was measured with three different laser repetition rates (10, 25, and 50 Hz). Effect of different switching ON wavelength and resulting dynamic range at 770 nm was measured using different switching ON wavelength ranging from 630 to 680 nm.

SUPPLEMENTARY MATERIALS

Supplementary material for this article is available at http://advances.sciencemag.org/cgi/content/full/6/24/eaaz6293/DC1

View/request a protocol for this paper from *Bio-protocol*.

REFERENCES AND NOTES

1. V. Ntziachristos, D. Razansky, Molecular imaging by means of multispectral optoacoustic tomography (MSOT). *Chem. Rev.* **110**, 2783–2794 (2010).
2. L. V. Wang, S. Hu, Photoacoustic tomography: In vivo imaging from organelles to organs. *Science* **335**, 1458–1462 (2012).
3. P. Hai, T. Imai, S. Xu, R. Zhang, R. L. Aft, J. Zou, L. V. Wang, High-throughput, label-free, single-cell photoacoustic microscopy of intratumoral metabolic heterogeneity. *Nat. Biomed. Eng.* **3**, 381–391 (2019).
4. J. Yao, L. Wang, J.-M. Yang, K. I. Maslov, T. T. W. Wong, L. Li, C.-H. Huang, J. Zou, L. V. Wang, High-speed label-free functional photoacoustic microscopy of mouse brain in action. *Nat. Methods* **12**, 407–410 (2015).
5. J. Aguirre, M. Schwarz, N. Garzorz, M. Omar, A. Buehler, K. Eyerich, V. Ntziachristos, Precision assessment of label-free psoriasis biomarkers with ultra-broadband optoacoustic mesoscopy. *Nat. Biomed. Eng.* **1**, 68 (2017).
6. J. Reber, M. Willershäuser, A. Karlas, K. Paul-Yuan, G. Diot, D. Franz, T. Fromme, S. V. Ovsepian, N. Bézière, E. Dubikovskaya, D. C. Karampinos, C. Holzapfel, H. Hauner, M. Klingenspor, V. Ntziachristos, Non-invasive measurement of brown fat metabolism based on optoacoustic imaging of hemoglobin gradients. *Cell Metab.* **27**, 689–701.e4 (2018).
7. V. Gujrati, A. Mishra, V. Ntziachristos, Molecular imaging probes for multi-spectral optoacoustic tomography. *Chem. Commun.* **53**, 4653–4672 (2017).
8. J. Brunker, J. Yao, J. Laufer, S. E. Bohndiek, Photoacoustic imaging using genetically encoded reporters: A review. *J. Biomed. Opt.* **22**, 70901 (2017).
9. Y. Liu, P. Bhattarai, Z. Dai, X. Chen, Photothermal therapy and photoacoustic imaging: Via nanotheranostics in fighting cancer. *Chem. Soc. Rev.* **48**, 4950–4965 (2019).
10. C. Moore, J. V. Jokerst, Strategies for image-guided therapy, surgery, and drug delivery using photoacoustic imaging. *Theranostics* **9**, 1550–1571 (2019).
11. I. Steinberg, D. M. Huland, O. Vermesh, H. E. Frostig, W. S. Tummers, S. S. Gambhir, Photoacoustic clinical imaging. *Photoacoustics* **14**, 77–98 (2019).
12. F. Knieling, C. Neufert, A. Hartmann, J. Claussen, A. Urich, C. Egger, M. Vetter, S. Fischer, L. Pfeifer, A. Hagel, C. Kielisch, R. S. Görtz, D. Wildner, M. Engel, J. Röther, W. Uter, J. Siebler, R. Atreya, W. Rascher, D. Strobel, M. F. Neurath, M. J. Waldner, Multispectral optoacoustic tomography for assessment of crohn's disease activity. *N. Engl. J. Med.* **376**, 1292–1294 (2017).
13. L. V. Wang, J. Yao, A practical guide to photoacoustic tomography in the life sciences. *Nat. Methods* **13**, 627–638 (2016).
14. K. Mishra, J. P. Fuenzalida-Werner, V. Ntziachristos, A. C. Stiel, Photocontrollable proteins for optoacoustic imaging. *Anal. Chem.* **91**, 5470–5477 (2019).
15. A. C. Stiel, X. L. Deán-Ben, Y. Jiang, V. Ntziachristos, D. Razansky, G. G. Westmeyer, High-contrast imaging of reversibly switchable fluorescent proteins via temporally unmixed multispectral optoacoustic tomography. *Opt. Lett.* **40**, 367–370 (2015).
16. J. Yao, A. A. Kaberniuk, L. Li, D. M. Shcherbakova, R. Zhang, L. Wang, G. Li, V. V. Verkhusha, L. V. Wang, Multiscale photoacoustic tomography using reversibly switchable bacterial phytochrome as a near-infrared photochromic probe. *Nat. Methods* **13**, 67–73 (2016).
17. H. Dortay, J. Märk, A. Wagener, E. Zhang, C. Grötzinger, P. Hildebrandt, T. Friedrich, J. Laufer, Dual-wavelength photoacoustic imaging of a photoswitchable reporter protein, in *Photons Plus Ultrasound: Imaging and Sensing*, A. A. Oraevsky, L. V Wang, Eds. (International Society for Optics and Photonics, 2016), vol. 9708.
18. J. Märk, H. Dortay, A. Wagener, E. Zhang, J. Buchmann, C. Grötzinger, T. Friedrich, J. Laufer, Dual-wavelength 3D photoacoustic imaging of mammalian cells using a photoswitchable phytochrome reporter protein. *Commun. Phys.* **1**, 3 (2018).
19. L. Li, A. A. Shemetov, M. Baloban, P. Hu, L. Zhu, D. M. Shcherbakova, R. Zhang, J. Shi, J. Yao, L. V. Wang, V. V. Verkhusha, Small near-infrared photochromic protein for photoacoustic multi-contrast imaging and detection of protein interactions in vivo. *Nat. Commun.* **9**, 2734 (2018).
20. R. K. W. Chee, Y. Li, W. Zhang, R. E. Campbell, R. J. Zemp, In vivo photoacoustic difference-spectra imaging of bacteria using photoswitchable chromoproteins. *J. Biomed. Opt.* **23**, 106006 (2018).
21. D. M. Shcherbakova, M. Baloban, S. Pletnev, V. N. Malashkevich, H. Xiao, Z. Dauter, V. V. Verkhusha, Molecular basis of spectral diversity in near-infrared phytochrome-based fluorescent proteins. *Chem. Biol.* **22**, 1540–1551 (2015).
22. P. Vetschera, K. Mishra, J. P. Fuenzalida-Werner, A. Chmyrov, V. Ntziachristos, A. C. Stiel, Characterization of reversibly switchable fluorescent proteins in optoacoustic imaging. *Anal. Chem.* **90**, 10527–10535 (2018).
23. T. G. Dietterich, An experimental comparison of three methods for constructing ensembles of decision trees: Bagging, boosting, and randomization. *Mach. Learn.* **40**, 139–157 (2000).
24. S. Zhou, C. Gravekamp, D. Bermudes, K. Liu, Tumour-targeting bacteria engineered to fight cancer. *Nat. Rev. Cancer* **18**, 727–743 (2018).
25. L. Breiman, Random forests. *Mach. Learn.* **45**, 5–32 (2001).
26. J. E. Brown, L. Diaz, T. Christoff-Tempesta, K. M. Nesbitt, J. Reed-Betts, J. Sanchez, K. W. Davies, Characterization of nitrazine yellow as a photoacoustically active pH reporter molecule. *Anal. Chem.* **87**, 3623–3630 (2015).
27. D. Bellini, M. Z. Papiz, Structure of a bacteriophytochrome and light-stimulated protomer swapping with a gene repressor. *Structure* **20**, 1436–1446 (2012).
28. X. Yang, J. Kuk, K. Moffat, Crystal structure of *Pseudomonas aeruginosa* bacteriophytochrome: Photoconversion and signal transduction. *Proc. Natl. Acad. Sci. U.S.A.* **105**, 14715–14720 (2008).
29. J. R. Wagner, J. Zhang, D. von Stetten, M. Günther, D. H. Murgida, M. A. Mroginski, J. M. Walker, K. T. Forest, P. Hildebrandt, R. D. Vierstra, Mutational analysis *Deinococcus radiodurans* bacteriophytochrome reveals key amino acids necessary for the photochromicity and proton exchange cycle of phytochromes. *J. Biol. Chem.* **283**, 12212–12226 (2008).
30. C. J. C. Burges, A tutorial on support vector machines for pattern recognition. *Data Min. Knowl. Discov.* **2**, 121–167 (1998).
31. A. Liaw, M. Wiener, Classification and regression by randomForest. *R News* **2**, 18–22 (2002).
32. E. Osuna, R. Freund, F. Girosi, *Support Vector Machines: Training and Applications* (Massachusetts Institute of Technology, 1997).
33. X. Deán-Ben, A. Stiel, Y. Jiang, V. Ntziachristos, G. G. Westmeyer, D. Razansky, Light fluence estimation by imaging photoswitchable probes with temporally unmixed multispectral optoacoustic tomography, in *Optics InfoBase Conference Papers 3* (Optical Society of America, 2016).
34. L. V. Wang, H, Wu, *Biomedical Optics: Principles and Imaging* (Wiley-Interscience, 2007).

Acknowledgments: We thank A. Möglich for providing the wild-type BphPs, R. Hillermann for technical assistance, and A. C. Rodríguez for discussions on the manuscript. We further thank P. Vetschera for his initial contributions to the OA spectrometer device. **Funding:** K.M. and

A.C.S. received funding from DFG (STI656/1-1). V.R.B. received funding from DFG SFB 1054 (TP B09). Y.H. received funding from the China Scholarship Council via fellowship (CSC 201306960006). **Author contributions:** K.M. performed all measurements (for in vitro data with help from J.P.F.-W. and Y.H.; for in vivo measurements with assistance from U.K. and occasional help from V.G.). K.M. analyzed all in vitro data. All in vivo data were analyzed by M.S. along with K.M. M.S. wrote analysis code and GUI. S.G. established stable cell lines. A.C.S. wrote the manuscript and conceived the project together with K.M. and M.S. V.R.B. and V.N. contributed to the manuscript. **Competing interests:** V.N. is a shareholder of iThera Medical GmbH. All other authors declare no competing interests. **Data and materials availability:** Data availability: A reduced source data contents file is available online. Due to size limitations of depositing raw imaging data, the data that support the findings of this study are available from the corresponding author upon request. *Rp*BphP1-PCM, a derivative of the original *Rp*BphP1 from the laboratory of V. V. Verkhusha (Kaberniuk, Nat. Meth. 2016), can be provided by the authors' pending scientific review and a completed material transfer agreement to nonprofit organizations solely. Code availability: Detailed code is available from the corresponding author upon request. A version of the code meant for public use together with a GUI can be found at https://gitlab.lrz.de/ga45huk/rsoap_analysis/.

Submitted 26 September 2019
Accepted 1 May 2020
Published 12 June 2020
10.1126/sciadv.aaz6293

Citation: K. Mishra, M. Stankevych, J. P. Fuenzalida-Werner, S. Grassmann, V. Gujrati, Y. Huang, U. Klemm, V. R. Buchholz, V. Ntziachristos, A. C. Stiel, Multiplexed whole-animal imaging with reversibly switchable optoacoustic proteins. *Sci. Adv.* **6**, eaaz6293 (2020).